SLAC-449
SLAC/SSRL-0088
UC-408
(SSRL-M)

LIGAND K-EDGE X-RAY ABSORPTION SPECTROSCOPIC STUDIES OF THE ELECTRONIC STRUCTURE OF INORGANIC MODEL COMPLEXES AND METALLOPROTEIN ACTIVE SITES

Susan E. Shadle

Stanford Linear Accelerator Center
Stanford Synchrotron Radiation Laboratory
Stanford University, Stanford, California 94309

August 1994

Prepared for the Department of Energy under contract number DE-AC03-76SF00515 and the NIH, Biomedical Resource Technology Program, Division of Research Resources

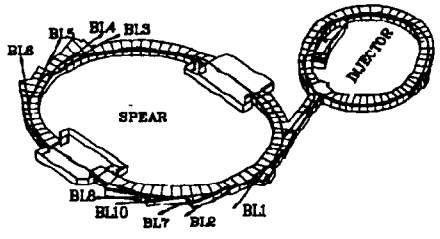

Printed in the United States of America. Available from the National Technical Information Service, U.S. Department of Commerce, 5285 Port Royal Road, Springfield, Virginia 22161

* Ph.D. thesis

LIGAND K-EDGE X-RAY ABSORPTION SPECTROSCOPIC STUDIES OF THE ELECTRONIC STRUCTURE OF INORGANIC MODEL COMPLEXES AND METALLOPROTEIN ACTIVE SITES

A DISSERTATION
SUBMITTED TO THE DEPARTMENT OF CHEMISTRY
AND THE COMMITTEE ON GRADUATE STUDIES
OF STANFORD UNIVERSITY
IN PARTIAL FULFILLMENT OF THE REQUIREMENTS
FOR THE DEGREE OF
DOCTOR OF PHILOSOPHY

By
Susan E. Shadle
August 1994

Abstract

Ligand K-edge X-ray absorption spectroscopy (XAS) has been developed as a technique for the investigation of ligand-metal bonding and has been applied to the study of electronic structure in inorganic model complexes and metalloprotein active sites.

Bonding in Cl-Cu(II) Complexes. Ligand K-edge XAS has been measured at the chloride K-edge for a series of complexes containing chloride ligands bound to open shell d^9 copper ions. The intensity of the pre-edge feature in these spectra reflects the covalency in the half-occupied $d_{x^2-y^2}$-derived molecular orbital (HOMO) of the complex. The energy of the pre-edge feature is related to both the charge on the ligand and the HOMO energy. An analysis of the intensity and energy of the pre-edge feature as well as the energy of the rising edge absorption provides quantitative information about the covalency of the ligand-metal interaction, the charge donated by the chloride, and the energy of the copper d-manifold. The results demonstrate that ligand K-edge XAS features can be used to obtain quantitative information about ligand-metal bonding. The results also identify the chemical basis for trends in the XAS data for the complexes: D_{4h} $CuCl_4^{2-}$, D_{2d} $CuCl_4^{2-}$, planar, trans-$CuCl_2(pdmp)_2$ (pdmp=N-phenyl-3,5-dimethyl-pyrazole), square pyramidal $CuCl_5^{3-}$, the planar dimer $KCuCl_3$, the distorted tetrahedral dimer $(Ph_4P)CuCl_3$, and two dimers with mixed ligation, one containing a bridging chloride, and the other, terminally bound chloride. A geometric distortion from square planar to distorted tetrahedral results in a decrease in the chloride-copper HOMO covalency but an increase in the total charge donation by the chlorides. Thus, while the geometry can maximize the overlap for a highly covalent HOMO, this does not necessarily reflect the overall charge donation. The Cl-Cu(II) bonding interactions are dependent on the nature of the other coordinating ligands. Replacement of chlorides by less strongly donating ligands causes an increase in charge donation by the remaining chloride ligands. An increase in the coordination number of the copper or in the charge donation by the ligands (resulting in a lower effective nuclear charge on the copper) causes an increase in the copper d-manifold energy. Finally, the bonding of a terminal *vs.* bridging chloride is very different, in that for the latter there is more total charge donation and a higher ligand covalent contribution to the HOMO orbital of the two coppers.

Investigation of the Source of the Small EPR $A_{\parallel}$ Splitting in Blue Copper. XAS for the oxidized blue copper protein plastocyanin and several Cu(II) model complexes have been measured at both the Cu K-edge and the ligand (Cl and S) K-edges in order to elucidate the source of the small parallel hyperfine splitting in the EPR spectra of blue copper centers. A feature in the Cu K-edge X-ray absorption

spectrum at ~8987 eV has been assigned as the Cu 1s —> 4p + ligand-to-metal charge transfer shakedown transition. This has allowed quantitation of 4p mixing into the ground state wavefunction, which is reflected in the 1s —> 3d (+4p) intensity at ~8979 eV. The results show that distorted tetrahedral (D_{2d}) $CuCl_4^{2-}$ is characterized by < 4% Cu $4p_z$ mixing while plastocyanin has only Cu $4p_{x,y}$ mixing. Thus, the small parallel hyperfine splitting in the EPR spectra of D_{2d} $CuCl_4^{2-}$ and of oxidized plastocyanin can not be explained by 12% $4p_z$ mixing into the $3d_{x^2-y^2}$ orbital as had been previously postulated. Data collected at the Cl K-edge for $CuCl_4^{2-}$ of various geometries show that the intensity of the ligand pre-edge feature at ~2820 eV reflects the degree of covalency between the metal half-occupied orbital and the ligands. The data show that D_{2d} $CuCl_4^{2-}$ is not unusually covalent. The source of the small parallel splitting in the EPR of D_{2d} $CuCl_4^{2-}$ is discussed. Experiments at the S K-edge (~2470 eV) show that plastocyanin is characterized by a highly covalent Cu-S(cysteine) bond relative to the cupric-thiolate model complex, [Cu(tet *b*)(*o*-$SC_6H_4CO_2$)]·H_2O. Self-consistent-field-Xα-scattered-wave calculations have been used to understand copper-thiolate bonding in this model complex and to quantify the covalency reflected in the S K-edge pre-edge intensity. The XAS results demonstrate that the small parallel hyperfine splitting in the EPR spectra of blue copper sites reflects the high degree of covalency of the copper-thiolate bond.

S(Cys)-Cu(II) Covalency in Blue Copper Sites. S K-edge X-ray absorption spectra have been measured for a series of Cu-thiolate model complexes, blue copper sites and sites designed by site-directed mutagenesis. The latter are specifically designed to (i) examine various aspects of the native protein active sites and/or (ii) act as active site models for native proteins which have proved difficult to study by X-ray crystallography. These studies provide quantitative information about the S(Cys) covalency in the redox-active HOMO of the site. Classic blue copper sites such as plastocyanin and azurin are characterized by a conserved, highly covalent S(Cys)-Cu bonding interaction. This property dominates many of the spectral features and much of the electronic structure of these sites. Model complexes which contrast blue and normal copper further support that a highly covalent S(thiolate) interaction is necessary for the properties of a blue site. For centers in which the C_{3v} symmetry of the blue copper active site is destroyed, such as H117G(Cu) or H117G(Hista) azurin mutants, the spectral properties indicate a normal copper site and significantly decreased S(Cys)-Cu covalency. The addition of imidazole to H117G azurin reconstitutes the blue copper geometry and restores the high S(Cys)-Cu covalency as well. Thus, the strong equatorial ligands in the blue copper site are necessary for the highly covalent S(Cys)-Cu bond and the resulting electronic structure of

the blue copper site. Decreased HOMO covalency, relative to plastocyanin and azurin, is observed in the perturbed blue copper protein stellacyanin. This is consistent with the suggestion that stellacyanin has a stronger axial ligand (O(Glutamine)) than the classic blue sites, which may result in a rotation of the HOMO and less S(Cys)-Cu overlap. A further decrease in covalency is observed in the high pH form of the protein. The decrease in covalency in stellacyanin relative to the classic blue copper sites may reflect either a moderate decrease only in Sp_π interactions with the Cu(II) or a large decrease in Sp_π accompanied by an increase in Sp_σ interactions. Nitrite Reductase (NiR) exhibits a total HOMO covalency which is similar to that observed in the classic blue copper centers. Variations observed in the optical spectrum, however, suggest that the covalency in NiR may be distributed differently. Specifically, a decrease in S(Cys)-Cu π-bonding is likely to be accompanied by an increase in S(Cys)-Cu σ-bonding. The total covalency, as reflected in the S K-edge pre-edge intensity, would remain approximately equal to that in the classic blue copper sites. The combination of the S K-edge results with other analyses on these sites will provide insight into the source of the changes in optical absorption intensity at ~450 nm in perturbed blue copper centers. Finally, the S K-edge of H35Q provides evidence that a mutation away from the active site can effect the S(Cys)-Cu covalency at the active site in a blue copper protein.

Ligand-Metal Bonding in a Series of T_d MCl_4^{n-}. Chloride K-edge XAS have been measured for a series of T_d MCl_4^{n-} complexes (M = Cu(II), Ni(II), Co(II), Fe(II), and Fe(III)) to investigate ligand-metal bonding. The intensity of the pre-edge feature in these spectra reflects excited state multiplet effects, intermediate ligand field excited-state mixing, and ligand-metal covalency in the partially-occupied d-orbital derived molecular orbitals of each complex. A methodology which relates covalency to pre-edge intensity for d^{10-n} hole systems ($n \geq 1$) is developed. Application of this methodology to the experimental data provides quantitative information about the covalency of the ligand-metal bond. The energy of the pre-edge feature is related to both the charge on the ligand and the metal d-derived orbital energy. An analysis of the pre-edge and edge energies allows the relative energy of the metal d-manifold as well as the charge on each chloride ligand to be quantitated. An analysis of the pre-edge and edge energies allows the relative energy of the metal d-manifold as well as the charge on each chloride ligand to be quantitated. Results show the metal d-derived orbital covalency decreases across the series from $Cu(II)Cl_4^{2-}$ to $Fe(II)Cl_4^{2-}$, while that of $Fe(III)Cl_4^{-}$ is larger than $Fe(II)Cl_4^{2-}$. This is related to the experimentally determined relative d-manifold energies which vary in the order Fe(III) < Cu(II) < Ni(II) < Co(II) < Fe(II). The metal centers with the deepest d-manifold energies (closest to the ligand 3p orbital energy) are involved in the

strongest ligand-metal bonding interactions and exhibit the largest covalency. The total charge donated by the chloride ligands to the metal is greatest in $Fe(III)Cl_4^-$ and the variation observed is similar to that seen in the HOMO covalency: Fe(III) > Cu(II) > Fe(II) ~ Co(II) ~ Ni(II). The results demonstrate the extension of ligand K-edge XAS to the investigation of ligand-metal bonding in d^{10-n} hole systems ($n \geq 1$) and form the foundation for ligand K-edge XAS studies of electronic structure in transition metal centers.

Ligand-Metal Bonding in Model Systems for Fe-S Proteins. The Cl and S K-edge XAS have been measured for a series of iron-sulfur model complexes which serve as analogs for Fe-S protein active sites. Features in the spectra are qualitatively assigned. Spectra of complexes containing terminal thiolate ligands display an intense thiolate-based feature at the onset of the edge jump. The energy of this feature varies significantly with the type of thiolate ligand. In both dimeric and tetrameric Fe-S sites both sulfide and thiolate pre-edge features are observed. The thiolate transitions occur at higher energy, reflecting the deeper 1s core of the less negative thiolate ligand. The sulfide covalency in the metal d-derived orbitals appears to be greater than the thiolates, reflecting the bridging nature of the sulfide ligands. The bridging sulfide ligands in Fe-S tetramers donate the same total charge as in the dimer. Thus, charge donated per iron by a given sulfide is greater in the dimer than in the tetramer. Further, the sulfide pre-edge intensity is greater in the dimer, suggesting that the sulfide covalency in the HOMOs of the dimer may be greater than in the tetramer. Both terminal thiolates and terminal chlorides donate less charge in the tetramer than in the dimer. This may be related to the difference in oxidation state of the metal in each cluster. Finally, spectra indicate that the d-manifold energy in the tetramers is at less deep binding energy than the dimer, consistent with differences in iron charge.

Spectroelectrochemical Studies of 2Fe Ferredoxin. Studies were undertaken to electrochemically generate the one-electron reduced form of 2Fe ferredoxin (Fd) for investigation with XAS. Tests were performed to characterize the RVC electrode response and to determine the optimal conditions for electrochemical control of Fd. XAS measurements were made of the oxidized and reduced forms of the proteins at both the Fe and S K-edges. Because a number of difficulties were encountered in the attempt to electrochemically stabilize Fd in aqueous solution for XAS measurements, the XAS results are preliminary. Relative to the oxidized spectrum, the reduced Fd Fe K-edge spectrum clearly reflects the contribution of one Fe(II) ion and one Fe(III) ion. The S K-edge of oxidized Fd shows similarity to a diferric Fe-S model complex. Changes observed in the S K-edge of reduced Fd relative to the oxidized spectrum do not directly

reflect changes in covalency in partially occupied molecular orbitals, but are certainly related to changes in the electronic structure of the site. These preliminary results demonstrate that changes in the electronic structure of the reduced 2Fe site relative to the oxidized site can be observed in X-ray absorption spectra and that electrochemical control of proteins in aqueous solution for XAS studies is feasible.

Acknowledgments

I approach research in a very social way (much as I approach other things in my life) and as a result there are a significant number of people who have contributed in a variety of ways, both big and small, to the success of my graduate experience.

I came to Stanford not at all sure what I was interested in and I was lucky to stumble upon a really neat project and into the somewhat unique situation of having two advisers. I have conducted my research under the guidance of Ed Solomon and Keith Hodgson. Being involved in a jointly-advised project has been a very positive experience for me - having two different two scientific perspectives, two advising styles, and two groups full of colleagues to work with has only been an advantage. Ed is expert at distilling a complicated equation down to its physical basis and it is from him that I have learned the importance of understanding the meaning in the symbols and numbers. Keith has demonstrated great confidence in my abilities and I have learned from his careful approach to data measurement and analysis.

As a half-Hodgson student, I have been fortunate to work with Drs. Britt Hedman and Pat Frank. In many ways Britt has acted as a third adviser over the last six years. She taught me everything I know about how to run an X-ray absorption experiment in a careful and organized(!) way. She is the queen of multitasking, and, despite her never-ending lists of things to do (and the overflowing ACTION file), is able to give her undivided attention and to communicate that your question is important. As a woman in science, I feel very fortunate to have had such a positive role model.

I owe much of my self confidence as a scientist to Dr. Pat Frank, who has acted as a true mentor. He has never let me get away with less than complete confidence in myself. He has unending patience for answering questions, no matter how clueless. His competence as a scientist and his willingness to discuss (and help out) with experimental difficulties has been invaluable. I have also enjoyed Pat's friendship. He has always been willing to listen to me bitch about one thing or another, to debate the topic of the day, or to suggest a movie I didn't have time to see.

The success of my experimental work can in part be attributed to the staff at SSRL. Beam time is tiring and stressful and they do everything they can to help experiments run smoothly.

I could fill another page just naming those in both labs who have helped me by getting me lunch on the beamline or answering a question or preparing a sample, because everyone in both labs has contributed to my experience here. Certainly the fact that I

didn't lose my mind over the last few years must be attributed to my colleagues in both labs.

There are a number of people, however, who deserve special mention. Paul Ross happily answered my clueless, first-year questions and as well as offered an oasis in an environment then dominated by sports scores and science that I did not yet understand. Paul now offers promise that there is indeed life after graduate school. Lou LaCroix, without whom I might have graduated about three weeks sooner, has been a great colleague, fellow-TA, and friend. Its nice to know that he still talks to me even though he's seen me at my worst... and that as long as its within his power, he'll keep me well fed. Kendra Williams, the third in a line of bright women students to take on a joint project (!), deserves thanks as well. First, for taking over where I leave off (good luck!) and second, for giving me the opportunity to teach someone else what I've learned, a job I have thoroughly enjoyed. Other people who deserve special mention (in a random order) include Jeff Guckert, with whom I share a healthy cynicism and an historical affinity for vanilla nut coffee; Heather Bufford, who has always been interested and enthusiastic about hearing and discussing vector projections, the electric dipole approximation or whatever topic is perplexing me at the moment; Marty Kirk, for bad boys and bad lingo; Dave Root, who has always been willing to engage (at length!) in scientific discussion (or any other topic for that matter); Cathy Boxwell and Cecilia Campochiaro, for offering perspective and feeding us excellent dinners, Uma Sundarum for delicious Indian food and her infectious sense of humor; Mark Pavlovksy for answering "sure, why not?" to Carl when questioned about whether Carl should ask me out; David Elizier for listening to my bitching and moaning and for sharing late night thesis-writing shifts; and Mark Yeager and Brooke Hemming, for their friendship and for having the courage to do what they really wanted to do and, in so doing, acting as role models for the rest of us. Brooke has also been a feminist compatriot and I've enjoyed our many discussions over the years.

Tami Westre and Jane DeWitt have been great labmates as well as excellent friends. Jane, who began a year before me, acted as a role model for how to be a responsible and successful graduate student. Our friendship grew over many long night shifts, several trips to Brookhaven, and a number of pints of Ben and Jerry's ice cream. Jane has been incredibly supportive and understanding (even long distance) and I have on more than one occasion appreciated her ability to put things into perspective. Fortunately for me, Tami forgave the fact that Jane and I put ourselves together on night-shift during her first run. Had she not done so, I'd have missed out on very productive discussions about data analysis and interpretation as well as the bitch sessions which have been absolutely vital to my survival over the years. I'd also have missed the gossip about

Sjon's latest purchase and Wendy's latest nailcolor. (She'll probably get a lot more done when I'm gone).

My involvement in education at Stanford (besides my own as a graduate student) has made my life here much richer. I credit Dr. Kirk Roberts with identifying my enthusiasm for teaching and connecting me with people at the Center for Teaching and Learning. Michelle Marincovich and others have offered me a forum in which my interpersonal skills and enthusiasm for teaching was appreciated and put to good use. Similarly, my experiences as a undergraduate academic adviser and as a mentor in the Women's Science and Engineering Network have reminded me of the existence of the world beyond the lab and have allowed me to feel I was making a small contribution to others at Stanford. Once I'm gone, maybe someone will get a word in edgewise at a WSEN advisory committee meeting.

People who have influenced my past and my future also deserve mention here. The faculty at Colgate University, particularly those in the Chemistry Department, gently nudged me onto this path. Prof. Mike Shen thankfully allowed me to be "just a happy undergrad" at the time, allowing me to decide for myself if pursuing research was what I wanted to do. When I was thinking about what to do after graduate school, I spoke to a lot of people involved in science education who took the time to encourage my efforts and to offer their perspective. It has bolstered my enthusiasm and motivation to know that there are so many exciting ways I can use my abilities as a scientist and as a communicator.

Friends outside the lab have been invaluable. Beth and David Martin have been wonderful friends over the last several years and I shall miss our dinners and my long (cheap) phone conversations with Beth. Friends from college: Julie & Joe, Amy, and Eileen have thankfully offered their support and have consistently reminded me that it is not normal to be working 80 hours a week.

It is difficult to acknowledge Carl for all the ways he has contributed to this accomplishment: patience for the long hours spent at the beam line, an answer to a question about $X\alpha$ or the irreducible tensor method, a creative meal or delicious dessert, or a listening ear for the latest story. Carl has provided a respite from the lab which always threatened (and largely succeeded) to steal all our time. He has filled my life outside the lab with laughter and support and patience and encouragement. I couldn't have done it without him (so its a good thing Ed didn't move to Cal).

Finally, and most importantly, I would like to thank my family for their support. I have always enjoyed my sister Ellen's long-winded accounts of her life and have marveled at how little planning really needs to be done ahead of time. I respect her

ability to go after what she really wants and hope I can apply her example in my own life. My parents, Bill and Carolyn Shadle, have always given me the freedom to figure out for myself what I wanted to do and have always had confidence that I could succeed at anything. It is on the basis of their love and support that I build my successes and so it is to them I dedicate this thesis.

P.S. I also thank the ninety-five million people who care.

Contents

List of Tables

Chapter 2

Chapter 3

Chapter 4

Chapter 5

List of Figures

Chapter 1

Chapter 2

Chapter 3

Chapter 4

Chapter 5

Chapter 6

Chapter 7

List of Abbreviations

[9]aneN_3	1,4,7-triazacyclononane
*Ad*WT	*Alcaligenes denitrificans* wild type azurin
Cu_2(L-O^-)Cl	[Cu_2(L-O^-)Cl][BPh_4]$_2$·CH_3COCH_3
Cu_2PAP	[Cu_2(PAP6Me)(OH)Cl_3]·H_2O
Cu-tet *b*	[Cu(tet *b*)(*o*-$SC_6H_4CO_2$)]·H_2O
Co9ane	[Co([9]aneN_3)$_2$]Cl_3
CT	charge transfer
EPR	electron paramagnetic resonance
Fd	ferredoxin
FWHM	full-width-at-half-maximum
H117G(Cu)	*P. aeruginosa* His117Gly(Cu) azurin
H117G(Hista)	*P. aeruginosa* His117Gly(Hista) azurin
H117G(Im)	*P. aeruginosa* His117Gly(Im) azurin
H35Q	*Pseudomonas aeruginosa* His35Gln azurin
HOMO	highest occupied molecular orbital
LCAO	linear combination of atomic orbitals
LCu(SCPh$_3$)	Cu(SCPh$_3$)[HB(3,5-*i*-Pr$_2$pz$_3$)]
LF	ligand field
LMCT	ligand-to-metal charge transfer
M121Q	*A. denitrificans* Met121Gln azurin
MCD	magnetic circular dichroism
NiR	*Achromobacter cycloclastes* Nitrite Reductase
PAP6Me	1,4-di(6'-methyl-2'-pyridyl)aminophtalazine
*Pa*WT	*Pseudomonas aeruginosa* wild type azurin
Pc	plastocyanin
pdmp	N-phenyl-3,5-dimethylpyrazole
rR	resonance Raman
SALC	symmetry-adapted linear combination
SCF-Xα-SW (Xα)	self-consistent field-Xα-scattered wave
Stella(HI)	*Rhus vernicifera* Stellacyanin (high pH)
Stella(LO)	*Rhus vernicifera* Stellacyanin (low pH)
Tfa	trifluoroacetate
WT	wild type
XAS	X-ray absorption spectroscopy

Chapter 1

Introduction to X-ray Absorption Edge Spectroscopy

1.1. Scope and Organization of this Dissertation

This dissertation focuses on the development of ligand K-edge X-ray absorption spectroscopy (XAS) and its application to the study of the electronic structure of metalloprotein active sites as well as to inorganic model compounds for these sites. Some transition metal K-edge XAS results are also included. A portion of the XAS data included in this thesis was collected prior to my tenure as a graduate student by Dr. Britt Hedman (a portion of the ligand K-edge data presented) and by Drs. James Penner-Hahn, Teresa Smith, and Robert Scott (the polarized XAS data presented in Chapter 3). I, however, have had primary responsibility for the analysis of these data and have interpreted the data with respect to my own research projects.

The remainder of Chapter 1 provides a brief overview of XAS, including the information content of transition metal K-edges. The methodology for the interpretation of ligand K-edge XAS is also presented. The basic XAS experimental design is discussed with particular attention to the details of the low-energy ligand K-edge experiment. Finally, a brief background is given on SCF-Xα-SW calculations, which are included in the Analysis Sections of Chapters 3 and 5.

Each of the subsequent experimental chapters has a brief introduction focusing specifically on the aspects of the project to be discussed. Chapter 2 presents the analysis of the Cl K-edge spectra of a series of Cu(II)-Cl model complexes and demonstrates how ligand XAS features are used to obtain information about ligand-metal bonding. Polarized Cu K-edges, combined with S K-edge XAS, are analyzed in Chapter 3 to determine the electronic structural basis of the small $A_{||}$ EPR hyperfine splitting in the blue copper protein, plastocyanin. Chapter 4 extends the S K-edge studies to probe the electronic structure of a series of "perturbed" blue copper sites. In Chapter 5, Cl K-edges of a series of first-row transition metal tetrachlorides are analyzed and the methodology is presented for the analysis of K-edges of ligands bound to metal ions other than copper. The S K-edges of model complexes for the 1Fe site in rubredoxin and the 2Fe and 4Fe sites in ferredoxins is presented in Chapter 6. Finally, Chapter 7 describes initial attempts to electrochemically stabilize the 2Fe2S spinach ferredoxin site in a one-electron reduced mixed-valent form. Preliminary Fe K-edge and S K-edge XAS results from these studies are presented.

1.2. X-ray Absorption Spectroscopy

1.2.1. General Background

X-ray absorption spectroscopy (XAS) involves the measurement of the absorption coefficient, μ, of an element as a function of energy. The absorption edge of an element is characterized by a sharp discontinuity in the absorption, resulting from the ionization of a core electron. Each edge occurs at a characteristic threshold energy which is specific to the absorbing element. The Bohr atomic level from which the photoionized electron originates is used to designate the absorption edge. Thus, a K-edge refers to the ionization of a 1s electron, a L_1 edge to the ionization of a 2s electron, etc.

XAS is a valuable probe of transition metal active sites in metalloproteins. Because it is element specific, XAS can be used to probe atoms specifically at the active site. Further, XAS can successfully be applied to the investigation of non-crystalline, dilute protein solutions.

XAS spectra are divided into several regions (Figure 1.1). At X-ray energies above the threshold for ionization, electrons are promoted into the continuum. Spectral data in this region, known as the EXAFS region (extended X-ray absorption fine structure), can be analyzed to obtain metrical information for the structural environment of the absorbing atom.[1] A discussion of EXAFS is beyond the scope of this thesis. For further information about the EXAFS method and applications, the reader is directed to reference 2 and references therein.

In the pre-edge and edge region the incident energy is below the ionization threshold. This region contains transitions from core levels to unoccupied or partially occupied atomic and molecular orbitals localized on the absorber, as well as to localized and delocalized continuum levels.[3] These features occur below or are superimposed on the rising edge. Throughout this thesis, features which occur at energies well-separated from the onset of the edge will be referred to as pre-edge features, while those transitions which actually overlap the rising edge intensity will be called edge or rising-edge features.

Absorption features in the pre-edge and edge region are sensitive to the local electronic and geometric environment of the absorbing atom.[4-14] The position of the absorption edge is dependent on the effective charge density at the absorbing atom. An atom with a higher effective nuclear charge has a deeper core level and, thus, a higher photon energy is needed to ionize the core electron. On this basis, to a first approximation, the position of the edge can be related to the oxidation state of the

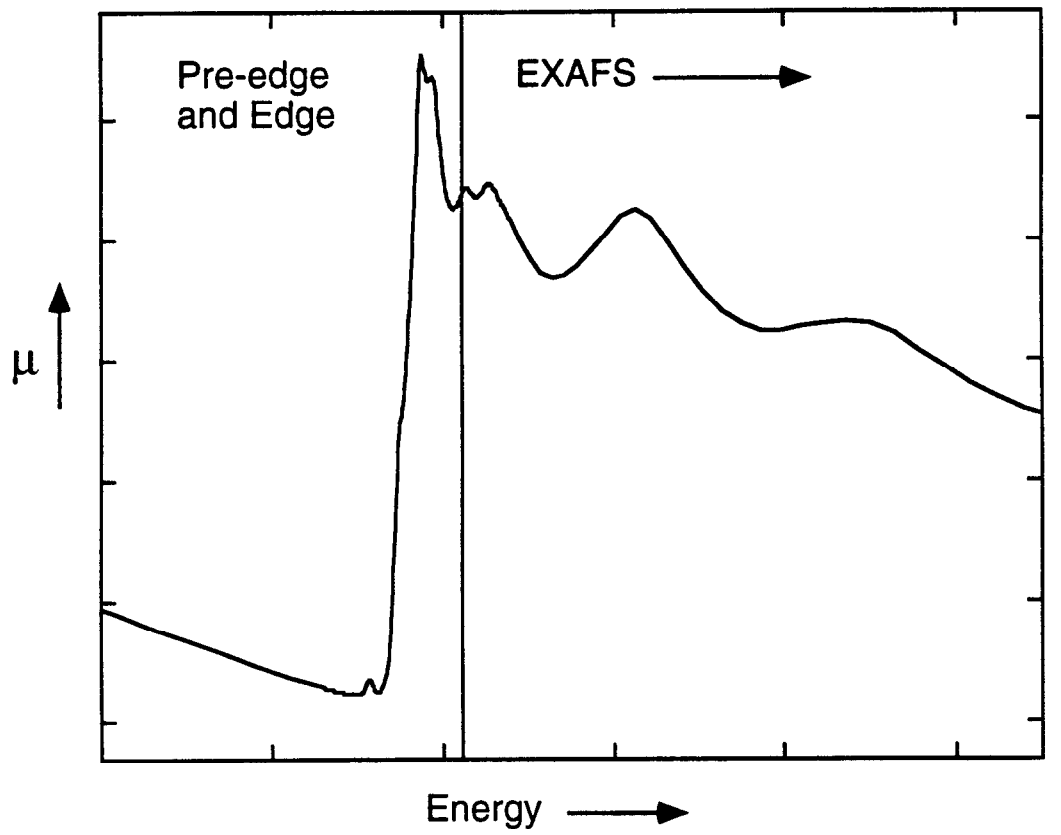

Figure 1.1. A typical X-ray absorption spectrum measured in transmission mode. μ is the absorption coefficient. The background slope in the pre-edge and EXAFS regions is in part caused by the absorption of lower Z atoms in the sample in addition to air, windows, and tape in the experimental set-up.

absorber. Further, for edges of species with the same oxidation state, variations in edge features can be related to differences in the covalent interactions in which the absorber is involved.

The bound-state transitions in the pre-edge and edge regions can be interpreted using the X-ray absorption cross section, σ, given in equation 1.1.

$$\sigma = c\left|\langle \phi_f | \hat{O} | \phi_i \rangle\right|^2 \tag{1.1}$$

where c is a constant, $\hat{O}$ is the transition moment operator, and ϕ_f and ϕ_i are the final and initial state wavefunctions, respectively. Pre-edge and edge features are governed primarily by electric dipole selection rules. The intensity of these features, then, is related to the density of final states of the appropriate symmetry which have a measurable overlap with the initial state wavefunction. Based on a dipole-coupled mechanism, the features in a K-edge spectrum reflect transitions from a core 1s orbital to p-type final states.

1.2.2. Polarized XAS

The plane polarized nature of synchrotron radiation is ideally suited for polarized XAS. Numerous studies[15-25] have demonstrated the utility of polarized XAS for investigating bound-state transitions. For polarized electric dipole transitions,[15] the absorption cross section (equation 1.1) can be rewritten as equation 1.2,

$$\sigma = c\sum_{orient}\left|\langle \phi_f | \mathbf{e}\bullet\mathbf{r} | \phi_i \rangle\right|^2 = c\sum_{orient}\cos^2\theta\left|\langle \phi_f | \mathbf{r} | \phi_i \rangle\right|^2 \tag{1.2}$$

where **e** is a unit vector coincident with the X-ray polarization direction, **r** corresponds to the x, y, or z component of the electric dipole operator and θ is the angle between the polarization and dipole matrix operator vectors. The cross section is proportional to the sum of all contributing molecular orientations in the crystal. Thus, when an oriented crystal is aligned with a known molecular orientation, the angular dependence of the intensity of a particular absorption feature may be used to determine the symmetry of the final state wavefunction. Further, specific edge or pre-edge features which are unresolved in orientationally-averaged spectra can be orientationally selected and resolved by polarized XAS.

1.2.3. Transition Metal K-edge XAS

Transition metal K-edge XAS of open-shell metal centers typically display a weak pre-edge feature, as well as some structure on the rising edge (Figure 1.1). The pre-edge feature is assigned as the formally dipole-forbidden 1s —> 3d transition which is made allowed through static or dynamic distortion of inversion symmetry, resulting in metal p-orbital mixing into the final state. Thus, the intensity of this transition can provide information about the site symmetry and electronic structure of the absorbing atom. This 1s —> 3d transition has also been shown to gain intensity through direct quadrupole coupling.[16]

The higher energy transitions which fall on the rising edge of transition metal K-edges are less well resolved, particularly in isotropic solution or powder samples. For this reason, fewer definitive assignments of the transitions in this region exist.[26] Single crystal polarized XAS, as described in the preceding section, provides a method for resolving transitions in this energy region, making assignments more accessible.[25] A detailed analysis of the shoulder observed in the polarized Cu K-edge spectra of Cu(II) systems is included in Chapter 3.

1.2.4. Ligand K-edge XAS

Most X-ray absorption edge studies have been conducted at transition metal K-edges. However, the XAS spectrum of a ligand bound to an open shell metal ion also provides information about the electronic structure of the site, and, in particular, about the ligand-metal bonding interaction.[27]

For a ligand such as chloride, bound to an open shell Cu^{2+} (d^9) ion, the ligand K-edge spectrum exhibits a well-resolved, intense pre-edge feature.[27] Figure 1.2, taken from reference 27, shows the Cl K-edge spectra of D_{4h} $CuCl_4^{2-}$, D_{2d} $CuCl_4^{2-}$ and D_{2d} $ZnCl_4^{2-}$. When the d-manifold of the metal is fully occupied, as for Zn(II), the pre-edge feature is absent.[27] This feature thus corresponds to a Cl 1s —> Cu $3d_{x^2-y^2}$ transition, where the $3d_{x^2-y^2}$ orbital is the half-occupied highest-occupied molecular orbital (HOMO) of the copper ion. However, due to the localized nature of the Cl 1s orbital, this transition can only have intensity if the $3d_{x^2-y^2}$ orbital has a significant covalent contribution of Cl p character.

A bonding interaction between the copper $3d_{x^2-y^2}$ orbital and the chloride 3p valence orbitals, shown schematically in Figure 1.3, results in the antibonding HOMO orbital, $\psi^* = \sqrt{(1-\alpha'^2)}$ Cu $3d_{x^2-y^2} - \alpha'$ Cl 3p, where α'^2 represents the Cl 3p character in

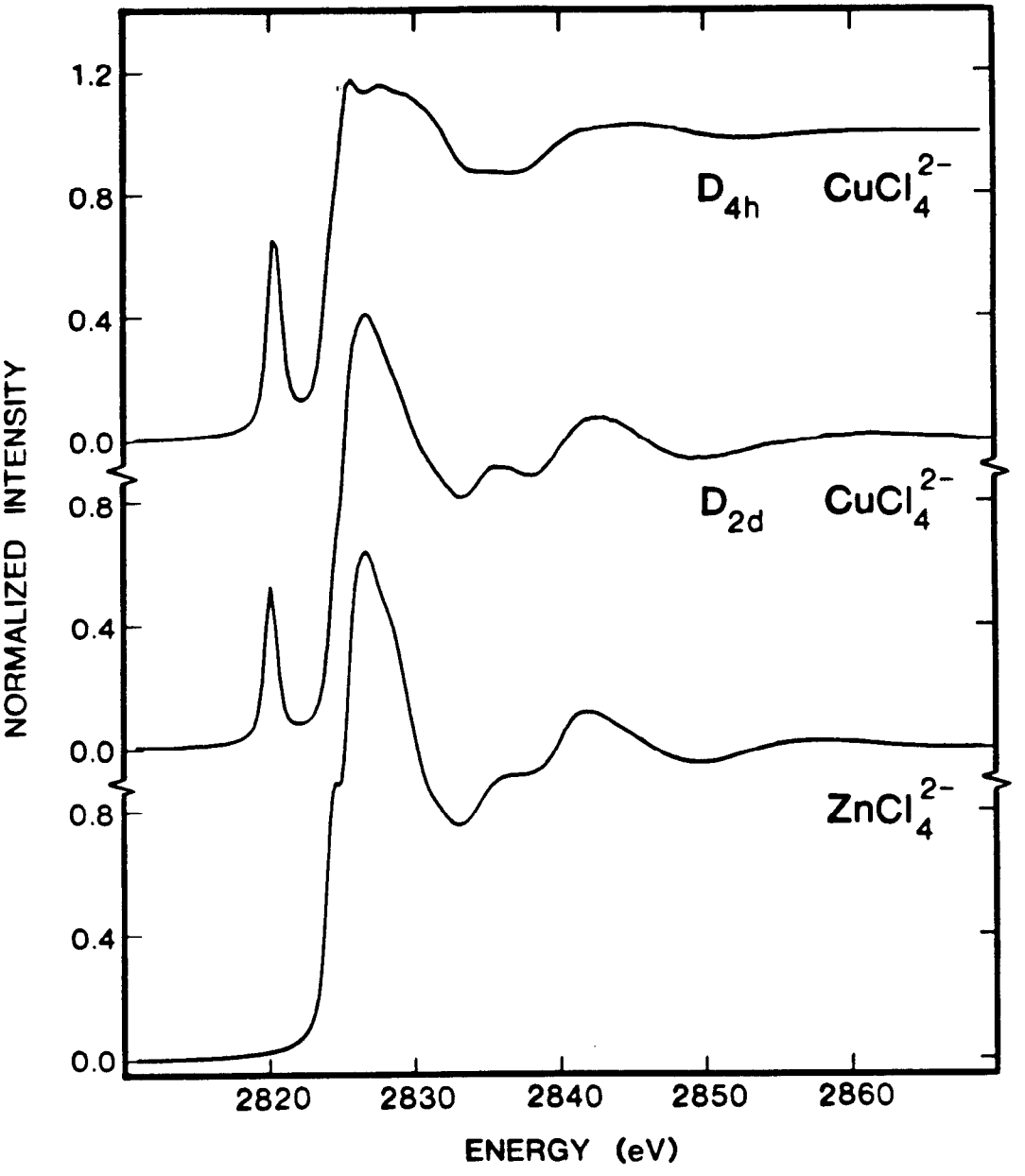

Figure 1.2. Cl K-edge XAS spectra of D_{4h} $CuCl_4^{2-}$ (top), D_{2d} $CuCl_4^{2-}$ (middle), and $ZnCl_4^{2-}$ (bottom). The spectra of chloride bound to the open shell Cu^{2+} ion exhibit an intense well-resolved pre-edge feature which is absent in the spectrum of d^{10} $ZnCl_4^{2-}$. Figure taken from ref. 27.

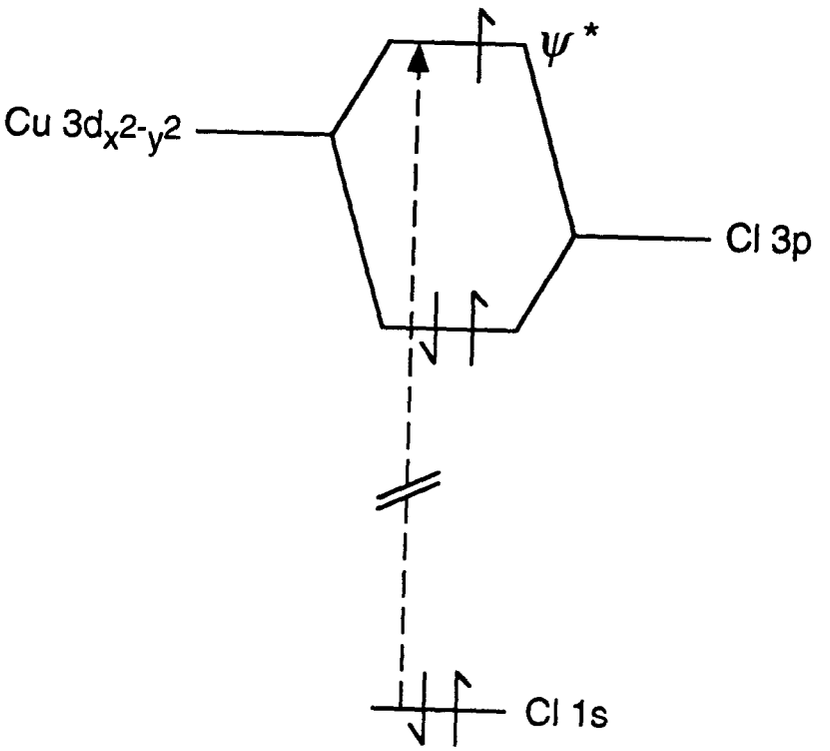

Figure 1.3. Orbital energy diagram showing the transition of the Cl 1s electron to the antibonding half-occupied ψ^* orbital.

the molecular orbital. The Cl K-edge feature is thus assigned as a Cl 1s —> ψ^* transition.[27]

Methodology has been developed[27] which relates the observed pre-edge intensity to the degree of covalent interaction between the ligands and the metal. The electric dipole intensity for this transition is given by equation 1.3a, where c is a constant and **r** is the electric dipole operator. Equation 1.3b is obtained by substitution of ψ^* as given above, combined with the fact that the transition must be localized on the Cl. Because $c|\langle \text{Cl 1s}|\mathbf{r}|\text{Cl 3p}\rangle|^2$ is simply the intensity of the pure Cl 1s —> 3p transition, the intensity observed in the pre-edge transition is the intensity of a pure Cl 1s —> 3p transition weighted by α'^2, the covalent contribution of the ligand to the antibonding orbital. This result is given in equation 1.3c.

$$\text{I(Cl 1s} \rightarrow \psi^*) = c|\langle \text{Cl 1s}|\mathbf{r}|\psi^*\rangle|^2 \quad (1.3a)$$

$$= \alpha'^2 c|\langle \text{Cl 1s}|\mathbf{r}|\text{Cl 3p}\rangle|^2 \quad (1.3b)$$

$$= \alpha'^2 \text{I(Cl 1s} \rightarrow \text{Cl 3p)} \quad (1.3c)$$

If the value of α^2 for a complex is known, equation 1.3c can be applied to the experimental pre-edge intensity to determine the value of I(Cl 1s —>3p). Then the experimental pre-edge intensity of a similar ligand-metal complex can be analyzed to determine the covalent contribution of the ligand to the HOMO orbital.

The methodology presented here is general for all ligands. It is, however, necessary to know the value of the covalency of α^2 for at least one system in order to quantitate others. Further, the straightforward relationship between intensity and covalency presented in equation 1.3c holds only for transition metal centers characterized by only one d-manifold vacancy (e.g., Cu^{2+}).

As will be demonstrated throughout this thesis, ligand K-edges enjoy several advantages over metal K-edges as a probe of electronic structure at a metal site. First, the resolution at the K-edges of Cl and S is higher than for K-edges in the hard X-ray region. The linewidth of features in the pre-edge and edge region is in part determined by the lifetime of the core hole of the absorbing species.[28] Relatively long core-hole lifetimes for low Z atoms[29] results in higher resolution. Further, improved monochromator resolution at low energies also enhances the resolution of features in the soft X-ray region. Thus, metal K-edges like Fe (~7 keV) and Cu (~9 keV) are characterized by a spectrometer resolution of ~1 and ~2 eV, respectively, while the resolution at the K-edges of Cl and S, which fall in the 2-3 keV range, is ~0.5 eV. The experimental resolution is

additionally dependent upon the vertical slit width which defines the beam height and on the crystal monochromator utilized in the experiment.

Ligand pre-edge features exhibit increased electric dipole-allowed intensity relative to features at a metal K-edge. This increased intensity is derived from the ligand p-orbital bonding interaction with the metal which creates a dipole-allowed final state. Thus, direct investigation of the details of the ligand-metal bonding interaction is possible. Ligand K-edges also have a strong advantage over traditional superhyperfine analysis of covalency in EPR spectroscopy. While EPR superhyperfine requires the ligand interacting with the metal center to have a nuclear spin, ligand K-edge spectroscopy only requires the ligand p-orbitals to undergo a bonding interaction with the metal.

1.2.5. Experimental Considerations

In this section, the general experimental considerations specific to X-ray edge spectroscopy which were used in the measurement of data for this thesis are described. In particular, the details of the low-energy set-up[30] are included. Issues which relate to the experimental design and execution of an XAS experiment, such as the choice of monochromator crystals or fluorescence detector and the elimination of undesired harmonic components in the incident beam, are described in detail elsewhere.[31,32]

The design of a basic X-ray absorption experiment is presented in Figure 1.4. Synchrotron radiation provides a tunable source of X-ray energies. The X-ray beam, which is highly vertically collimated, is further defined vertically and horizontally by pairs of slits and then monochromatized with a double-crystal monochomator. After passing through an additional set of slits designed to minimize scatter, the incident intensity is measured in a gas-filled ionization chamber. There are two basic ways in which high-energy XAS data is measured. Transmission of the X-rays by the sample is determined by measuring the X-ray flux before and after the sample using ionization chambers (I_0 and I_1 in Figure 1.4). This method is effective for concentrated solid samples. However, for dilute samples, the signal-to-noise ratio is reduced if the fluorescence signal, emitted as the excited nucleus relaxes after photoionization, is measured (FF in Figure 1.4). For K-shell excitation, the K_α emission line is measured in a configuration which places the sample at a 45° angle to the incoming beam. This allows the fluorescence signal to be measured at a 90° angle to the beam path. In both configurations, the observed quantity (transmitted or fluorescent intensity) is ratioed by the incident intensity to correct for any instability in the synchrotron source.

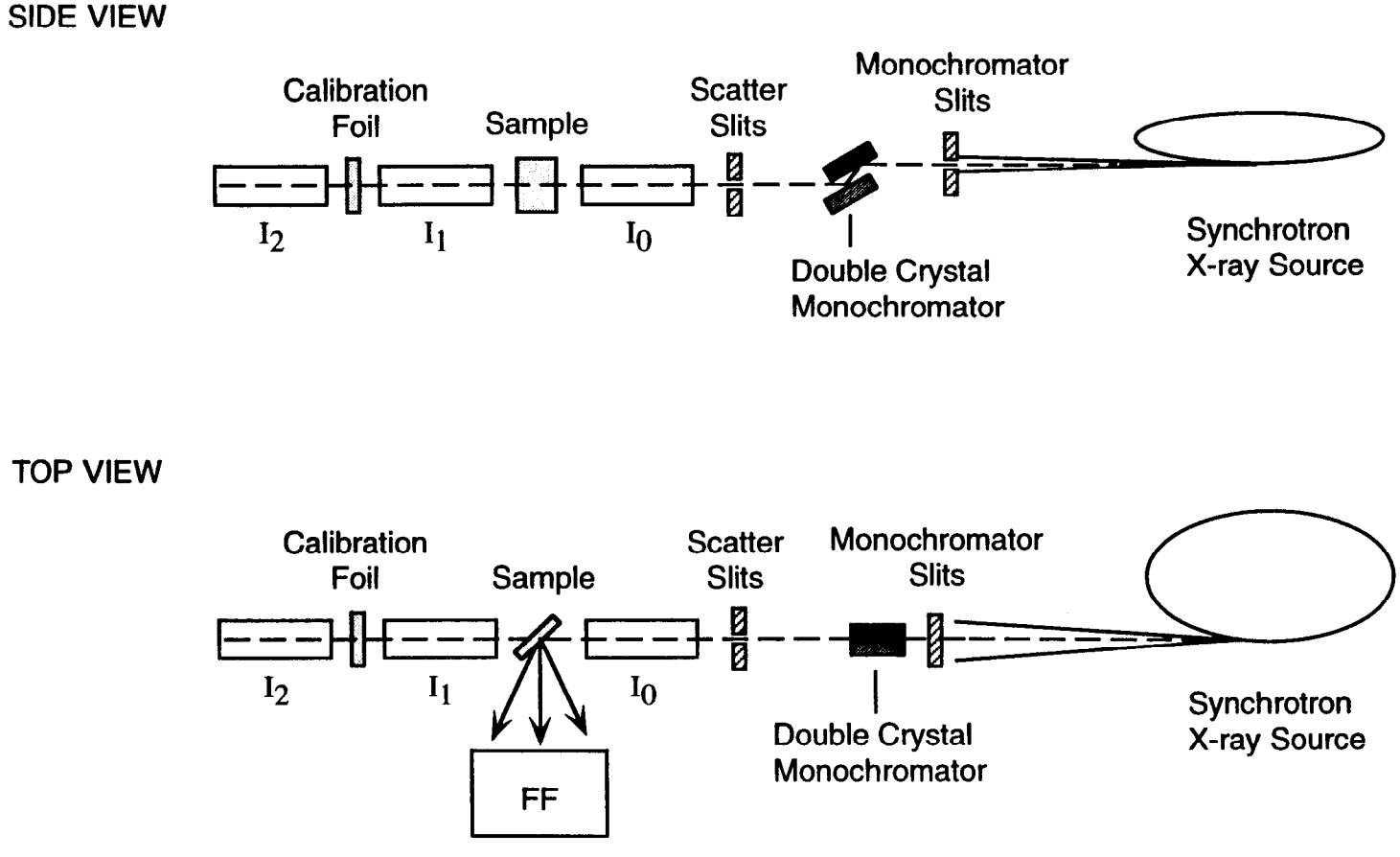

Figure 1.4. Side and Top views of the experimental design for a typical XAS measurement in the hard X-ray region. See text for a description of the set-up.

In high energy experiments, a third ionization chamber (I_2 in Figure 1.4) is placed behind I_1 and a foil of the element being measured is placed before I_2. Measurement of the transmitted intensity of the foil (using I_1 as the incident intensity) allows an internal calibration measurement to be made at the same time as the sample measurement.

Beyond the basic experimental design, a most important consideration in X-ray edge spectroscopy is the resolution of the experiment. For a given monochromator, the resolution is controlled through the use of the defining slits placed before the monochromator. For the edge experiments described in this thesis, the slits were set to optimize the spectral resolution at a vertical height of 1 mm. By limiting the vertical height of the beam, the experimental resolution is limited primarily by other factors such as the intrinsic resolution of the monochromator and the core-hole lifetime of the absorber. The resolution is also, in principle, affected by mirrors in the optical path of the beam. The experiments described herein were performed on beam lines where mirrors were not present or were used in such a way that degradation of resolution did not occur.[27]

Low energy experiments have several important differences from those designed for measurements in the hard X-ray region. The X-ray beam at energies between 2-3 keV can not penetrate air or sample. As a result, transmission measurements are not possible. Thus, all measurements at low energy are conducted in fluorescence mode and calibration involves measurement of a calibration sample at regular intervals between sample measurements. The experimental set up used for low energy experiments is shown schematically in Figure 1.5. The beam path is entirely enclosed in a He atmosphere, which does not significantly attenuate the beam or the fluorescence. A flexible section of tubing is attached directly to the beam pipe *via* a snug-fitting ring. This tubing is connected to a large plexiglass box containing a fluorescence screen with vertical motion (used for alignment of the apparatus with respect to the beam) and a set of scatter slits which can be manipulated from outside the plexiglass box. The plexiglass box is then attached directly to the ionization chamber used for measurement of incident intensity. Another section of flexible tubing connects the ionization chamber to the front of an aluminum box which holds the sample. An optimized ion chamber detector[33,34] is used for fluorescence detection and is attached directly to the sample box, without the Soller slits generally used at high energies.[33] The only windows in this set up are the window at the end of the beam pipe, and a 6.3 μm polypropylene window at the front of the sample box. This effectively separates the sample space from the "I_0 section". Each space is purged with a separate He gas supply.

TOP VIEW

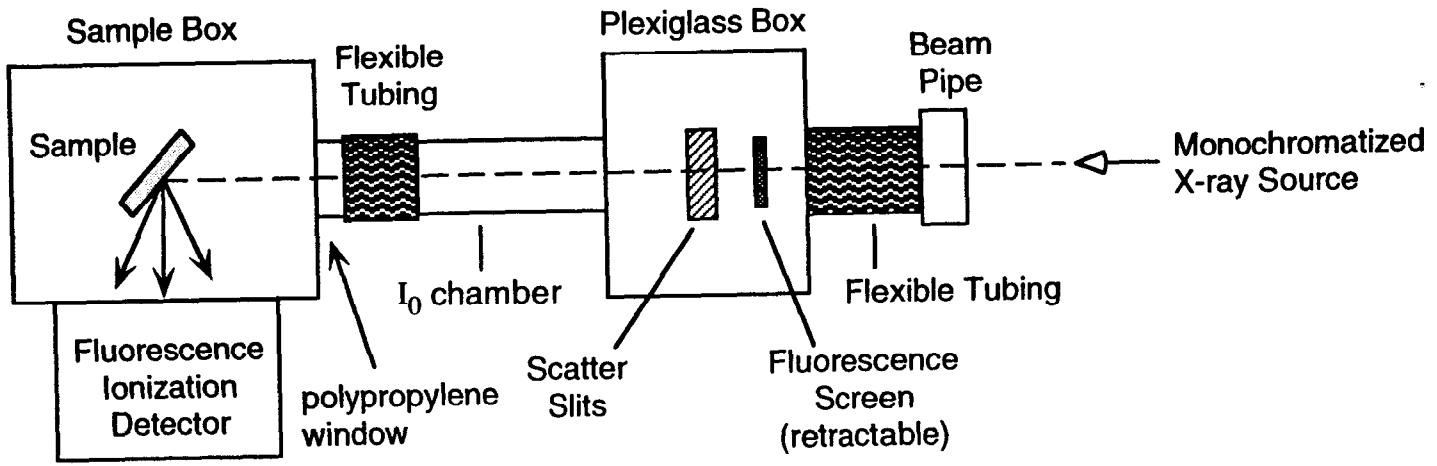

Figure 1.5. Top view of the experimental design used in this work for XAS measurements in the soft X-ray region. See text for a description of the set-up.

1.2.6. Data Reduction

The initial step in the reduction of XAS edge data is the energy calibration of each scan. The reproducibility in energy position is better than 0.2 eV, as determined by comparison of first and second derivatives of spectra for model compounds measured during different experimental sessions.[30] After the inspection of individual scans for consistency, like sample scans are averaged.

As seen in Figure 1.1, the absorption of a sample in an XAS spectrum is superimposed on scatter from the sample and the absorption of lower Z atoms in the sample, as well as absorption from windows, tape, or air in the beam path. To obtain the absorption of the species of interest, the background absorption is approximated by fitting a linear or second order polynomial function to the pre-edge or post-edge region. This function is extrapolated and subtracted from the entire spectrum.

In order to compare absorption intensities from one spectrum to another, the data is normalized. This procedure scales the edge jump intensity to a value of 1.0 and allows the data to be interpreted on a per-atom basis. Variations in structure in the edge region are dependent on the structural and electronic environment of the absorber. Thus, the point at which the data is scaled must lie above the edge region so that the normalization procedure is independent of the nature of the sample. A linear or nearly-flat polynomial is fit to the post-edge region and the value of that function is generally defined as 1.0 at E_0, where E_0 is the beginning of the continuum region of the XAS spectrum.

1.3. SCF-Xα-SW Calculations

The self consistent field-Xα-scattered wave (SCF-Xα-SW) method[35-45] is an iterative technique for calculating one-electron energies and wavefunctions using Slater's statistical approximation for exchange[46,47] and the scattered wave formalism developed by Johnson. It has been successfully applied to understand the electronic structure and dependent properties of a large number of molecular systems. As the method has been extensively reviewed,[35-38,46] the background given here is designed only to give the reader a basic understanding of the components of the method.

Xα theory uses an approximation to the exchange potential, given by equation 1.4, based on Slater's statistical exchange approximation.[46,47]

$$V_{X\alpha} = -6\alpha\left(\frac{3\rho}{8\pi}\right)^{1/3} \qquad (1.4)$$

where α is an adjustable parameter and ρ is the electron density as a function of the atomic coordinates. Equation 1.4 applies to "spin restricted" calculations for which the spin up and spin down orbitals are required to be degenerate ($\rho\uparrow = \rho\downarrow$). The value of α used in these calculations is that determined by Schwarz[48,49] by matching the $X\alpha$ solutions to those of hyper-Hartree-Fock calculations.

The scattered wave (SW) formalism[35-45] involves modeling a molecule as a cluster of spheres (also known as "the muffin tin" approximation). The cluster is divided into three regions: region I is bounded by the atomic spheres, region II is the "interatomic" region outside the atomic spheres but inside an outer sphere which surrounds the whole cluster, and region III is the "extramolecular" region outside the outer sphere. For anionic or cationic molecules, a charged "Watson sphere", coincident with the outer sphere, is normally included to approximate the stabilizing effect of surrounding counterions.[50]

In regions I and III the potential is spherically averaged (constant for a given distance from the center of the sphere). In region II the potential is volume averaged (constant throughout the region). For very large planar molecules the large volume of region II results in eigenvalues which are, in general, too low.[35] The relative energy ordering is, however, preserved. It is thus best to minimize the volume of region II if possible. The α values chosen for the molecular calculation are those of the individual atoms for region I. Within regions II and III, an average of the atomic α values, weighted by the number of valence electrons, is used for α. The wavefunction in regions I and III are expanded in terms of spherical harmonics and the wavefunction in region II is expressed as a linear combination of waves incident upon and scattered by the atomic spheres.

A starting potential for the cluster is generated from a superposition of the charge densities of each atom or ion in the cluster. A set of coupled linear equations result from the condition that the wavefunctions and their first derivatives must be continuous at the region boundaries. Determination of the energies which satisfy these equations gives a set of eigenvalues and eigenfunctions for the one-electron Schrödinger equation. These eigenfunctions are used to calculate new charge densities and then a new potential, which is combined in a weighted average with the previous potential and used to generate new eigenvalues and eigenfunctions. The process is repeated until self consistency is reached.

The resulting wavefunctions can be expressed in a manner similar to a linear combination of atomic orbitals (LCAO). To do this, electron density from regions II and III must be repartitioned among the atomic spheres using the method of Case and Karplus.[51]

The Slater transition state formalism[42,46,47] is utilized in Xα-SW to calculate transition energies. The method involves manually removing half an electron from the orbital of origin and placing half an electron in the orbital of destination. The potential is then converged for this configuration and the transition energy is equated to the difference between the eigenvalues of the two partially occupied orbitals. This technique provides the advantage that relaxation energy is partially accounted for in the calculation of transition energies.[42,46,47]

There are disadvantages to the use of the statistical exchange approximation, including the lack of a direct correspondence between the total energy and a total wavefunction. As Xα produces a single Slater determinant, there is no total wavefunction. The energies calculated by Xα for a given configuration may not be related to a specific state, but will correspond to a weighted average of the energies of the states generated by that configuration.[42,44] Further, the dependence of the calculation on the parameter α and on the choice of sphere radii is also problematic.

The criteria which determine the choice of sphere radii for the atomic spheres which define region I are not well-defined. A commonly used set of criteria is that proposed by Norman,[52] in which the ratios of radii required to encompass an electronic charge equal to the nuclear charge remain constant. For the calculations described herein, the sphere radii begin with the Norman criteria and are then adjusted until the calculation reproduces an experimental parameter (such as an optical transition energy), while requiring matched potentials at the sphere boundaries. In other cases, the sphere radii are chosen to be the same as for a molecule to which close comparisons will be made.

The Xα method does enjoy certain advantages over other calculations. It strictly satisfies Fermi statistics.[42,44] Furthermore, in the limit of infinite interatomic distances, the total energy of the system becomes the sum of the individual atomic energies. As described, the use of Slater's transition state formalism allows the partial inclusion of relaxation energy in the calculation of transition energies. Most importantly, it requires relatively little computational time which is particularly advantageous for systems like transitions metal centers with many electrons.

1.4. References

(1) Stern, E. A. In *X-ray Absorption: Principles, Applications, Techniques of EXAFS, SEXAFS, and XANES*; Koningsberger, D. C.; Prins, R., Ed.; John Wiley & Sons: New York, 1988; pp 1-52.

(2) *X-ray Absorption: Principles, Applications, Techniques of EXAFS, SEXAFS, and XANES*; Koningsberger, D. C.; Prins, R., Ed.; John Wiley & Sons: New York, 1988.

(3) Bianconi, A. In *X-ray Absorption: Principles, Applications, Techniques of EXAFS, SEXAFS, and XANES*; Koningsberger, D. C.; Prins, R., Ed.; John Wiley & Sons: New York, 1988; pp 573-662.

(4) Srivastava, U. C.; Nigam, H. L. *Coord. Chem. Rev.* **1973**, *9*, 275-310, and references therein.

(5) Agarwal, B. K.; Bhargava, C. B.; Vishnoi, A. N.; Seth, V. P. *J. Phys. Chem. Solids* **1976**, *37*, 725-728.

(6) Kostroun, V. O.; Fairchild, R. W.; Kukkonen, C. A.; Wilkins, J. W. *Phys. Rev. B* **1976**, *13*, 3268-3271.

(7) Schulman, R. G.; Yafet, Y.; Eisenberger, P.; Blumberg, W. E. *Proc. Natl. Acad. Sci. (USA)* **1976**, *73*, 1384-1388.

(8) Belli, M.; Scafati, A.; Bianconi, A.; Mobilio, S.; Pallandino, L.; Reale, A.; Burattini, E. *Solid State Commun.* **1980**, *35*, 355-361.

(9) Kutzler, F. W.; Hodgson, K. O.; Doniach, S. *Phys. Rev. A* **1982**, *26*, 3020-3022.

(10) Grunes, L. A. *Phys. Rev. B* **1983**, *27*, 2111-2131.

(11) Sham, T. K. *J. Am. Chem. Soc.* **1983**, *105*, 2269-2273.

(12) Cramer, S. P.; Eccles, T. K.; Kutzler, F. W.; Hodgson, K. O.; Mortenson, L. E. *J. Am. Chem. Soc.* **1976**, *98*, 1287-1288.

(13) Horsley, J. A. *J. Chem. Phys.* **1982**, *76*, 1451-1458.

(14) Bair, R. A.; Goddard, W. A., III *Phys. Rev. B* **1980**, *22*, 2767-2776.

(15) Hahn, J. E.; Hodgson, K. O. *ACS Symp. Ser.* **1983**, *211*, 431-444.

(16) Hahn, J. E.; Scott, R. A.; Hodgson, K. O.; Doniach, S.; Desjardins, S. R.; Solomon, E. I. *Chem. Phys. Lett.* **1982**, *88*, 595-598.

(17) Scott, R. A.; Hahn, J. E.; Doniach, S.; Freeman, H. C.; Hodgson, K. O. *J. Am. Chem. Soc.* **1982**, *104*, 5364-5369.

(18) Templeton, D. H.; Templeton, L. K. *Acta Crystallogr., Sect. A* **1980**, *36*, 237-241.

(19) Templeton, D. H.; Templeton, L. K. *Acta Crystallogr., Sect. A* **1982**, *38*, 62-67.

(20) Heald, S. M.; Stern, E. A. *Phys. Rev. B* **1978**, *17*, 4069-4081.

(21) Stern, E. A.; Sayers, D. E.; Dash, J. G.; Shechter, H.; Bunker, B. *Phys. Rev. Lett.* **1977**, *38*, 767-770.

(22) Stern, E. A.; Sayers, D. E.; Lytle, F. W. *Phys. Rev. Lett.* **1976**, *37*, 298-301.

(23) Cox, A. D.; Beaumont, J. H. *Philos. Mag. B* **1980**, *42*, 115-126.

(24) Kutzler, F. W.; Scott, R. A.; Berg, J. M.; Hodgson, K. O.; Doniach, S.; Cramer, S. P.; Chang, C. H. *J. Am. Chem. Soc.* **1981**, *103*, 6083-6088.

(25) Smith, T. A.; Penner-Hahn, J. E.; Berding, M. A.; Doniach, S.; Hodgson, K. O. *J. Am. Chem. Soc.* **1985**, *107*, 5945-5955.

(26) Kau, L. S.; Spira-Solomon, D. J.; Penner-Hahn, J. E.; Hodgson, K. O.; Solomon, E. I. *J. Am. Chem. Soc.* **1987**, *109*, 6433-6442.

(27) Hedman, B.; Hodgson, K. O.; Solomon, E. I. *J. Am. Chem. Soc.* **1990**, *112*, 1643-1645.

(28) Cowan, R. D. *The Theory of Atomic Structure and Spectra*; University of California Press: Berkeley, CA, 1981, pp 18-19.

(29) Krause, M. O.; Oliver, J. H. *J. Phys. Chem. Ref. Data.* **1979**, *8*, 329-338.

(30) Hedman, B.; Frank, P.; Gheller, S. F.; Roe, A. L.; Newton, W. E.; Hodgson, K. O. *J. Am. Chem. Soc.* **1988**, *110*, 3798-3805.

(31) Scott, R. A. *Meth. Enzymol.* **1985**, *117*, 414-459.

(32) Heald, S. M. In *X-ray Absorption: Principles, Applications, Techniques of EXAFS, SEXAFS, and XANES*; Koningsberger, D. C.; Prins, R., Ed.; John Wiley & Sons: New York, 1988; pp 87-118.

(33) Lytle, F. W.; Greegor, R. B.; Sandstrom, D. R.; Marques, E. C.; Wong, J.; Spiro, C. L.; Huffman, G. P.; Huggins, F. E. *Nucl. Instrum. Meth. Phys. Res.* **1984**, *226*, 542-548.

(34) Stern, E. A.; Heald, S. M. *Rev. Sci. Instrum.* **1979**, *50*, 1579-1582.

(35) Connolly, J. W. D. In *Semiempirical Methods of Electronic Structure Calculation, Part A: Techniques*; Segal, G. A., Ed.; Plenum: New York, 1977; pp 105-132.

(36) Johnson, K. H. *Ann. Rev. Phys. Chem.* **1975**, *26*, 39-171.

(37) Johnson, K. H. *Adv. Quantum Chem.* **1973**, *7*, 143-185.

(38) Johnson, K. H.; Norman, J. G., Jr.; Connolly, J. W. D. In *Computational Methods for Large Molecules and Localized States in Solids*; Herman, F.; McLean, A. D.; Nesbet, R. K., Ed.; Plenum: New York, 1973; pp 161-201.

(39) Slater, J. C. *J. Chem. Phys.* **1965**, *43*, S228.

(40) Johnson, K. H. *J. Chem. Phys.* **1966**, *45*, 3085-3095.

(41) Johnson, K. H.; Smith, F. C., Jr. *Phys. Rev. B* **1972**, *5*, 831-843.

(42) Slater, J. C.; Johnson, K. H. *Phys. Rev. B* **1972**, *5*, 844-853.

(43) Weinberger, P.; Schwarz, K. In *International Review of Science, Physical Chemistry, Ser. Two, Vol. 1*; Buckingham, A. D.; Coulson, C. A., Ed.; Butterworth: London, 1975; pp 255-282.

(44) Slater, J. C. *The Calculation of Molecular Orbitals*; Wiley: New York, 1979.

(45) Case, D. A. *Ann. Rev. Phys. Chem.* **1982**, *33*, 151-171.

(46) Slater, J. C. *Adv. Quantum Chem.* **1972**, *6*, 1-92.

(47) Slater, J. C. *Quantum Theory of Molecules and Solids*; McGraw-Hill: New York, 1974; Vol. 4.
(48) Schwarz, K. *Phys. Rev. B* **1972**, *5*, 2466-2468.
(49) Schwarz, K. *Theoret. Chim. Acta* **1974**, *34*, 225-231.
(50) Watson, R. E. *Phys. Rev* **1958**, *111*, 1108-1110.
(51) Case, D. A.; Karplus, M. *Chem. Phys. Lett.* **1976**, *39*, 33-38.
(52) Norman, J. G., Jr. *Mol. Phys.* **1976**, *31*, 1191-1198.

Chapter 2

Ligand K-edge X-ray Absorption Spectroscopic Studies of Ligand-Metal Bonding: Charge Donation and Covalency in Copper-Chloride Systems

2.1. Introduction

Insight into the electronic structure of an absorbing atom is obtained from an analysis of X-ray absorption edge spectra,[1,2] as demonstrated for transition metal centers such as Cu, Fe, Ni and Mo at the metal K-edges.[3-6] It has also been shown that ligand absorption edges can be used to probe electronic structure of transition metal complexes.[7]

A representative K-edge absorption spectrum for a chloride ligand bound to an open shell cupric d^9 ion is shown in Figure 2.1. The pre-edge feature, well separated from the rising edge, is absent in metal systems with a full d-manifold and is assigned as the Cl 1s —> Cu $3d_{x^2-y^2}$ transition, where the $3d_{x^2-y^2}$ orbital is the half-occupied, highest-occupied molecular orbital (HOMO).[7] Figure 2.2 shows an energy level diagram depicting the transition which gives rise to the pre-edge spectral feature. As described in Chapter 1, because of the localized nature of the Cl 1s orbital, this transition can have absorption intensity only if the HOMO orbital contains a significant component of Cl 3p character as a result of covalency. The electric dipole intensity observed in this pre-edge transition is simply the intensity of the pure dipole-allowed Cl 1s —> 3p transition weighted by α^2, the covalent contribution of the ligand to the HOMO (equation 1.3c). Thus, the pre-edge intensity provides a direct probe of ligand-metal covalency due to bonding.[7] (See Chapter 1, Section 1.2.4).

As indicated in Figure 2.2, a combination of factors affect the energy position of a pre-edge transition. A shift in the core Cl 1s energy, which is related to the relative charge on the chloride, results in a change in the observed pre-edge energy. More charge donation to the metal results in a shift of the Cl 1s core to deeper binding energy (*vide infra*). In addition, the energy of the pre-edge transition is affected by the HOMO orbital energy which has two contributions. First, the geometry of the ligand field of the complex determines the d-orbital energy splitting pattern and thus contributes to the HOMO orbital energy. Second, the overall d-manifold can shift in energy. This is related to both the coordination number of the metal (the total antibonding and repulsive interactions with the ligands) and the effective charge on the metal, which affects the energy of all the metal orbitals.

At higher energy in Figure 2.1 are absorption edge features due to transitions to bound states higher in energy than the HOMO. The intense electric dipole-allowed transitions which give rise to the main edge jump are Cl 1s —> 4p transitions.

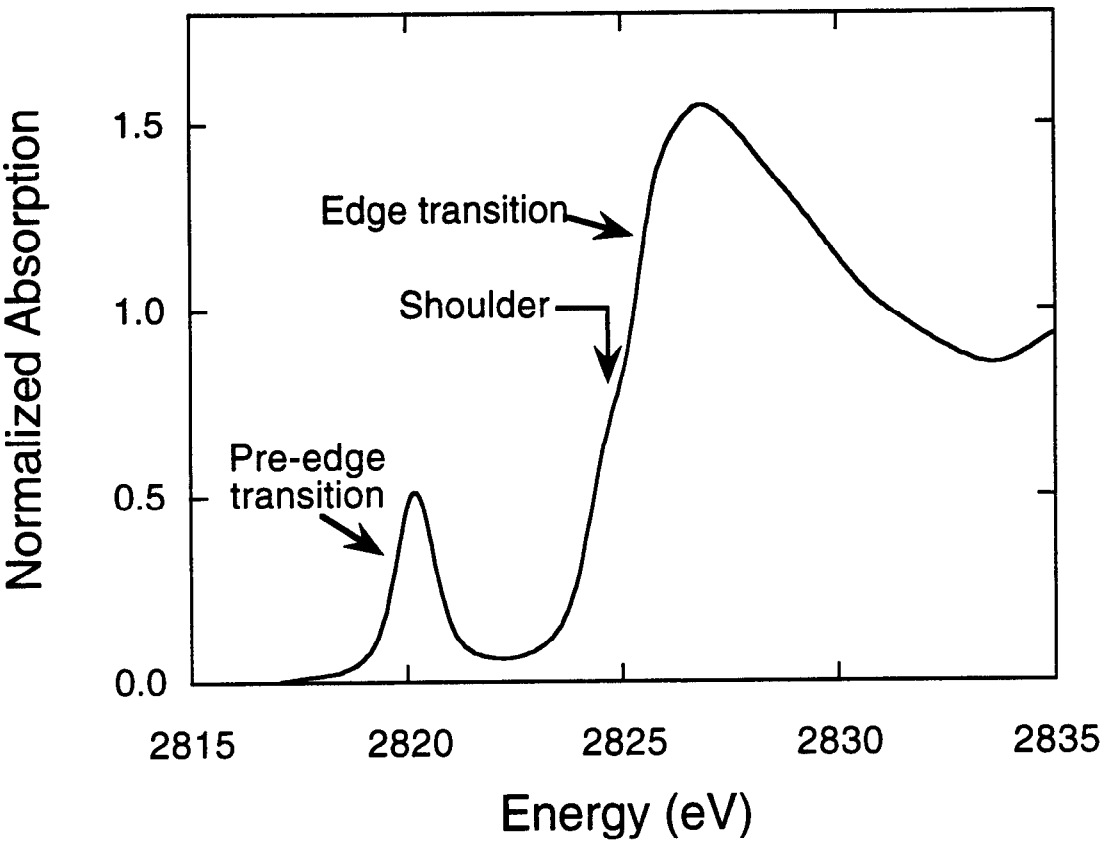

Figure 2.1. The pre-edge and edge region of a typical Cl K-edge absorption spectrum for a Cl bound to an open shell metal ion. (Shown here is the Cl K-edge for Cs_2CuCl_4). Shown are the intense, well-resolved pre-edge feature, the main edge transition, and a shoulder which occurs on the rising edge.

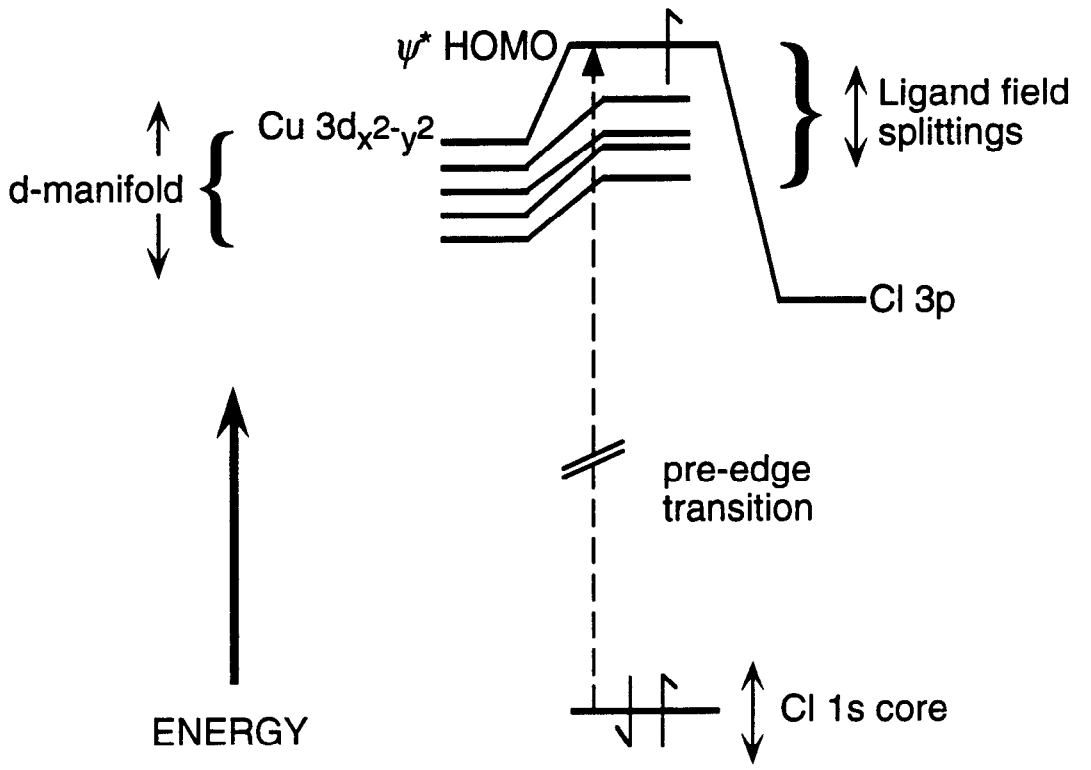

Figure 2.2. Schematic representation of the contributions to the pre-edge transition energy. The pre-edge energy is determined both by shifts in the Cl 1s core energy and in the energy of the HOMO of the complex. The HOMO orbital energy is determined by overall shifts in the d-manifold (related to coordination number and charge on the metal) as well as by the specific repulsive interaction of the HOMO orbital (determined by the ligand field of the complex).

Transitions to molecular orbitals with both Cl 3p and metal (e.g. 4s) character can appear as shoulders on the rising edge. The energy of the main edge transition, which can be determined in some cases from the rising edge inflection point, has been shown to be linearly related to the charge on the absorber.[8-10] The binding energies of core electrons undergo chemical shifts which relate to changes in the valence electron distribution due to bonding. More negative charge on the Cl will result in the core 1s energy shifting to lower binding energy; delocalization of Cl electron density due to bonding results in a core orbital shift to deeper binding energy. Since the unoccupied Cl 4p orbitals are less effected by charge donation, shifts in the rising edge inflection energy *directly* reflect shifts in the Cl 1s core in response to the effective charge on the atom.

In this study, the relationship between pre-edge intensity and covalency is used (equation 1.3c) to further develop the application of pre-edge intensity to quantitate the ligand-metal covalency in transition metal complexes. Development of a quantitative analysis of the pre-edge and edge energies for ligand K-edge spectra is presented. This analysis, based on the model described above, allows the contributions to the pre-edge transition energy from both the Cl 1s core and the HOMO shifts to be determined. The Cl 1s core shift is quantitated from energy shifts in the edge transition. Ligand field contributions to the HOMO energy are determined from optical spectra. By correcting the observed pre-edge energy for these effects, the contribution to the pre-edge energy from energy shifts of the d-manifold can be determined. In several cases, independent methods confirm the results of this methodology.

This energy and intensity analysis is applied to Cl K-edge absorption spectra for a series of Cl-Cu(II) complexes. This simple ligand-metal system allows us to determine the electronic and geometric structural basis for trends observed in the ligand K-edge spectra. The structural variations which are examined include the distortion of the $CuCl_4^{2-}$ ion from a square planar (D_{4h}) to a distorted tetrahedral (D_{2d}) geometry, the substitution of pyrazoles for two chloride ligands in a square planar complex, and the addition of a fifth ligand to tetrachlorocuprate, generating the square pyramidal $CuCl_5^{3-}$ complex. Studies of planar and tetrahedrally-distorted $Cu_2Cl_6^{2-}$ dimers compare terminal to bridging chlorides in two geometric environments. Spectra for dimers which contain square pyramidal coppers coordinated primarily by N/O ligands and either bridging or terminal chloride allow the resolution of features of bridging *vs.* terminal chlorides which can then be related to systems with both types of chloride involved in bonding.

2.2. Experimental

2.2.1. Sample Preparation.

All model compounds were prepared according to published methods: $(creatininium)_2CuCl_4$,[11] Cs_2CuCl_4,[12,13] $CuCl_2$(N-phenyl-3,5-dimethyl pyrazole)$_2$,[14] (N(2amet)pipzH_3)$CuCl_5 \cdot 2H_2O$) [N(2amet)pipzH_3 = (N-(2-ammonioethyl)-piperazinium)],[15] $KCuCl_3$,[16] $(Ph_4P)CuCl_3$,[17] $[Cu_2(PAP6Me)(OH)Cl_3] \cdot H_2O$ [PAP6Me = 1,4-di(6'-methyl-2'-pyridyl)aminophtalazine)],[18] $[Cu_2(L\text{-}O^-)Cl]$-$[BPh_4]_2 \cdot CH_3COCH_3$ [(where L-O^- is a binucleating ligand providing 2 pyridyl nitrogens and a tertiary amine nitrogen to each Cu and a bridging phenolate oxygen)].[19] The starting material for $[Cu_2(L\text{-}O^-)Cl][BPh_4]_2 \cdot CH_3COCH_3$ was generously provided by Dr. Kenneth Karlin.

The samples for the X-ray absorption experiments were ground into a fine powder which was thinly dispersed on mylar tape (containing an acrylic adhesive determined to be free of chlorine contaminants). We have verified that this procedure minimizes self-absorption effects in the data by systematically testing progressively thinner samples until the observed intensity no longer varies with the thickness of the sample. Samples were prepared identically to those in which self-absorption was shown to be negligible. The powder on tape was mounted across the window of an aluminum plate. The $[Cu_2\text{-}(L\text{-}O^-)Cl]$-$[BPh_4]_2 \cdot CH_3COCH_3$ sample was prepared in a dry, inert atmosphere. A polypropylene film window protected the sample from exposure to air.

2.2.2. X-ray Absorption Measurements and Data Acquisition Parameters.

X-ray absorption data were measured at the Stanford Synchrotron Radiation Laboratory using the 54-pole wiggler beamline 6-2 in low magnetic field mode (5 kG) with a Pt-coated focusing mirror and a Si(111) double crystal monochromator, under dedicated conditions (3.0 GeV, ~50 mA). Some data were measured on beamline X10C at the National Synchrotron Light Source (2.5 GeV, 200 mA). The monochromator was in both cases detuned ~30% to eliminate higher harmonic components in the X-ray beam. Details of the optimization of this set-up for low energy studies have been described in Chapter 1 (Section 1.2.5) as well as in an earlier publication.[20]

The data were collected as fluorescence excitation spectra utilizing an ionization chamber as a fluorescence detector.[21,22] Several scans (2-3) were measured for each sample. The energy was calibrated from the Cl K-edge spectra of Cs_2CuCl_4, run at

intervals between the samples. The maximum of the first edge-region feature in the spectrum was assigned to 2820.20 eV. Scans ranged from 2740 to 3100 eV, with a step size of 0.08 eV in the edge region for most samples. Several samples (D_{4h} $CuCl_4^{2-}$, $CuCl_5^{3-}$ and $KCuCl_3$) had a larger pre-edge step size of 0.2 eV. The spectrometer resolution was ~0.5 eV. Calculating and comparing first and second derivatives for model compounds measured during different experimental sessions results in a reproducibility in edge position of ~0.1 eV for these experiments.

2.2.3. Data Analysis.

Data were averaged and a smooth background was removed from all spectra by fitting a polynomial to the pre-edge region and subtracting this polynomial from the entire spectrum. Normalization of the data was accomplished by fitting a flat polynomial or straight line to the post-edge region and normalizing the edge jump to 1.0 at 2840 eV.

The inflection point of the rising edge for each Cl K-edge spectrum was determined from the energy of the maximum of the first derivative of the data in the rising edge region. In spectra with overlapping peaks in the first derivative, the highest energy peak in the rising edge region was used in comparisons.

2.2.4. Fitting Procedures.

The intensity of pre-edge features were quantitated by fits to the data. The fitting program EDG_FIT, which utilizes the double precision version of the public domain MINPAK fitting library[23] was used. EDG_FIT was written by Dr. Graham N. George of the Stanford Synchrotron Radiation Laboratory. All spectra were fit over the range 2818-2826 eV. Pre-edge features were modeled by pseudo-Voigt line shapes (simple sums of Lorentzian and Gaussian functions). This line shape is appropriate as the experimental features are expected to be a convolution of the Lorentzian transition envelope[24] and the Gaussian lineshape imposed by the spectrometer optics.[21,25,26] A fixed 50:50 ratio of Lorentzian to Gaussian contribution for the pre-edge feature successfully reproduced these spectral features.

Functions modeling the background underneath the pre-edge features were chosen empirically to give the best fit. The rising edge was mimicked by combinations of pseudo-Voigt line shapes (of varying admixtures). In some cases a step function was included. The number and positions of the functions used were chosen based on the

features evident in the second derivative of the spectrum. In all cases the minimum number of functions required to successfully reproduce the data were utilized.

The second derivative of the data was compared to the second derivative of the fit. In all cases, a number of fits were obtained which reproduced the data and the second derivative. The value reported for the area of a fitted feature (where peak area was approximated by the height x full-width-at-half-maximum (FWHM)) is the average of all the pseudo-Voigts which successfully fit the feature. For each sample, the standard deviation of the average of the areas was calculated to quantitate the error. In several cases the second derivative of the data was not of sufficient quality to be used to define the goodness of fit. In these cases, the fits were made only to the data. Because the fit to the second derivative of the data is most sensitive to the FWHM of the fitting function, the FWHM for these samples was stepped through the entire range of values found for the model systems with well-behaved second derivatives. The area and standard deviation reported are from the set of fits produced in this way. In the cases where the pre-edge contained overlapping features, the average area and standard deviation for each feature was determined separately as described above. The standard deviation of these area values was carried through in any analysis which utilized the fitted peak areas.

2.2.5. Determination of Rising Edge Positions.

The energies reported for the rising edge position were determined from the maximum in the first derivative of the data corresponding the rising edge inflection point. These measurements were performed independently of the above described fitting procedures.

2.2.6. Error Analysis.

There are several possible sources of systematic error in the analysis of these spectra. Normalization procedures can introduce a 1-3% difference in pre-edge peak heights, as determined by varying the parameters used to normalize a set of Cl K-edge spectra such that the final fits met requirements of consistency. This maximum of ~3% error and the error resulting from the fitting procedure discussed above (Section 2.2.4) were taken into account in the calculation of pre-edge intensities and subsequent determinations of covalency. Experimental self-absorption could, in principle, result in an artificially low observed intensity. However, care was taken to avoid self-absorption in these experiments (*vide supra*), and this effect is assumed to be negligible.

The uncertainty in pre-edge and edge energies is limited by the reproducibility of the edge spectra (~0.1 eV). Thus, relative energies of features are reported with an error of ± 0.1 eV. For pre-edge features with overlapping energies, the error in the energy position was determined from fits to the data in the manner described above (Section 2.2.4). The centers of ligand field spectra were used to quantitate energy shifts of HOMO orbitals for complexes with unassigned ligand field spectra. The error in this approximation has been determined to be ~0.2 eV from comparison of the centers of assigned ligand field spectra to the HOMO shift determined from the assigned transitions. It was assumed that there is no error in the HOMO shifts for those determined from assigned ligand field spectra.

2.3. Results of X-ray Absorption Experiments

Figure 2.3 shows the Cl K-edge X-ray absorption spectra of the inorganic compounds $NaClO_4$, $KClO_3$, and KCl, as well as the first derivatives of these spectra. The inflection point of the rising edge, determined by the energy of the maximum in the first derivative, ranges over almost 10 eV for this series of complexes. The inflection point is lowest for KCl at 2824.8 eV (Figure 2.3a) and highest for $NaClO_4$ at 2833.7 eV (Figure 2.3c), while that of $KClO_3$ occurs at 2830.5 eV (Figure 2.3b). Table 2.1 summarizes these results as well as all other numerical information presented in the Results Section.

The Cl K-edge X-ray absorption spectra of the monomeric Cl-Cu(II) complexes, D_{4h} $CuCl_4^{2-}$, D_{2d} $CuCl_4^{2-}$, square planar trans-$CuCl_2pdmp_2$ (pdmp = N-phenyl-3,5-dimethylpyrazole), and square pyramidal $CuCl_5^{3-}$ are shown in Figure 2.4. Each spectrum exhibits an intense, well-resolved pre-edge feature at lower energy than the edge. The pre-edge feature in the spectrum of D_{2d} $CuCl_4^{2-}$ (Figure 2.4b) appears at 2820.2 eV. This is at lower energy than in the others, which are 2820.6, 2820.5, and 2820.6 eV for D_{4h} $CuCl_4^{2-}$, $CuCl_2pdmp_2$ and $CuCl_5^{3-}$, respectively.

Figure 2.4 also shows the first derivative of each spectrum. In contrast to the spectra in Figure 2.3, the first derivatives shown in Figure 2.4 reflect structure on the rising edge: a broad maximum or two well-defined maxima in the region of the rising edge. The lower energy feature corresponds to the inflection point of the shoulder seen on the rising edge in each spectrum. The higher energy feature in the first derivative reflects the energy of the inflection point for the Cl 1s —> 4p main edge transition. The

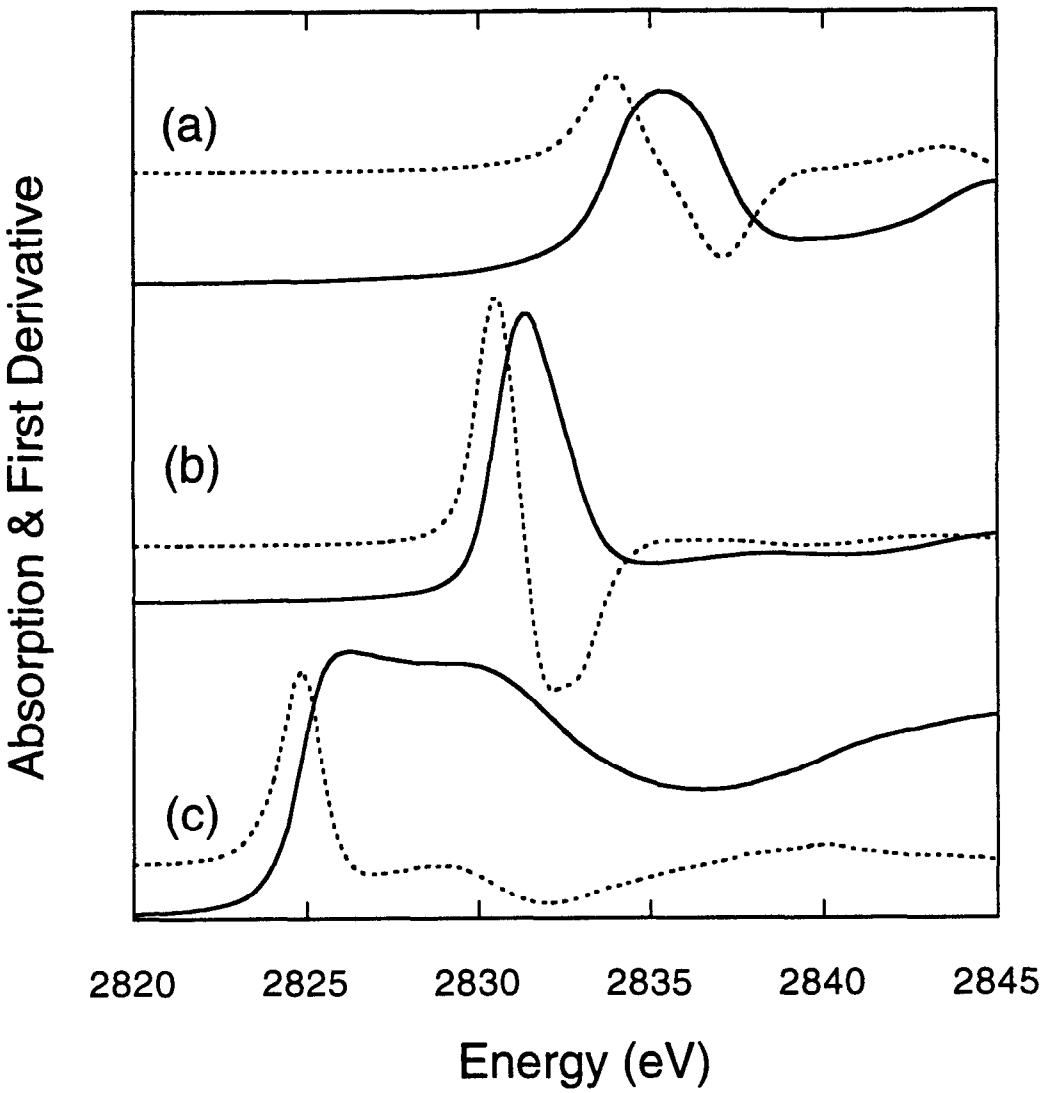

Figure 2.3. Cl K-edge spectra of (a) $NaClO_4$ (b) $KClO_3$ and (c) KCl. For each spectrum the solid line is the X-ray absorption data and the dashed line is the first derivative of the data. Spectral intensity are are rescaled due to a large variation in the y-scale of these spectra. The inflection point of the rising edge, determined by the energy of the maximum in the first derivative, ranges over almost 10 eV for this series of complexes. There are no pre-edge features observed in these data.

Table 2.1. Cl K-edge Transition Energies and Intensities and Spectral Analysis

Complex	Cl K-edge Spectral Features			Cl K-edge Spectral Analysis		
	Pre-edge energy (eV)[a]	Normalized pre-edge intensity[b]	Rising edge inflection point[c]	Calculated charge[d]	Re-normalized pre-edge intensity[e]	covalency per Cl (%)[f]
$NaClO_4$	-	-	2833.7	**1.91**		
$KClO_3$	-	-	2830.5	**1.49**		
KCl	-	-	2824.8	**-0.87**		
D_{4h} $CuCl_4^{2-}$	2820.6	0.75	2825.0	-0.65	0.76	9.8
D_{2d} $CuCl_4^{2-}$	2820.2	0.57	2825.3	-0.56	0.57	7.3
$CuCl_2$pdmp$_2$	2820.5	0.76	2825.3	-0.56	0.76	9.7
$CuCl_5^{3-}$	2820.6	0.57	2824.9	-0.69	0.72	9.2
$KCuCl_3$ (Cl^t)	2820.6 ±0.05	0.66±0.09	2824.9	-0.69	0.99±0.14	12.7±1.8
$KCuCl_3$ (Cl^b)	2821.3 ±0.09	0.35±0.09	(2825.6)[g]	-0.46	1.05±0.26	13.5±3.5
$(Ph_4P)CuCl_3$ (Cl^t)	2820.0	0.50	2825.3	-0.56	0.74	9.5
$(Ph_4P)CuCl_3$ (Cl^b)	2821.0	0.30	(2826.3)[g]	-0.23	0.92	11.7
$(Ph_4P)CuClBr_2$ (Cl^t)	2820.0					
$(Ph_4P)CuClBr_2$ (Cl^b)	2821.0					
Cu_2PAP	2820.7	0.53	2824.8	-0.72	0.80	10.2
Cu_2(L-O$^-$)Cl	2821.4	1.07	2825.8	-0.39	1.07	13.8

[a] Reported error is the standard deviation of the energy as determined from fitting of the spectra; the error is ≤ 0.009 eV unless otherwise noted.

[b] Reported error is the standard deviation of the area as determined from fitting of the spectra and the ~3% error from normalization of the data; the error is ≤ 0.04 unless otherwise noted.

[c] Error in the inflection point is < 0.1 eV; the inflection point reported is the highest energy feature in the first derivative in the rising edge region.

[d] Charge is generated from the relationship determined from Auger spectroscopy which established the charges of $KClO_4$, $KClO_3$, and KCl (the values in boldface type); see Figure 2.8.

[e] Areas are properly normalized to the total chloride which contributes to pre-edge intensity. The reported error is the standard deviation obtained from fits to the data and the ~3% error from normalization of data; error is ≤ 0.05 unless otherwise noted

[f] Error reported is the standard deviation of the reported covalency value. Error is ≤ 0.5% unless otherwise noted. Zero error in the 39% total covalency (9.75% per Cl) in D_{4h} $CuCl_4^{2-}$ used to quantitate the pre-edge intensity has been assumed.

[g] Inflection point for Cl^b estimated relative to that measured for the Cl^t of each complex, utilizing the observed pre-edge energy splitting (see text).

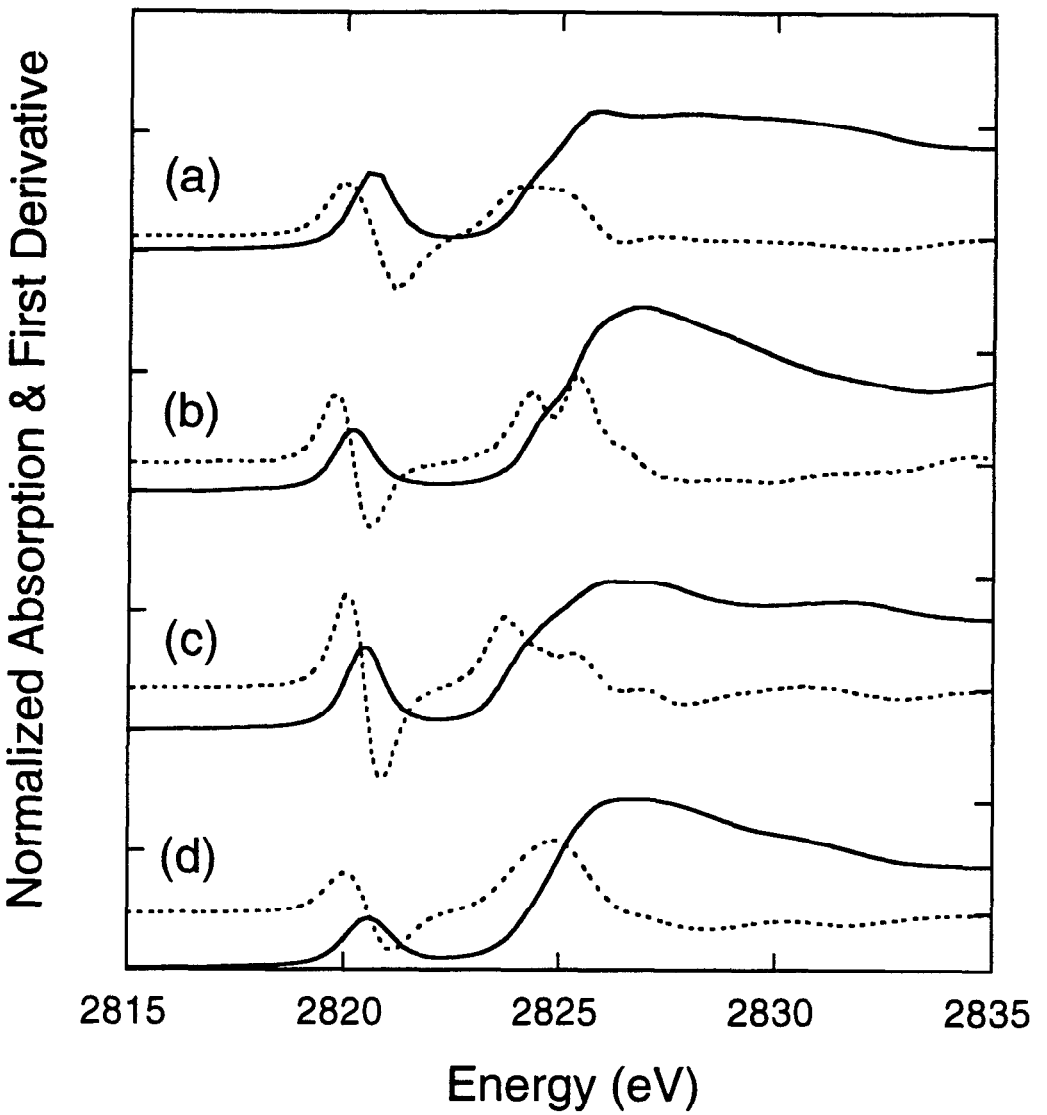

Figure 2.4. Cl K-edge spectra of the monomeric complexes (a) D_{4h} $CuCl_4^{2-}$ (b) D_{2d} $CuCl_4^{2-}$ (c) square planar trans $CuCl_2pdmp_2$ and (d) square pyramidal $CuCl_5^{3-}$. For each spectrum the solid line is the normalized X-ray absorption data and the dashed line is the first derivative of the data. Each spectrum exhibits a single pre-edge feature well separated from the rising edge. The energy of the feature in spectrum (b) is lower (2820.2 eV) than in (a), (c), and (d) for which the feature appears at 2820.6, 2820.5, and 2820.6 eV respectively.

inflection point of this Cl-based transition is used for comparison and occurs at 2825.0, 2825.3, 2825.3, and 2824.9 eV, for D_{4h} $CuCl_4^{2-}$, D_{2d} $CuCl_4^{2-}$, $CuCl_2pdmp_2$, and $CuCl_5^{3-}$, respectively.

Shown in Figure 2.5 are the Cl K-edge X-ray absorption spectra of the dimeric complexes $KCuCl_3$, $(Ph_4P)CuCl_3$, and $(Ph_4P)CuClBr_2$. The planar $Cu_2Cl_6^{2-}$ unit in $KCuCl_3$ has tetragonal symmetry at each copper,[16] including two additional Cl^- ligands at ~3.0 Å which belong to the equatorial plane of adjacent binuclear units (Figure 2.6a). The latter two complexes contain isolated $Cu_2Cl_6^{2-}$,[17] and $Cu_2Cl_2Br_4^{2-}$,[27] units for which the Cu symmetry is distorted T_d (Figure 2.6b). Studies of $(Ph_4P)CuClBr_2$ have shown[27] that the Cl has a preference for the bridging position in the dimer.

The Cl K-edge spectrum of each complex in Figure 2.5 exhibits a pre-edge feature. Compared to the monomers, the pre-edge width at half-height for $KCuCl_3$ (Figure 2.5a) is significantly larger and the feature is asymmetric. A fit of this spectrum (shown in Figure 2.5a, inset) reveals two transitions contained in the pre-edge feature envelope. In the spectrum of $(Ph_4P)CuCl_3$ (Figure 2.5b) the pre-edge is split into two distinct transitions. The pre-edge transition at lower energy is more intense than that at higher energy. The Cl K-edge spectrum of $(Ph_4P)CuClBr_2$ (Figure 2.5c) also exhibits a split pre-edge feature. The energies are identical to those found in $(Ph_4P)CuCl_3$, but in this spectrum the higher energy transition is more intense. Because some of the Cl^t are replaced with bromides in $CuClBr_2$, the reduction in relative intensity of the lower energy peak requires that it be Cl^t based and the higher energy peak is then assigned as originating from the Cl^b. The Cl^t (lower energy) transition has some residual intensity in $(Ph_4P)CuClBr_2$ because the complex contains some Cl^t.[27] By analogy, the two transitions in $KCuCl_3$ are assigned as the lower energy transition arising from the Cl^t and the higher energy transition arising from the Cl^b. The pre-edge transitions for the tetrahedrally distorted dimers (2820.0 and 2821.0 eV) are shifted to lower energy relative to those in $KCuCl_3$ (2820.6 and 2821.3 eV).

Figure 2.5 also shows the first derivative of each spectrum. Like for the monomers, the derivatives reflect structure on the rising edge. The inflection points of the main edge transitions for $KCuCl_3$ and $(Ph_4P)CuCl_3$ are at 2824.9 and 2825.3 eV, respectively.

Figure 2.7 shows the Cl K-edge X-ray absorption spectra for the mixed ligated dimers $[Cu_2(PAP6Me)(OH)Cl_3]\cdot H_2O$ (Cu_2PAP) and $[Cu_2(L\text{-}O^-)Cl][BPh_4]_2\cdot CH_3COCH_3$ ($Cu_2(L\text{-}O^-)Cl$). The Cu_2PAP dimer,[28] shown schematically in Figure 2.6c, contains square pyramidal five-coordinate coppers bridged by a hydroxyl oxygen in the equatorial plane, and by a chloride at a shared apical position with a large bond distance of > 2.6 Å.

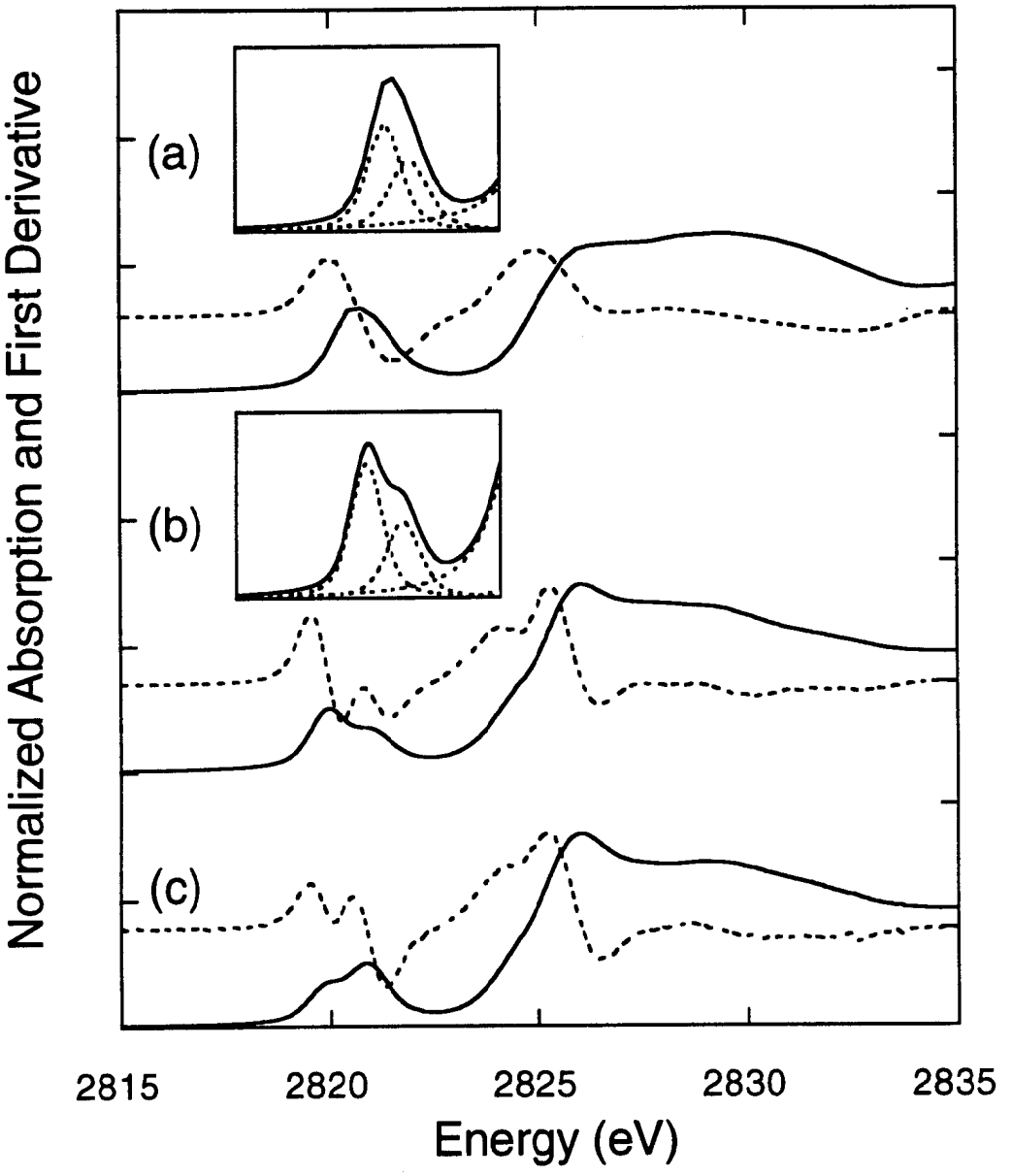

Figure 2.5. Cl K-edge spectra of dimeric complexes (a) planar $KCuCl_3$ (b) distorted tetrahedral $(Ph_4P)CuCl_3$ and (c) distorted tetrahedral $(Ph_4P)CuClBr_2$. For each spectrum the solid line is the normalized X-ray absorption data and the dashed line is the first derivative of the data. Spectrum (a) exhibits an asymmetric pre-edge feature; (b) and (c) exhibit a split pre-edge feature. Insets (a) and (b) show the fit to the pre-edge for $KCuCl_3$ and for $(Ph_4P)CuCl_3$, respectively.

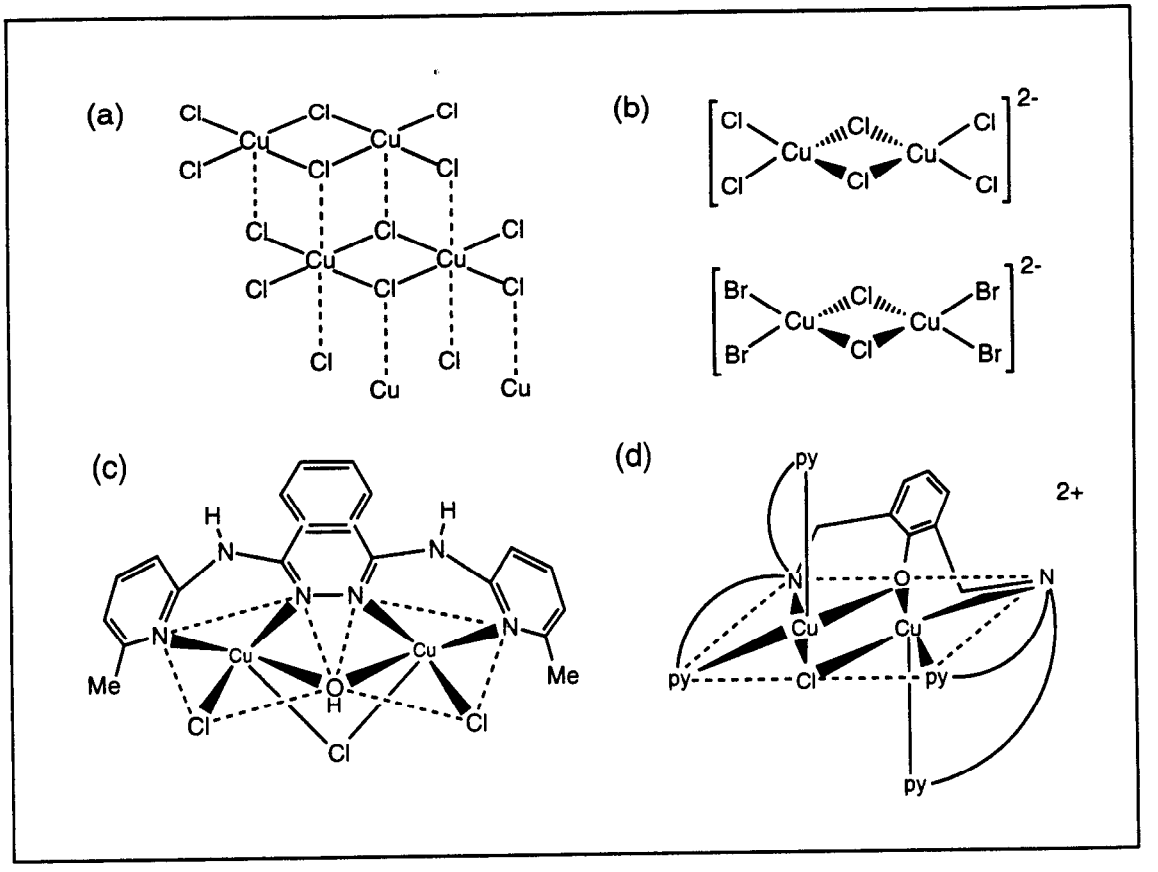

Figure 2.6. Schematic structures of Cl-Cu(II) dimeric complexes (a) $KCuCl_3$ (b) $(Ph_4P)CuCl_3$ and $(Ph_4P)CuClBr_2$ (c) Cu_2PAP and (d) $Cu_2(L\text{-}O^-)Cl$.

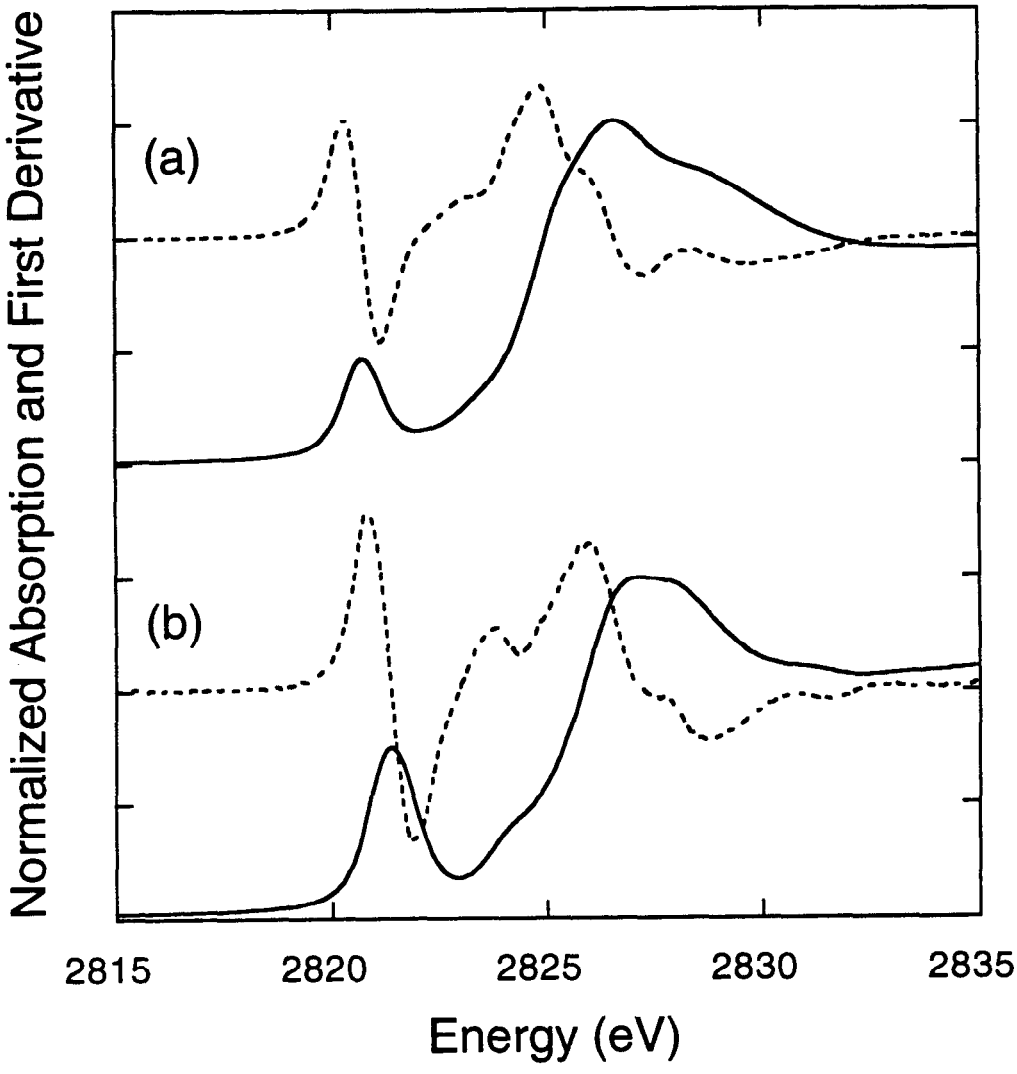

Figure 2.7. Cl K-edge spectra of dimeric complexes (a) Cu_2PAP and (b) $Cu_2(L\text{-}O^-)Cl$. For each spectrum the solid line is the normalized X-ray absorption data and the dashed line is the first derivative of the data. The pre-edge feature in (a) appears at 2820.7 eV while that in (b) appears 0.7 eV higher at 2821.4 eV. In addition, the rising edge inflection point is a higher energy for (b) and the pre-edge intensity is greater for spectrum (b).

Each copper is further coordinated by an equatorial terminal chloride, a pyridyl nitrogen and a phthalazine nitrogen in the equatorial plane. The $Cu_2(L\text{-}O^-)Cl$ dimer complex,[19] shown schematically in Figure 2.6d, contains square pyramidal five-coordinate coppers bridged by a phenolate oxygen and a chloride in the equatorial plane of the square pyramid. Each axial position is occupied by a pyridyl nitrogen, and the remaining equatorial positions for each copper are occupied by one pyridyl and one amine nitrogen. Each Cl K-edge spectrum (Figure 2.7) exhibits a pre-edge feature, which is at 2820.7 eV for Cu_2PAP and 2821.4 eV for $Cu_2(L\text{-}O^-)Cl$. The first derivatives of the spectra, shown in Figure 2.7, again reflect the rising edge structure in these systems. The main edge inflection points for these complexes are at 2824.8 and 2825.8 eV for Cu_2PAP and $Cu_2(L\text{-}O^-)Cl$, respectively.

2.4. Analysis of Results

2.4.1. Cl K-edges

As described in the Introduction (Section 2.1), the intense electric dipole allowed transition observed at the onset of the edge jump is a bound state Cl 1s —> 4p transition. The energy of this main edge transition is determined from the rising edge inflection point and shifts in this energy reflect shifts in the Cl 1s core in response to the relative charge on the atom. This correlation between charge and inflection point is clearly observed in the Cl K-edges of $NaClO_4$, $KClO_3$, and KCl (Figure 2.3). In $NaClO_4$, Cl has a formal charge of +7; in $KClO_3$ it has a formal charge of +5; and Cl in KCl is formally -1. The rising edge inflection points for these complexes at 2833.7, 2830.5, and 2824.8 eV for $NaClO_4$, $KClO_3$, and KCl, respectively, reflect these changes due to relative core shifts.

A more realistic charge on the Cl for these compounds has been experimentally estimated using Auger spectroscopy.[30] The charge on the Cl in KCl, $KClO_3$, and $KClO_4$ was determined to be -0.87, +1.49 and +1.91, respectively.[30] While the number of charges which have been experimentally determined are limited, previous studies[8-10] have demonstrated that the relationship between the X-ray edge position and a quantity called the "coordination charge"[29] is linear. Thus, using the charges from the Auger study and the experimental rising edge inflection points, a linear fit to the data in Figure 2.8 is obtained with $q = -916.66 + 0.32425\ eV^{-1}\ (x)$, where q is the charge on the

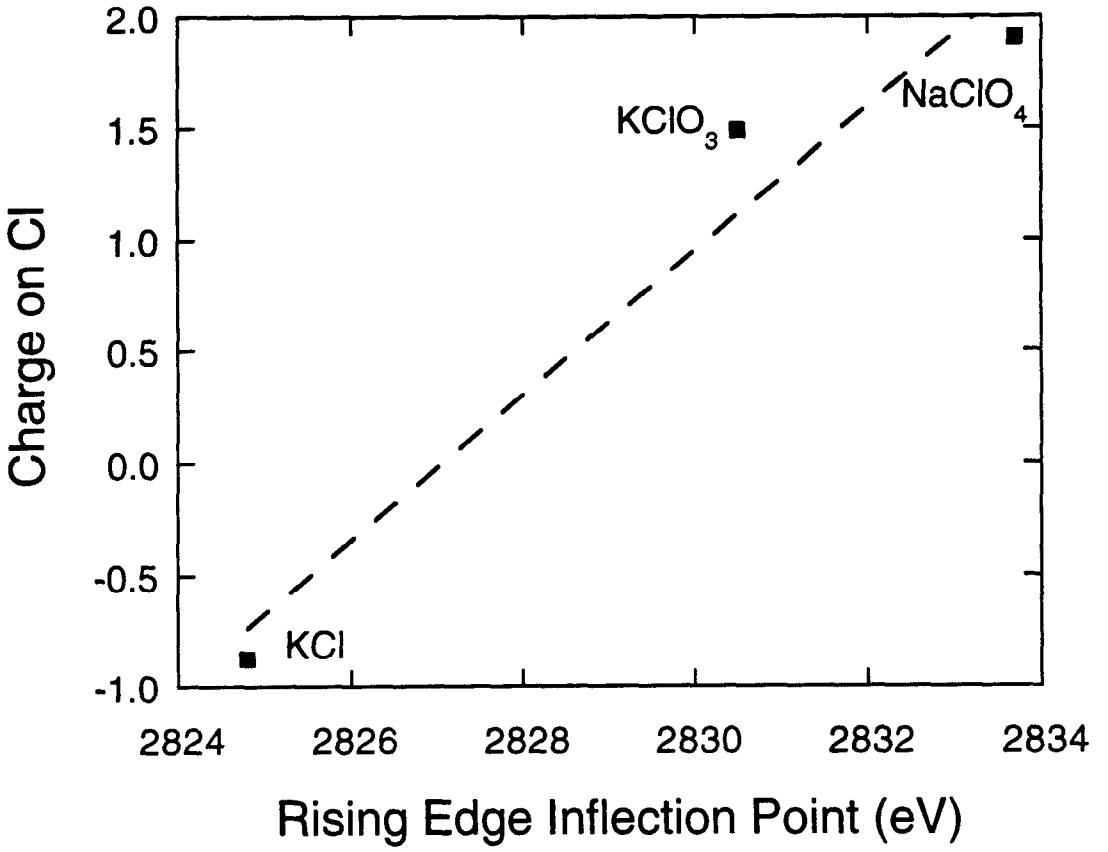

Figure 2.8. Inflection point of the rising edge of Cl K-edge data plotted *vs.* the charge on the Cl determined by Auger spectroscopy for the complexes $NaClO_4$, $KClO_3$, and KCl. The quantitative relationship between the rising edge energy and its total charge is determined by a linear fit to the data points, given by the equation $q = -916.66 + 0.32425\ eV^{-1}\ (x)$, where q is the charge on the Cl and x is the edge inflection point in eV.

Cl and x is the rising edge inflection point in eV. This equation can be applied to the Cl 1s —> 4p rising edge inflection point for each Cl-Cu(II) complex to obtain an estimate of the charge on the Cl. Table 2.1 shows the results from such an analysis for complexes with only one type of Cl. For D_{4h} $CuCl_4^{2-}$ the charge on each chloride is -0.65, while in D_{2d} $CuCl_4^{2-}$ and $CuCl_2$pdmp$_2$ it is -0.56. For the bridging chloride in Cu_2(L-O$^-$)Cl the charge is -0.39.

For complexes with more than one type of Cl, each may have a distinct core energy which can give rise to different rising edge inflection points. In $CuCl_5^{3-}$ and Cu_2PAP, the axial chlorides (Cl_{ax}) have a significantly weaker bonding interaction with the Cu and thus the equatorial chlorides (Cl_{eq}) have deeper core energies. Thus, the highest energy maximum in the first derivative reflects the 1s —> 4p transition for the Cl_{eq} in each case. Further, the stoichiometry of each site would indicate that the Cl_{eq} should dominate the rising edge region. Thus, the rising edge inflection point for these spectra can be used to calculate the charge on the Cl_{eq} in each case. In $CuCl_5^{3-}$ the Cl_{eq} charge is -0.69 and in Cu_2PAP it is -0.72. These results are presented in Table 2.1.

For the $Cu_2Cl_6^{2-}$ dimers, both the terminal (Cl^t) and bridging (Cl^b) chlorides have strong interactions with the coppers and the Cl 1s —> 4p transitions are unresolved. In order to determine which Cl gives rise to the main edge transition (and the corresponding inflection point) a comparison can be made to the Cu_2PAP and Cu_2(L-O$^-$)Cl dimers in which the rising edge inflection reflects only Cl^t and Cl^b, respectively. The rising edge inflection point occurs at (see Table 2.1) 2824.8 eV for the Cl^t in Cu_2PAP and at 2825.8 eV for the Cl^b in Cu_2(L-O$^-$)Cl. The main edge inflection in the planar $KCuCl_3$ dimer is at 2824.9 eV. This inflection point is thus assigned to the Cl 1s —> 4p transition for the Cl^t. From the stoichiometry of these dimers (2:1 Cl^t:Cl^b), the Cl^t would be expected to make a stronger contribution to the rising edge region. To obtain an estimate for the unresolved Cl^b 1s —> 4p transition in this spectrum, the magnitude of the pre-edge splitting can be used. While the difference in the Cl^t and Cl^b 1s —> 4p transitions is not necessarily the same as the 1s core energy difference (reflected in the pre-edge splitting), the pre-edge splitting of ~0.7 eV provides a useful approximation. Thus, the inflection point for the Cl^b would be expected at ~2825.6 eV (given in parentheses in Table 2.1), consistent with the inflection point for the Cl^b of Cu_2(L-O$^-$)Cl. The charges which correspond to these inflection points are -0.69 and -0.46 eV for the Cl^t and Cl^b, respectively (see Table 2.1). It should be noted that if the opposite assignment is made, such that the main edge inflection originates from the Cl^b, unreasonable values for the charges on each Cl are obtained.

By analogy, the main edge inflection point (at 2825.3 eV) in the tetrahedrally distorted $(Ph_4P)CuCl_3$ can be assigned as corresponding to the Cl^t. The unresolved Cl^b inflection point is estimated to be ~1 eV higher at 2826.3 eV (given in parentheses in Table 2.1). The charges calculated from these inflection points are -0.56 for the Cl^t and -0.23 for the Cl^b. Due to the uncertainty in obtaining the inflection for the Cl^b in these $Cu_2Cl_6^{2-}$ dimers (in addition to the uncertainty in the pre-edge splitting for $KCuCl_3$), the charge on each Cl^b is not rigorously determined.

For systems in which the charges on all ligands are quantitated by the above method, the charge on the central copper can be estimated. For D_{4h} $CuCl_4^{2-}$ each Cl carries a charge of -0.65 and the Cu carries a charge of +0.60. In D_{2d} $CuCl_4^{2-}$ each Cl carries a charge of -0.56 and the Cu carries a charge of +0.24. In the planar dimer $KCuCl_3$, the Cl^t's and Cl^b's carry charges of -0.69 and -0.46, respectively, and each Cu is characterized by a charge of +0.84. In the tetrahedrally distorted dimer $(Ph_4P)CuCl_3$ the Cl^t's and Cl^b's carry charges of -0.56 and -0.23, respectively, which results in a charge on Cu of +0.35. These results indicate that upon distortion from planarity, the total charge donation to the copper is increased. Further, while each Cl^b in a dimer donates more charge than the Cl^t, each copper in a dimer is more positive than in the analogous monomer because each bridging chloride must donate charge to two metal centers.

2.4.2. Pre-edge Peak Intensities

As described in Chapter 1 (Section 1.2.4), the intensity of the pre-edge feature in Cl K-edge spectra of Cl-Cu(II) systems provides a direct probe of the ligand contribution to the HOMO orbital due to bonding.[7] For symmetrically inequivalent chlorides, only those which contribute Cl 3p character to the HOMO orbital can reflect pre-edge intensity. Therefore, in order to accurately compare the pre-edge intensity for $CuCl_5^{3-}$ and Cu_2PAP to that of the other complexes, the pre-edge intensity must be re-normalized. The HOMO orbital is $d_{x^2-y^2}$ for both $CuCl_5^{3-}$,[31] and Cu_2PAP.[32] As the axial chloride of the square pyramid has no overlap with the $d_{x^2-y^2}$ orbital, it cannot contribute to the intensity of the pre-edge feature. Thus, in $CuCl_5^{3-}$, while all five chlorides contribute to the edge jump, only the four equatorial chlorides contribute to the pre-edge intensity. In Cu_2PAP, three chlorides contribute to the edge jump, but only the two equatorial Cl^t contribute to the pre-edge intensity. Further, for systems which have more than one pre-edge transition (e.g., both Cl^t and Cl^b transitions), each transition intensity must be re-normalized to the total of that type of Cl in the complex. The re-normalized pre-edge intensity for each complex are presented in Table 2.1.

The covalency of the Cl-Cu(II) interaction has been determined for D_{4h} $CuCl_4^{2-}$ by a variety of spectroscopic methods.[33] These give a HOMO orbital with 9.8% Cl 3p character donated by each of the four chlorides. Using this value as a calibration of the Cl K-edge pre-edge intensity, the covalency can be calculated from the experimental intensity for each complex using equation 1.3c. The Cl covalency in the HOMO orbital of these complexes ranges from 7.3% per chloride in D_{2d} $CuCl_4^{2-}$ to 13.8% for the Cl^b in $Cu_2(L\text{-}O^-)Cl$. These results are summarized in Table 2.1.

2.4.3. Pre-edge Peak Energies

In order to understand the trends exhibited in the energies of ligand pre-edge features, the separate contributions to the pre-edge energy (see Figure 2.2) from the Cl 1s core and the HOMO (both ligand field effects and d-manifold shifts) must be quantitated.

The contribution to the pre-edge energy from the Cl 1s core can be determined from the rising edge inflection point of Cl K-edge spectra. As described above, the energy position of the rising edge inflection point gives a measure of the relative Cl 1s core shift. The Cl 1s core energy for each complex relative to D_{4h} $CuCl_4^{2-}$ for four-coordinate complexes and relative to $CuCl_5^{3-}$ for five-coordinate complexes is summarized in Table 2.2. Because an increase in the coordination number would be expected to raise the overall d-manifold energy, this variable is eliminated if complexes with the same coordination number are compared (*vide infra*).

Energy shifts in the HOMO which are related to variations in ligand field geometry are taken into account by comparison of the optical d-d transition energies. For structural perturbations which change the geometry of the site only with respect to the ligands in the equatorial plane, changes in the energy of the $xy \longrightarrow x^2\text{-}y^2$ optical transition give the relative repulsion of the HOMO. In complexes for which the ligand field transitions have been assigned by polarized single-crystal absorption spectroscopy, comparison of the energies of the $xy \longrightarrow x^2\text{-}y^2$ transition can be made.

As the ligand field changes, all orbitals change energy. However, the center of the four fully occupied d-orbitals will experience a more limited variation.[34] Thus, a change in the energy center of the ligand field transitions primarily reflects shifts in the HOMO orbital. In cases for which optical assignments have not been made, the shift in the center of the d-d transitions provides a reasonable approximation to the shift in the HOMO orbital. This method introduces a larger uncertainty (~0.2 eV) than the use of assigned d-d transitions. Table 2.2 summarizes the shifts in the HOMO energy due to

Table 2.2. Cl K-edge Energy Analysis Parameters

Complex	Pre-edge energy (eV)[a]	Rising edge inflection point (eV)	Cl 1s core energy shift (eV)[b]	Ligand field $d_{xy} \rightarrow d_{x^2-y^2}$ transition (cm^{-1})	Center of ligand field transitions (cm^{-1})	Ligand field induced HOMO shift (eV)	Corrected pre-edge energy (eV)	d-manifold energy shift (eV)
			relative to D_{4h}			relative to D_{4h}		relative to D_{4h}
D_{4h} $CuCl_4^{2-}$	2820.6	2825.0	0	12500[e]	14445	0	2820.6	0
D_{2d} $CuCl_4^{2-}$	2820.2	2825.3	-0.3		7100[f]	-0.9[c]	2820.8±0.1	0.2±0.1
$CuCl_2$pdmp$_2$	2820.5	2825.3	-0.3		9950[g]	-0.6[d]	2820.8±0.3	0.2±0.3
$CuCl_5^{3-}$ (Cl_{eq})	2820.6	2824.9	+0.1	11000[h]		≥ -0.2[c]	2820.9±0.1	≥0.3±0.1
$KCuCl_3$ (Cl^t)	2820.6 ±0.05	2824.9	+0.1	11850[h]		-0.1[c]	2820.8±0.2	0.2±0.2
$KCuCl_3$ (Cl^b)	2821.3 ±0.09	(2825.6)	(-0.6)					
$(Ph_4P)CuCl_3$ (Cl^t)	2820.0	2825.3	-0.3		10565[i]	-0.5[d]	2820.2±0.3	-0.4±0.3
$(Ph_4P)CuCl_3$ (Cl^b)	2821.0	(2826.3)	(-1.3)					
			relative to $CuCl_5^{3-}$			relative to $CuCl_5^{3-}$		relative to $CuCl_5^{3-}$
$CuCl_5^{3-}$ (Cl_{eq})	2820.6	2824.9	0		11250[h]	0	2820.6	0
Cu_2PAP	2820.7	2824.8	+0.1	-	14800[j]	+0.4[d]	2820.4±0.3	-0.2±0.3
Cu_2(L-O$^-$)Cl	2821.4	2825.8	-0.9	-	14935[k]	+0.5[d]	2820.0±0.3	-0.6±0.3

[a] Error is less than 0.009 unless otherwise noted.

[b] Error for these energy differences is estimated to be ±0.1 eV

[c] Shifts are quantitated by differences in the $xy \rightarrow x^2-y^2$ transition energy.

[d] Shifts are quantitated by differences in the centers of the d-d optical transitions for which the uncertainty is ~0.2 eV.

[e] Hitchman, M. A. *J. Chem. Soc., Chem. Commun.* **1979**, 973-974.

[f] Ferguson, J. *J. Chem. Phys.* **1964**, *40*, 3406-3410.

[g] Ref 14.

[h] Ref 31.

[i] Willett, R. D.; Chow, C. *Acta Crystallogr.* **1974**, *B30*, 207-214.

[j] Ref 18.

[k] Ref 19.

ligand field effects relative to D_{4h} $CuCl_4^{2-}$ for four-coordinate complexes and relative to $CuCl_5^{3-}$ for five-coordinate complexes.

These relative energy shifts in the Cl 1s core and the HOMO can be used to obtain pre-edge energies which have been ligand field and core shift corrected. Shifts in the HOMO energy due to ligand field effects are subtracted from and the core 1s energy are added to the observed pre-edge transition energy (see Figure 2.2). These corrected pre-edge energies are given in Table 2.2. For cases in which these are the only contributions to the pre-edge energy, the corrected energy will be 2820.6 eV, the pre-edge energy for both D_{4h} $CuCl_4^{2-}$ and $CuCl_5^{3-}$, which have been used as the reference compounds for four- and five-coordinate complexes, respectively. Deviations from this value indicate that an additional effect, the overall energy of the d-manifold, must be taken into account. Table 2.2 (last column) gives the relative deviation in the corrected pre-edge energy (from 2820.6 eV), which is attributable to a d-manifold energy shift.

2.4.4. Correlations in Cl-Metal Bonding

Having defined the information content of Cl pre-edge energies and intensities, insight into bonding differences in related compounds may be obtained.

2.4.4.1. D_{4h} $CuCl_4^{2-}$ and D_{2d} $CuCl_4^{2-}$. Comparison of the Cl K-edge spectra for D_{4h} $CuCl_4^{2-}$ and D_{2d} $CuCl_4^{2-}$ (Figure 2.4) shows that the intensity of the D_{2d} complex is lower than that for D_{4h}. The intensity corresponds to a 9.8% covalent contribution to the HOMO per Cl in D_{4h} $CuCl_4^{2-}$, while the covalency of the D_{2d} $CuCl_4^{2-}$ HOMO is 7.3% per Cl (Table 2.1). As described previously, this is due to the differences in overlap between the Cl 3p orbitals and the Cu $d_{x^2-y^2}$ in the two geometries.[7,35] The D_{4h} Cu $d_{x^2-y^2}$ orbital lobes point directly at the Cl ligands, resulting in higher covalency.

The pre-edge transition energy is 0.4 eV lower for the D_{2d} complex relative to D_{4h} $CuCl_4^{2-}$. The energy analysis shows that this is a result of a ligand field induced HOMO shift to lower energy in D_{2d} by -0.9 eV in addition to a shift in the D_{2d} 1s core to deeper energy by -0.3 eV. A small energy effect of 0.2±0.1 eV, attributable to a shift to higher energy of the d-manifold of D_{2d} $CuCl_4^{2-}$, emerges from the analysis (Table 2.2). An overall shift up in the energy of the d-manifold is consistent with a slightly less positive Cu ion in the D_{2d} complex due to more total charge donation by its Cl ligands. The estimated charge on the copper in D_{4h} $CuCl_4^{2-}$ is +0.60 and in D_{2d} $CuCl_4^{2-}$ is +0.24.

This effect of charge donation is further supported by the Cl K-edge spectra which show that the rising edge inflection point is 0.3 eV higher in the D_{2d} complex (Table 2.1).

The relative energy of the rising edge inflection point indicates that the overall charge donation by the Cl in D_{2d} is greater, resulting in a Cl 1s core at deeper binding energy. This is also in agreement with results from a PES study[36] of these complexes which found that D_{2d} $CuCl_4^{2-}$ was characterized by ~3% more Cl covalency over the d-manifold than D_{4h} $CuCl_4^{2-}$. Thus, even though the HOMO orbital for the D_{4h} complex has a higher covalent contribution from Cl, the distortion from planarity in D_{2d} $CuCl_4^{2-}$, which results in slightly shorter bond lengths, allows a more favorable *overall* bonding interaction between the Cl and the copper.

2.4.4.2. D_{4h} $CuCl_4^{2-}$ and $CuCl_2pdmp_2$. The Cl K-edge spectrum of $CuCl_2pdmp_2$ (Figure 2.4) exhibits nearly the same pre-edge intensity as D_{4h} $CuCl_4^{2-}$. The intensity corresponds to 9.7% per Cl in $CuCl_2pdmp_2$ (compared to 9.8% in the D_{4h} complex) (Table 2.1). This indicates that, with respect to the Cu $d_{x^2-y^2}$ orbital, each Cl in $CuCl_2pdmp_2$ undergoes a very similar bonding interaction as in D_{4h} $CuCl_4^{2-}$.

The pre-edge transition energy is 0.1 eV lower in the $CuCl_2pdmp_2$ complex and the ligand field shifts the HOMO to lower energy by 0.6 eV. Combined with the core shift to higher energy by 0.3 eV, the energy analysis indicates that the d-manifold is shifted up in $CuCl_2pdmp_2$ by 0.2±0.3 eV (Table 2.2). The result is limited in this case primarily by the error associated with the measurement of the ligand field shift of the HOMO. Thus, within the resolution of the analysis there is little significant d-manifold shift in the $CuCl_2pdmp_2$ complex relative to D_{4h} $CuCl_4^{2-}$.

The rising edge inflection point is 0.3 eV higher in the $CuCl_2pdmp_2$ complex (Table 2.1), reflecting a core shift to deeper energy by 0.3 eV. This indicates that the overall charge donation by the Cl in $CuCl_2pdmp_2$ is larger than in D_{4h} $CuCl_4^{2-}$. Because two of the negatively charged Cl ligands have been replaced by neutral pyrazoles, each remaining Cl donates more electron density to the metal than in the tetrachloride complex.

2.4.4.3. D_{4h} $CuCl_4^{2-}$ and $CuCl_5^{3-}$. The re-normalized Cl K-edge pre-edge intensity in $CuCl_5^{3-}$ (Figure 2.4) is lower than in D_{4h} $CuCl_4^{2-}$. The $CuCl_5^{3-}$ intensity corresponds to 9.1% per Cl_{eq} in the HOMO (Table 2.1). In the square pyramidal geometry, the Cu is 0.3 Å above the plane of the four Cl_{eq}. Thus, the Cl_{eq} have less direct overlap with the Cu $d_{x^2-y^2}$ orbital than in the planar D_{4h} $CuCl_4^{2-}$. This change in the geometry slightly decreases the Cl_{eq} covalent contribution to the HOMO.

The observed pre-edge transition energy is the same in both complexes. The shift in the ligand field in $CuCl_5^{3-}$ relative to D_{4h} $CuCl_4^{2-}$ is determined from the energy of the optical xy —> x^2-y^2 transition, which indicates a shift down of the $CuCl_5^{3-}$ HOMO by at least 0.2 eV due to a decrease in the repulsive interaction of the x^2-y^2 orbital with the

equatorial ligands distorted out of the Cu xy plane. In this case the xy orbital may also experience less repulsion. Thus, the absolute shift in the x^2-y^2 orbital may be even larger than 0.2 eV. Combined with the core shift to higher energy by 0.1 eV, the energy analysis indicates that the overall d-manifold is shifted to higher energy in $CuCl_5^{3-}$ by at least 0.3 eV (Table 2.2). This d-manifold shift is due to the increase in coordination number which increases the repulsive, antibonding interaction experienced by the metal center.

The rising edge inflection point for the Cl_{eq} in $CuCl_5^{3-}$ is 0.1 eV lower than that observed in D_{4h} $CuCl_4^{2-}$, reflecting a core shift to higher energy by 0.1 eV in $CuCl_5^{3-}$. This indicates that the overall charge donation by the Cl_{eq} in $CuCl_5^{3-}$ is slightly less than in D_{4h} $CuCl_4^{2-}$. The equatorial bond lengths in these two complexes are nearly identical (2.250 Å[11] and 2.255 Å[15], for D_{4h} $CuCl_4^{2-}$ and $CuCl_5^{3-}$, respectively). However, the presence of additional Cl_{ax} results in each of the Cl_{eq} donating somewhat less charge than in the four-coordinate complex.

2.4.4.4. D_{4h} $CuCl_4^{2-}$ and $KCuCl_3$. The planar dimer $KCuCl_3$ exhibits two, unresolved pre-edge features (Figure 2.5). As described in the Results Section, the lower energy transition is assigned as originating from the Cl^t and the higher energy from the Cl^b. The re-normalized intensity of the Cl^b is somewhat larger than the Cl^t, corresponding to a covalency per Cl of 12.7±1.8% for the Cl^t and 13.5±3.5% for the Cl^b. The uncertainty in these measurements, which originates from the overlapping nature of the features, limits the quantitative comparison of these covalencies. Both chlorides in the dimer seem to be slightly more covalent with respect to the HOMO orbital than that observed in D_{4h} $CuCl_4^{2-}$.

The Cl^t and Cl^b pre-edge transition energies are separated by approximately 0.7 eV. Because these two transitions are from within the same molecule, the HOMO energy is fixed. Thus, this energy splitting provides a *direct* measure of the difference in the Cl 1s core energies. The splitting is a clear indication that each Cl^b, which is bound to two coppers, donates more negative charge than each Cl^t, which is bound to only one copper. This causes the Cl^b 1s core orbital to shift to deeper binding energy and results in a pre-edge transition at higher energy.

The Cl^t pre-edge transition energy in $KCuCl_3$ is the same as in D_{4h} $CuCl_4^{2-}$, while the Cl^b transition is ~0.7 eV higher. The shift in the HOMO due to shifts in the ligand field for $KCuCl_3$ relative to D_{4h} $CuCl_4^{2-}$ is calculated to be -0.1 eV from the xy —> x^2-y^2 transition. Combined with the core shift to higher energy by 0.1 eV for the Cl^b (relative to D_{4h} $CuCl_4^{2-}$), this indicates that the overall d-manifold is shifted to higher

energy in $KCuCl_3$ by 0.2±0.2 eV (Table 2.2). Thus, within the resolution of the analysis there is no net d-manifold shift in the dimer relative to the square planar monomer.

As described previously, the total charge on the Cu (+0.84) is more positive in the dimer than in the D_{4h} monomer (+0.60). Thus, while each Cl^b donates more total charge than a Cl^t, the total charge donation to the copper is less in the dimer than in the monomer. This change in charge would cause the copper orbitals to be shifted to lower energy in the dimer. However, due to the weak axial interactions in this complex the coordination number is increased from 4 to 6 (tetragonally elongated), increasing the repulsive interaction of the d-orbitals with the ligands. These two effects, which result in opposing d-manifold shifts, combine to give little net change in the d-manifold energy.

The rising edge inflection point reflects a core shift to lower binding energy by ~0.1 eV in the Cl^t of $KCuCl_3$ relative to the Cl in D_{4h} $CuCl_4^{2-}$. By comparison of the pre-edge transition splitting, the Cl^b core is estimated to be ~0.6 eV to lower energy than in D_{4h} $CuCl_4^{2-}$. This indicates that the overall charge donation by the Cl^t in $KCuCl_3$ is similar to the Cl in D_{4h} and the donation by the Cl^b is greater due to the interaction with two coppers.

2.4.4.5. D_{4h} $CuCl_4^{2-}$ and $(Ph_4P)CuCl_3$. The distorted tetrahedral dimer $(Ph_4P)CuCl_3$ also exhibits two resolved pre-edge features. As described in the Results Section, the lower energy transition originates from the Cl^t and the higher energy from the Cl^b. The re-normalized intensity of the Cl^b is larger than for the Cl^t, corresponding to a covalency per Cl of 9.5% for the Cl^t and 11.7% for the Cl^b (Table 2.1). These results clearly indicate that the Cl^b undergoes a more covalent interaction with respect to the HOMO due to its bonding to two coppers. The value of the Cl^t covalency is only slightly less than the 9.8% per Cl for D_{4h} $CuCl_4^{2-}$. While distortion toward T_d in the D_{2d} $CuCl_4^{2-}$ monomer reduced the Cl HOMO covalency, the distortion from planarity in this dimer complex is not as large. Further, the Cu-Cl^t bond length is significantly shorter in the $(Ph_4P)CuCl_3$ dimer than in D_{4h} $CuCl_4^{2-}$ (2.192 Å[17,37] *vs.* 2.250 Å[11], respectively) which will serve to increase the covalent interaction. This combination of factors results in only a small total reduction in covalency for the Cl^t relative to D_{4h} $CuCl_4^{2-}$.

The Cl^t and Cl^b pre-edge transition energies are separated by 1.0 eV. As in the planar dimer, this energy splitting provides a *direct* measure of the difference in the Cl 1s core energies. The splitting is a clear indication that the Cl^b donates more overall charge in the dimer through its interactions with two coppers.

The pre-edge transition energy is 0.6 eV lower for the Cl^t, and the transition from the Cl^b is 0.4 eV higher than in D_{4h} $CuCl_4^{2-}$. The shift in the ligand field in $(Ph_4P)CuCl_3$, as calculated from the centers of the optical d-d transitions, indicates a shift

down of the HOMO in $(Ph_4P)CuCl_3$ by 0.5 eV relative to D_{4h} $CuCl_4^{2-}$, which would be expected for the distortion away from planarity. Combined with the core shift to deeper energy by 0.3 eV for the Cl^t, this indicates that the overall d-manifold is shifted to lower energy in $(Ph_4P)CuCl_3$ by 0.4±0.3 eV (Table 2.2). This is consistent with a higher positive charge on the copper, which would result in a shift of all Cu orbitals to lower energy. However, the charge calculated above for the coppers in this dimer (+0.35) is less positive than the Cu (+0.60) in D_{4h} $CuCl_4^{2-}$. Because this calculated charge depends on an indirect estimate of the Cl^b core shift, the above d-manifold shift indicates that this approximation overestimates the total charge donated by the Cl^b in this complex.

The rising edge inflection point in $(Ph_4P)CuCl_3$ corresponding to the Cl^t appears 0.3 eV higher than the Cl in D_{4h} $CuCl_4^{2-}$ and reflects a core shift to deeper energy by 0.3 eV in the Cl^t. From the pre-edge transition splitting, then, the Cl^b core is shifted to ~1.3 eV to deeper energy than in D_{4h} $CuCl_4^{2-}$. This indicates that the overall charge donation by the Cl^t in $(Ph_4P)CuCl_3$ is slightly more than the Cl in D_{4h} and the donation by the Cl^b is significantly greater. The increased charge donation by the Cl^t is due to the change in geometry which, as in the D_{2d} monomer, favors an increase in the overall charge donation by the ligands. The shorter Cl^t-Cu(II) bond length also allows for a relative increase in the Cl^t charge donation. Relative to the Cl^t, the increase in charge donation by the Cl^b is again due to its interaction with two coppers.

2.4.4.6. Cu_2PAP and $Cu_2(L\text{-}O^-)Cl$. The Cu_2PAP and $Cu_2(L\text{-}O^-)Cl$ dimers contain square pyramidal coppers with N/O coordination. Each Cu in Cu_2PAP has one terminal Cl_{eq} which contributes to the pre-edge feature, while the two coppers in $Cu_2(L\text{-}O^-)Cl$ are bridged by a single equatorial chloride.

The re-normalized pre-edge intensity is significantly higher for $Cu_2(L\text{-}O^-)Cl$ than for Cu_2PAP (Figure 2.7). This corresponds to 13.7% covalent contribution per Cl in $Cu_2(L\text{-}O^-)Cl$ and a 10.1% covalent contribution per Cl in Cu_2PAP. The high covalency in $Cu_2(L\text{-}O^-)Cl$ is due to the bridging nature of the chloride bonding interaction.

The Cu_2PAP Cl_{eq} can be compared to the Cl_{eq} in $CuCl_5^{3-}$. The covalent contribution to the HOMO of each Cl_{eq} in Cu_2PAP is higher than in $CuCl_5^{3-}$ (9.1%), which is likely due to the significant distortion of the square pyramid in Cu_2PAP[28] resulting in a more favorable $d_{x^2-y^2}$ - Cl 3p interaction than in $CuCl_5^{3-}$.

In contrast to the monomeric $CuCl_2pdmp_2$, there is no indication that the chlorides in these dimers donate more total charge due to the substitution of N/O ligation at the copper sites. This is likely due to the variations in donating ability by these ligands which, due to the complexity of the ligands, can not be easily determined.

The pre-edge energy for Cu_2PAP is 0.7 eV lower than in $Cu_2(L\text{-}O^-)Cl$. As the energy analysis in Table 2.2 shows, the relative 1s core energies for the chlorides in these dimers are different by 1.0 eV, while the ligand field contributions to the HOMO energies are nearly the same. Thus, a small difference in the overall d-manifold is indicated which can likely be attributed to differences in bonding interactions with the non-chloride ligands.

The difference between the rising edge inflection points, 2824.8 and 2825.8 eV for the terminal Cl_{eq} of Cu_2PAP and the Cl^b of $Cu_2(L\text{-}O^-)Cl$, respectively, clearly illustrates the difference in charge donation by the terminal and bridging chloride. The Cl^b donates significantly more charge due to its interaction with two coppers which shifts the Cl^b 1s core to deeper energy.

2.5. Discussion

Ligand K-edge spectroscopy has been shown to be a powerful tool in the study of the electronic structure of metal-ligand interactions. The intensity of pre-edge features provides a direct probe of the covalent contribution of the ligand to the HOMO orbital. The energy of these pre-edge features can be corrected for ligand field effects and shifts in ligand core energy to reveal the relative energy of the d-manifold of the metal in the complex. Finally, the rising edge inflection point energy reflects the Cl 1s core energy and can be related to the relative charge donated by the ligand in the complex.

Results obtained from the application of this methodology to several systems are strongly supported by independent spectral data or by basic ligand field concepts. The d-manifold shift to less deep binding energy in D_{2d} vs. D_{4h} $CuCl_4^{2-}$ indicates the Cu in the D_{2d} complex is less positively charged. This result is supported by PES studies[36] which showed the D_{2d} complex to be more covalent over its orbitals than the D_{4h} complex. Further, this study indicates a shift up in the d-manifold energy for square pyramidal $CuCl_5^{3-}$ relative to D_{4h} $CuCl_4^{2-}$ when a fifth ligand is added to the coordination sphere. This is supported by basic ligand field concepts which give the average d-orbital energy to be proportional to $\sum_i \frac{Z_i e}{a}$, which is a sum over i ligands with a metal-ligand distance of a and charge Z_i.[38]

The application of energy and intensity models to a series of Cl-Cu(II) complexes has allowed the chemical basis for effects which contribute to pre-edge energies and intensities to be defined.

- In a geometric distortion from a square planar to a distorted tetrahedral structure, a decrease in the covalent Cl contribution to the HOMO and an increase in the

overall charge donation by Cl ligands are observed. The results show clearly that while the geometry can maximize the overlap and result in a high covalency in the HOMO, this is not necessarily reflective of the overall charge donation. However, because the half-occupied HOMO serves as the redox-active orbital in Cu(II) systems, the covalency of this orbital is crucial for understanding the catalytic properties of Cu in enzymatic systems.

• The bonding interaction with copper is very different for terminal *vs.* bridging chlorides. Due to the interaction with two copper ions, bridging chlorides donate more total charge than terminal chlorides. This difference in bonding is also reflected in a relatively larger covalent contribution to the HOMO for bridging chlorides.

• An increase in the coordination number or an increase in charge donation by the ligands (resulting in a less positively charged copper ion) has been shown to result in an increase in the overall energy of the d-manifold of the copper.

• The Cl-Cu(II) bonding is dependent on the nature of the other coordinating ligands. Replacing chlorides with less strongly donating pyrazoles causes the remaining chlorides to donate more total charge relative to the tetrachloride complex.

• Ligand pre-edge features, which contain contributions from both the Cl 1s core and the antibonding HOMO, are more complicated than features localized only on the ligand or metal. However, this study has shown that the different contributions can be separated to provide insight into the ligand-metal interactions of the site.

These studies, which demonstrate how ligand K-edge X-ray absorption features can be used to obtain information about ligand-metal bonding, form the basis for future ligand XAS studies. In particular, this methodology can be applied to study the differences in covalency of S(Cys)-Cu(II) bonding interactions and the relationship to electron transfer reactivity in blue copper sites. Further, the fact that ligand K-edge XAS can resolve features of bridging and terminal chlorides will be important for studies on iron-sulfur metalloproteins, in which the active site contains bridging inorganic sulfide as well as terminal cysteine sulfur ligands.

2.6. Acknowledgments

This research was supported by grants from NSF (CHE91-21576, K.O.H.), (CHE-9217628, E.I.S.) and NIH (RR 01209, K.O.H.). SSRL operations are funded by the Department of Energy, Office of Basic Energy Sciences. The Biotechnology Program is supported by the NIH, Biomedical Research Technology Program, National Center for Research Resources. Further support is provided by the Department of Energy, Office of

Health and Environmental Research. The authors also thank Prof. Kenneth Karlin for providing the precursor to Cu_2(L-O^-)Cl and Dr. William Estes for helpful discussions about the synthesis of $(Ph_4P)CuClBr_2$.

2.7. References and Notes

(1) Heald, S. M.; Tranquada, J. M. In *Physical Methods of Chemistry*; Rossiter, B. W.; Hamilton, J. F., Ed.; John Wiley & Sons: New York, 1990; Vol. 5; pp 189-272.

(2) Bianconi, A. In *X-ray Absorption: Principles, Applications, Techniques of EXAFS, SEXAFS, and XANES*; Koningsberger, D. C.; Prins, R., Ed.; John Wiley & Sons: New York, 1988; pp 573-662.

(3) Kau, L. S.; Spira-Solomon, D. J.; Penner-Hahn, J. E.; Hodgson, K. O.; Solomon, E. I. *J. Am. Chem. Soc.* **1987**, *109*, 6433-6442.

(4) Roe, A. L.; Schneider, D. J.; Mayer, R. J.; Pyrz, J. W.; Widom, J.; Que, L. *J. Am. Chem. Soc.* **1984**, *106*, 1676-1681.

(5) Eidsness, M. K.; Sullivan, R. J.; Scott, R. A. In *Bioinorganic Chemistry of Nickel*; Lancanster, J. R., Jr., Ed.; VCH: Deerfield Beach, FL, 1988; pp 73-92.

(6) Conradson, S. D.; Burgess, B. K.; Newton, W. E.; Hodgson, K. O.; McDonald, J. W.; Rubinson, J. F.; Gheller, S. F.; Mortenson, L. E.; Adams, M. W. W.; Mascharack, P. K.; Armstrong, W. A.; Holm, R. H. *J. Am. Chem. Soc.* **1985**, *107*, 7935-7940.

(7) Hedman, B.; Hodgson, K. O.; Solomon, E. I. *J. Am. Chem. Soc.* **1990**, *112*, 1643-1645.

(8) Ovsyannikova, I. A.; Batsanov, S. S.; Nasanova, L. I.; Batsanova, L. R.; Nekrasova, E. A. *Bull. Acad. Sci. USSR Phys. Ser. (Engl. Transl.)* **1967**, *31*, 936-940.

(9) Cramer, S. P.; Eccles, T. K.; Kutzler, F. W.; Hodgson, K. O.; Mortenson, L. E. *J. Am. Chem. Soc.* **1976**, *98*, 1287-1288.

(10) Kirby, J. A.; Goodin, D. B.; Wydrzynski, T.; Robertson, A. S.; Klein, M. P. *J. Am. Chem. Soc.* **1981**, *103*, 5537-5542.

(11) Udupa, M. R.; Krebs, B. *Inorg. Chim. Acta* **1979**, *33*, 241-244.

(12) Sharnoff, M. *J. Chem. Phys.* **1965**, *42*, 3383-3395.

(13) McGinnety, J. A. *J. Am. Chem. Soc.* **1972**, *94*, 8406-8413.

(14) Francisco, R. H. P.; Lechat, J. R.; Massabni, A. C.; Melios, C. B.; Molina, M. *J. Coord. Chem.* **1980**, *10*, 149-153.

(15) Antolini, L.; Marcotrigiano, G.; Menabue, L.; Pellacani, G. C. *J. Am. Chem. Soc.* **1980**, *102*, 1303-1309.

(16) Willett, R. D.; Dwiggins, C., Jr.; Kruh, R. F.; Rundle, R. E. *J. Chem. Phys.* **1963**, *38*, 2429-2436.

(17) Textor, M.; Dubler, E.; Oswald, H. R. *Inorg. Chem.* **1974**, *13*, 1361-1365.

(18) Bautista, D. V.; Dewan, J. C.; Thompson, L. K. *Can. J. Chem.* **1982**, *60*, 2583-2593.

(19) Karlin, K. D.; Farooq, A.; Hayes, J. C.; Cohen, B. I.; Rowe, T. M.; Sinn, E.; Zubieta, J. *Inorg. Chem.* **1987**, *26*, 1271-1280.

(20) Hedman, B.; Frank, P.; Gheller, S. F.; Roe, A. L.; Newton, W. E.; Hodgson, K. O. *J. Am. Chem. Soc.* **1988**, *110*, 3798-3805.

(21) Lytle, F. W.; Greegor, R. B.; Sandstrom, D. R.; Marques, E. C.; Wong, J.; Spiro, C. L.; Huffman, G. P.; Huggins, F. E. *Nucl. Instr. Meth.* **1984**, *226*, 542-548.

(22) Stern, E. A.; Heald, S. M. *Rev. Sci. Instrum.* **1979**, *50*, 1579-1582.

(23) Argonne National Laboratory; B. S. Garbow, K. E. Hillstrom, J. J. More.

(24) Agarwal, B. K. *X-ray Spectroscopy*; Springer-Verlag: Berlin, 1979, pp 276ff.

(25) Tyson, T. A.; Roe, A. L.; Frank, P.; Hodgson, K. O.; Hedman, B. *Phys. Rev. B* **1989**, *39A*, 6305-6315.

(26) Lytle, F. W. In *Applications of Synchrotron Radiation*; Winick, H.; Xian, D.; Ye, M. H.; Huang, T., Ed.; Gordon & Breach: New York, 1989; pp 135.

(27) Estes, W. E.; Wasson, J. R.; Hall, J. W.; Hatfield, W. E. *Inorg. Chem.* **1978**, *17*, 3657-3664.

(28) Mandal, S. K.; Thompson, L. K.; Hanson, A. W. *J. Chem. Soc., Chem. Commun.* **1985**, 1709-1711.

(29) The "coordination charge" is given by $\eta = Z - \Sigma_k n_k c_k$ where η is the coordination charge, Z is the formal oxidation state of the absorber, and c_k is the degree of covalence for the *k*th ligand and n_k is the total number of ligands. Previous studies have used differences in electronegativities to calculate the c_k values (see refs. 8-10).

(30) Nefedov, V. I.; Yarzhemsky, V. G.; Chuvaev, A. V.; Trishkina, E. M. *J. Electron Spectros. Relat. Phenom.* **1988**, *46*, 381-404.

(31) Desjardins, S. R.; Wilcox, D. E.; Musselman, R. L.; Solomon, E. I. *Inorg. Chem.* **1987**, *26*, 288-300.

(32) Mandal, S. K.; Woon, T. C.; Thompson, L. K.; Newlands, M. J.; Gabe, E. J. *Aust. J. Chem.* **1986**, *39*, 1007-1021.

(33) Solomon, E. I. *Comments Inorg. Chem.* **1984**, *3*, 227-320.

(34) Solomon, E. I.; Hare, J. W.; Dooley, D. M.; Dawson, J. H.; Stevens, P. J.; Gray, H. B. *J. Am. Chem. Soc.* **1980**, *102*, 168-178.

(35) Shadle, S. E.; Penner-Hahn, J. E.; Schugar, H. J.; Hedman, B.; Hodgson, K. O.; Solomon, E. I. *J. Am. Chem. Soc.* **1993**, *115*, 767-776.

(36) Didziulis, S. V.; Cohen, S. L.; Gewirth, A. A.; Solomon, E. I. *J. Am. Chem. Soc.* **1988**, *110*, 250-268.

(37) Willett, R. D.; Chow, C. *Acta Crystallogr.* **1974**, *B30*, 207-214.

(38) Figgis, B. N. *Introduction to Ligand Fields*; John Wiley & Sons, Inc.: New York, 1966, pp 31.

Chapter 3

X-ray Absorption Studies of the Blue Copper Site: Metal and Ligand K-Edge Studies to Probe the Origin of the EPR Hyperfine Splitting in Plastocyanin

3.1. Introduction

The oxidized blue copper protein active site is characterized by unique spectral features compared to those of normal, tetragonal Cu(II) complexes.[1-3] The development of a detailed understanding of these features has been the goal of many experimental and theoretical studies. The intense blue color of the oxidized blue copper proteins results from an optical absorption at ~600 nm. The extinction coefficient of this feature is two orders of magnitude greater than that for absorption bands in the same region in normal tetragonal copper(II) complexes. Polarized absorption and low temperature magnetic circular dichroism (MCD) studies in combination with self-consistent-field-Xα-scattered-wave (Xα) calculations have definitively assigned this feature as a S(Cys) $3p\pi$ —> Cu $3d_{x^2-y^2}$ charge transfer (CT) transition.[4,5]

The EPR spectra of oxidized blue copper centers exhibit $g_{\|} > g_{\perp} > 2.00$, indicating that the half-occupied ground state orbital is $3d_{x^2-y^2}$. The same ground state is found in normal, tetragonal copper(II) complexes. However, the EPR spectra of blue copper centers exhibit unusually small parallel hyperfine splitting, the magnitude of which (60×10^{-4} cm^{-1}) is about one-third that of normal copper hyperfine splitting. The half-occupied 3d-orbital associated with this EPR signal is involved in the electron transfer reactivity of the blue copper center. Thus, to gain insight into the function of these proteins, it is essential to have a clear understanding of the electronic structural origin of the small $A_{\|}$ splitting associated with this ground state wavefunction.

Distorted tetrahedral (D_{2d}) $CuCl_4^{2-}$ exhibits small EPR parallel hyperfine splitting similar to that exhibited by blue copper centers (on the order of $< 70 \times 10^{-4}$ cm^{-1}). One explanation for the reduced $A_{\|}$ splitting in distorted tetrahedral copper(II) complexes requires $4p_z$ mixing into the $3d_{x^2-y^2}$ ground state wave function.[6] This mixing would reduce the hyperfine coupling because the $4p_z$ orbital has a spin dipolar contribution which opposes that of the $3d_{x^2-y^2}$ orbital, thus reducing the coupling between the unpaired electron spin and the copper nuclear spin. Sharnoff has calculated that for distorted tetrahedral (D_{2d}) $CuCl_4^{2-}$, 12% Cu $4p_z$ orbital-character mixed into the half-occupied Cu 3d orbital would lower the hyperfine splitting value to the experimentally observed value.[7] Because spectroscopy[8] and subsequent crystal structures[9,10] of blue copper proteins have led to a description of the active site geometry as distorted tetrahedral, the reduced $A_{\|}$ splitting in the EPR of blue copper has also been explained by a $4p_z$ mixing mechanism.[11]

Single crystal EPR studies of plastocyanin (Pc), the most well characterized of the blue copper proteins, have shown that the unique axis ($g_{\|}$) is nearly aligned with the long Cu-thioether bond (Figure 3.1).[12] A ligand field analysis of the EPR data and of the near-

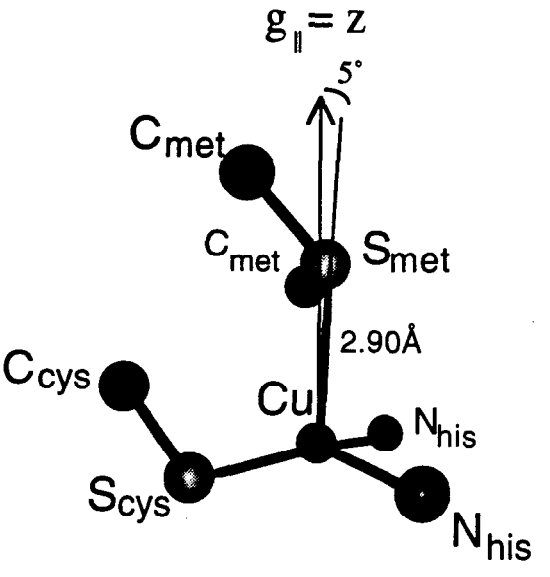

Figure 3.1. Active site structure of the oxidized form of the blue copper protein plastocyanin. The copper is ligated in an effective C_{3v} geometry by one cysteine, two histidines and one methionine, which lies ~5° off the $g_{\|}$ direction.

IR ligand field transitions determined that the site is best described as having elongated C_{3v} site symmetry with rhombic distortions.[12] In C_{3v} symmetry, group theory allows the $3d_{x^2-y^2}$ orbital to mix with $4p_{x,y}$, which would increase, not decrease, the $A_{||}$ hyperfine splitting.

Xα calculations have previously been performed on several copper(II) centers. In D_{4h} $CuCl_4^{2-}$, which exhibits normal EPR hyperfine splitting, the ground state wavefunction contains no 4p mixing due to inversion symmetry.[13] Calculations on the distorted tetrahedral (D_{2d}) $CuCl_4^{2-}$ complex indicate only ~4% $4p_z$ mixing into the ground state $3d_{x^2-y^2}$ orbital.[13] Similar calculations on the Pc site indicate that the protein site ground state wavefunction contains only ~1% 4p mixing involving the $p_{x,y}$ orbitals,[4,5] which is consistent with the C_{3v} effective site symmetry described by the ligand field analysis. These results clearly question the possibility that 12% $4p_z$ mixing accounts for the small hyperfine in either the D_{2d} complex or the blue copper site.

An alternative explanation for the small $A_{||}$ hyperfine coupling constant of blue copper sites is unusually high covalency in the Cu-thiolate bond.[4,5] Xα calculations indicate that the ground state wavefunction is highly covalent, consisting of 42% Cu $3d_{x^2-y^2}$ and 36% S(Cys) 3p.[4,5] A high degree of covalency delocalizes the unpaired electron spin from the copper onto the cysteine ligand thereby reducing the coupling to the copper nuclear spin. Interestingly, Xα calculations do not indicate that the ground state wave function of D_{2d} $CuCl_4^{2-}$ is unusually covalent.[13]

Experimental studies of the magnitude and nature of Cu 4p mixing into the $3d_{x^2-y^2}$ ground state and of the covalency of these sites are necessary to determine the origin of the small hyperfine splitting in both the D_{2d} $CuCl_4^{2-}$ and the blue copper centers. The results will provide important insight into the blue copper site, in particular into the electronic structure and copper-thiolate interaction of the ground state wavefunction.

To evaluate $4p_z$ mixing, Cu K-edge X-ray absorption spectral (XAS) studies on $CuCl_4^{2-}$ complexes and the blue copper protein Pc have been undertaken. Previous K-edge studies of Cu(II) systems have observed a weak transition at ~8979 eV and a shoulder or partially resolved peak on the rising edge at ~8987 eV.[14,15] The peak at ~8979 eV is assigned as a 1s —> 3d transition. In appropriate orientations, this transition has electric quadrupole-allowed intensity.[16] Further, as a formally forbidden electric dipole transition, it gains electric dipole intensity from 4p mixing into the half-occupied 3d-orbital in appropriate site symmetries. As the electric dipole intensity of the 1s —> 3d transition reflects the magnitude of 4p mixing into the half-occupied 3d orbital, these spectra serve as a probe of 4p mixing into the ground state orbital. Polarized XAS studies of oriented single crystals provide a method for selecting and resolving the orientation-dependence of

near-edge features.[16-25] The high intensity and plane-polarization of synchrotron radiation is ideal for these studies. Analysis of the polarized intensity of the 1s —> 3d (~8979 eV) transition allows for the determination of which Cu 4p-orbital(s) contribute electric dipole intensity to the transition. Herein, a protocol for quantitating this 4p mixing is developed, which includes an analysis of the ~8987 eV feature.

As an experimental probe of the covalency of these sites, XAS K-edge studies have been conducted at the Cl and S K-edges. As described in Chapter 1 (section 1.2.4) and demonstrated in Chapter 2, ligand K-edge XAS can be used as a quantitative probe of covalency in open-shell metal complexes.[26] This technique is particularly useful for sulfur ligands since naturally occurring isotopes of sulfur do not have a nuclear spin; thus experiments involving ligand superhyperfine are not accessible. We have measured the S K-edge X-ray absorption spectra of the model compound, [Cu(tet *b*)(*o*-$SC_6H_4CO_2$)]·H_2O (Cu-tet *b*) and of the oxidized blue copper protein, Pc. Cu-tet *b* is ligated by a thiolate sulfur at 2.36 Å from the copper and four nitrogen ligands in a distorted 5-coordinate geometry. This complex has a $3d_{x^2-y^2}$ ground state[27] and exhibits normal EPR hyperfine splitting[28] and so provides a good contrast to the blue copper system. These studies at the S K-edge allow the degree of covalency between the copper and the cysteine sulfur in blue copper proteins to be determined. In order to quantitate the pre-edge intensity SCF-Xα-SW calculations on the Cu-tet *b* complex have been performed. Xα calculations provide insight into the electronic structure and bonding of the system, in particular into the covalent character of the ground state wavefunction.

3.2 Experimental

3.2.1. Sample Preparation

(Creatininium)$_2CuCl_4$[29] and Cs_2CuCl_4[7,30] were prepared according to published methods. Other details of the crystal preparation are as previously described in references 16 and 31-32, respectively. The sample of [Cu(tet *b*)(*o*-$SC_6H_4CO_2$)]·H_2O was synthesized as described in the literature.[27] $Na_2S_2O_3 \cdot 5H_2O$ was purchased from J.T. Baker and used without further purification.

The purification and crystallization of poplar Pc (*Populus nigra var italica*) used in the polarized Cu K-edge experiments has been described previously in the publication where these spectra were initially reported.[17] Spectra shown in Figure 3.8 are data collected on crystal #7.[33] Pc used in the non-polarized Cu K-edge experiments and in the

S K-edge experiments was isolated from spinach chloroplasts according to published methods.[34]

For the Cu K-edge powder spectra, the metal complexes were ground into a fine powder and diluted in boron nitride. This mixture was then packed into an aluminum spacer sample holder and sealed with mylar tape. For the ligand K-edge experiments, solid samples were ground into a fine powder which was thinly dispersed on mylar tape (containing an acrylic adhesive determined to be free of chlorine and sulfur contaminants). The tape was mounted across the window of an aluminum plate.

Pc S K-edge protein measurements were made at room temperature. The protein solution (in 50 mM phosphate buffer, pH = 7.0) was pre-equilibrated in a buffer-saturated He atmosphere for ~1 hour to minimize bubble formation in the sample cell. The protein solution was loaded via syringe into a 1-2 mm teflon cell sealed in back by a layer of mylar tape and in front by a thin 6.4 μm polypropylene window. UV/Vis spectroscopy was used to verify the integrity of the sample both before and after exposure to the X-ray beam.

3.2.2. Crystal Alignment

(Creatininium)$_2$CuCl$_4$[29], Cs$_2$CuCl$_4$[30], and poplar Pc[9] have been structurally characterized by X-ray diffraction. The molecular site symmetry of (creatininium)$_2$CuCl$_4$ is approximately D_{4h}. The site symmetry of Cs$_2$CuCl$_4$ will be discussed later in this section. The published atomic coordinates were used to determine the orientation of specific molecular directions relative to the crystal axes. Integer hkl values corresponding to a set of lattice planes perpendicular to the chosen molecular directions were then calculated with use of the known unit cell parameters. The alignment procedure finds the ϕ and χ values which place the desired molecular orientation perpendicular to the incoming radiation and in the horizontal plane. Since synchrotron radiation is highly polarized in the horizontal plane, the alignment provides for orientation of the molecular vector of interest to be parallel to the electric vector (**E**) of the incoming radiation. Specific crystal alignment and crystal positioning procedures for (creatininium)$_2$CuCl$_4$[16], Cs$_2$CuCl$_4$[31,32], and poplar Pc[17] are described in earlier publications of these spectra.

3.2.3. X-ray Absorption Measurements & Data Acquisition

All data were collected at the Stanford Synchrotron Radiation Laboratory under dedicated operation (3.0 GeV, ~50 mA) with the SPEAR storage ring.

3.2.3.1. Cu K-edges. (Creatininium)$_2$CuCl$_4$ and Pc polarized Cu K-edge data were collected on beam line 2-2; experimental details are described in references 16 and 17, respectively. Cs_2CuCl_4 polarized Cu K-edge data were collected in fluorescence mode on beam line 4-2; experimental details are described elsewhere.[31,32] Non-polarized data of (creatininium)$_2$CuCl$_4$ and Cs_2CuCl_4 were measured in transmission mode at room temperature on beam line 2-2. Pc solution data were collected in fluorescence mode at 35 K using a Ge 13-element array detector on beam line 7-3.

A Si(220) double-crystal monochromator was utilized for energy selection for all Cu K-edge measurements. The monochromator was detuned 50% to minimize higher harmonic components in the X-ray beam. Data for the above samples were measured from ~8970 to ~9300 eV, with a step size of ~0.2 eV in the edge region (8970-9050 eV). For the Cu K-edge experiments, a third ion chamber was used for internal calibration by the simultaneous measurement of the absorption of a Cu foil placed between the second and third ion chambers. The first inflection point of the Cu foil edge spectrum was assigned to 8980.3 eV.

3.2.3.2. S K-edges. Sulfur K-edge data were measured using the 54-pole wiggler beam line 6-2 in low magnetic field mode (5 kG) with a Pt-coated focusing mirror and a Si(111) double-crystal monochromator. The monochromator was detuned ~30% to minimize higher harmonic components in the X-ray beam. Details of the optimization of this beamline for low energy studies and the experimental setup have been described in Chapter 1 (Section 1.2.5) as well as in an earlier publication.[35]

The data were collected as fluorescence excitation spectra.[35] The energy was calibrated from the S K-edge spectra of $Na_2S_2O_3 \cdot 5H_2O$, run at intervals between the sample scans. The maximum of the first pre-edge feature in this spectrum was assigned to 2472.02 eV. Data were collected from 2420 to 2740 eV, with a step size of 0.08 eV in the edge region. The spectrometer resolution was ~0.5 eV.[35] A reproducibility in edge position determination of ~0.1 eV for these experiments was obtained by calculating and comparing first and second derivatives for model compounds measured during different experimental sessions.

3.2.4. Data Analysis

A smooth pre-edge background was removed from all spectra by fitting a polynomial to the pre-edge region and subtracting this polynomial from the entire spectrum. Normalization of the data was accomplished by fitting a flat polynomial or straight line to

the post-edge region and normalizing the edge jump to 1.0 at 9000 eV for the copper edges and at 2490 eV for the sulfur edges.

3.2.4.1. Analysis of polarized data. Description of the crystallographic systems in (creatininium)$_2$CuCl$_4$[16] and poplar Pc[17] and their application to data analysis are described in earlier publications. Cs_2CuCl_4 crystallizes in the orthorhombic space group Pnam. There are four molecules per unit cell, which form two pairs related by glide planes. Although the symmetry of the molecule is only C_s from crystallographic symmetry, the anion has approximate D_{2d} symmetry. The molecular axes are defined such that the *z*-axis is perpendicular to the plane which the $CuCl_4^{2-}$ anion would occupy if it were flattened to D_{4h} symmetry. The molecular *x* and *y* axes are defined along the projections of the Cu-Cl bonds in the hypothetical flattened plane.[36] One of the *x,y* axes (arbitrarily chosen as *y*) is aligned parallel to the crystallographic *c*-axis. Due to the space group symmetry, the two distinct molecular *x*-axes (and the molecular *z*-axes) are separated by 75°. The observed transition strengths along each crystallographic axis, I_a, I_b, I_c are then:

$$I_a = 0.63\ I_x + 0.37\ I_z$$
$$I_b = 0.37\ I_x + 0.63\ I_z$$
$$I_c = I_y$$

where I_x, I_y, and I_z are the molecular absorption cross sections. Data were measured along each crystallographic axis and from these data it is possible to determine the isolated molecular transition strengths.

3.2.5. Fitting Procedures

Data were fit with the non-linear least squares fitting program FITCUR. FITCUR was written by Dr. Geoffrey S. Waldo, now at North Carolina State University, then in the laboratory of Prof. James E. Penner-Hahn. The program was modified at Stanford University by Dr. Soichi Wakatsuki to include the option of imposing separate optimization weightings for the fit to the data, the first derivative, and/or the second derivative of the data. In the fitting experiments described herein, the weighting scheme used for the fits was: data, 0.70 : first derivative, 0.0 : second derivative, 0.30. Pre-edge features were modeled by Lorentzian or Gaussian functions. Neither function by itself is completely adequate for fitting the pre-edge features, as the features are expected to be a convolution of the Lorentzian transition envelope[37] and the Gaussian imposed by the spectrometer

optics.[37-40] Functions were chosen which were found empirically to give the best fit. The rising edge was modeled by either an arctangent function or the tail of a Lorentzian function. For spectra consisting of a pre-edge feature and a smooth rising edge, one function for the rising edge and one function for the pre-edge feature were all that was necessary, and a best fit minimum was found fairly easily.

For edges with a complicated line shape, such as the *z*-polarized Cu K-edge spectrum of Cs_2CuCl_4, the following approach was taken. The number and energy position of the functions used were chosen based on the features evident in the second derivative of the spectrum. Functions for fitting were chosen based on the criteria that the features of both the data and of the second derivative should be reproduced. It was found that for this fit, the feature at ~8987 eV was best modeled using a combination of Lorenztian and Gaussian contributions. All parameters (maximum height, full-width-at-half-maximum (FWHM), and energy position) of each feature were allowed to vary, with the exception of those parameters which varied to unreasonable values (e.g., a FWHM which varied to over 4.8 eV). These parameters' values were fixed for each fit and systematically stepped through a series of reasonable values. Fits were examined carefully and the best value for the parameter, based on the above criteria, was chosen. In some cases, the goodness-of-fit was invariant to the value of the fixed parameter and a series of equivalently good fits resulted. The standard deviation of the fit (as calculated by FITCUR) was the same for a series of equivalently good fits. Areas for the fitted features were approximated by the maximum height x FWHM. It was found that this approximation gave within error the same results as an analysis which utilized the actual integrated intensities. The reported intensity ratios between features modeled in the fit is the average ratio for the series of equivalently good fits; the error is the standard deviation.

3.2.6. Error Analysis

There are several possible sources of systematic error in this analysis. Normalization procedures can introduce a 1-3% difference in pre-edge peak heights as determined by varying the parameters used to normalize a set of Cl K-edge spectra, while still requiring the final fits to meet requirements of consistency. This ~3% error is reported for peak heights when comparisons between two sets of data are being made. However, for comparison of intensities of several features in a given spectrum, the difference has been scaled for all features and normalization does not introduce significant variation in the ratios between features. Further, the choice of functions/parameters used to fit spectra can also introduce errors. Estimation of this error requires comparing fits to the data which

use a variety of functions and parameters defining those functions. In the analysis of the fitting of z-polarized Cu K-edge of D_{2d} $CuCl_4^{2-}$, while the absolute variation in the intensities of given features was large (up to ~8%), the variation in the range of ratios between features was much less. Comparison of all reasonable fits showed a range of less than 1%, while inclusion of less-good fits with different fitting functions only increased this range to 1.5%. This error is reported in the analysis. In less complicated spectra (e.g., the S K-edges described herein), the error introduced by fitting is minimal.

3.2.7. SCF-Xα-SW Calculations

Standard SCF-Xα-SW calculations on the Cu-tet *b* molecule were performed on DEC station 3100 computers with between 300 and 400 iterations required for convergence. The calculations were considered to have converged when the largest relative change in the potential between subsequent iterations was less than 10^{-4}. Each nitrogen ligated to the copper was approximated by an amine group and the thiolate group was modeled with methyl thiolate. The Cu-tet *b* calculation was performed with a 5-coordinate geometry having idealized C_s symmetry. Distances and angles were averaged from the crystal structure values. The coordinate system was chosen to reproduce the experimentally observed d_{x2-y2} ground state. The position of the atoms, sphere radii, α values, and maximum values for the azimuthal quantum number are given in Table 3.1. Sphere radii used were the same as in the previous calculation on Pc which were chosen by fitting the calculation to the experimental g-values.[5] The α values were those determined by Schwarz[41] and a Watson sphere coincident with the outer sphere radius was used in calculations of charged species. Optical transition energies were determined by using the Slater transition state formalism.

3.3. Results and Analysis

3.3.1. Cu K-edge Spectroscopy

3.3.1.1. Cu 1s —> 3d quadrupole transition intensity. Figure 3.2 shows the polarized Cu K-edge spectra of D_{4h} $CuCl_4^{2-}$. Because the inversion symmetry of the anion precludes Cu 4p mixing into the ground state orbital, the 1s —> 3d pre-edge transition is not expected to have any electric dipole intensity. However, the spectra clearly show pre-edge transition intensity in the 8979 eV region. The maximum intensity is observed for the *xy*-orientation (Figure 3.2a) for which $\phi = 45^\circ$ and in which the half-

Table 3.1. Input Parameters for Cu-tet *b* SCF-Xα–SW Calculation.

	position†			sphere		
Atom	x	y	z	radius	α value	l_{max}
Out	0.0000	0.0000	0.0000	9.35	0.73663	4
Cu	0.0000	0.0000	0.0000	2.95	0.70697	3
S	4.5213	0.0000	0.0000	2.50	0.72475	2
N1	-0.13411	0.0000	3.8316	1.90	0.75197	2
-H	0.79000	-1.6427	4.5346	1.17	0.77725	0
-H	0.79000	1.6427	4.5346	1.17	0.77725	0
-H	-2.0528	0.0000	4.4360	1.17	0.77725	0
N2	-0.13411	0.0000	-3.8316	1.90	0.75197	2
-H	0.79000	1.6427	-4.5346	1.17	0.77725	0
-H	0.79000	-1.6427	-4.5346	1.17	0.77725	0
-H	-2.0528	0.0000	-4.4360	1.17	0.77725	0
N3	-2.5480	3.2568	0.0000	1.90	0.75197	2
-H	-2.2141	4.3690	1.6426	1.17	0.77725	0
-H	-2.2141	4.3690	-1.6426	1.17	0.77725	0
-H	-4.4551	2.6170	0.0000	1.17	0.77725	0
N4	-2.5480	-3.2568	0.0000	1.90	0.75197	2
-H	-2.2143	-4.3689	-1.6426	1.17	0.77725	0
-H	-2.2143	-4.3689	1.6426	1.17	0.77725	0
-H	-4.4551	-2.6170	0.0000	1.17	0.77725	0
C	5.5807	0.0000	-3.2607	1.80	0.75928	2
-H	4.8860	-1.6426	-4.1911	1.17	0.77725	0
-H	4.8860	1.6426	-4.1911	1.17	0.77725	0
-H	7.5916	0.0000	-3.3130	1.17	0.77725	0

† coordinates are in Bohr units.

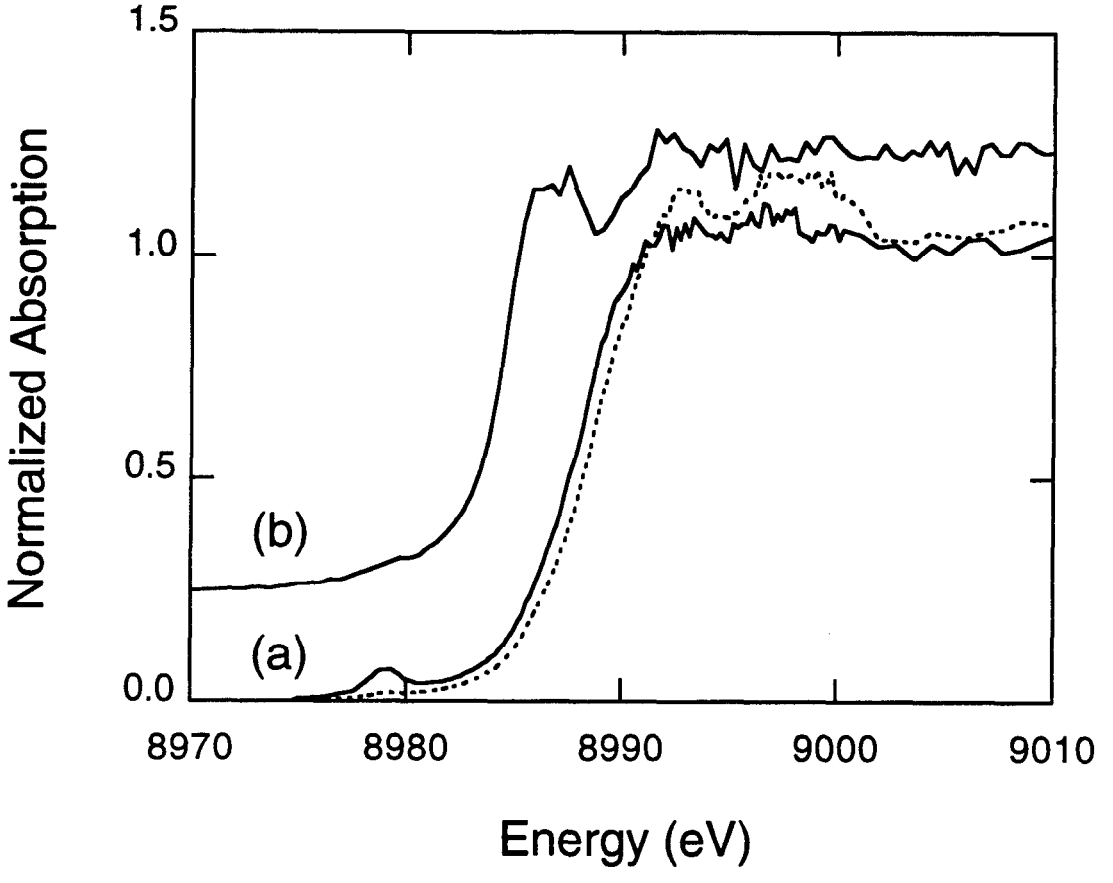

Figure 3.2. Polarized Cu K-edge spectra of D_{4h} $CuCl_4^{2-}$. (a) *xy*-polarized orientations for values of $\phi = 0^o$ (----) and $\phi = 45^o$ (——), where ϕ is collinear with the crystallographic *c*-axis (taken from reference 16). The Cu 1s —> 3d quadrupole transition intensity at ~8979 eV varies as $\sin^2(2\phi)$. (b) *z*-polarized orientation (——). The prominent feature at ~8986 eV is assigned as the 1s —> 4p + LMCT shakedown transition.

occupied $3d_{x2-y2}$ orbital transforms as d_{xy} in the coordinate frame of the incoming radiation; the molecule lies in the plane of the polarization and the polarization vector, **E**, bisects the Cl-Cu-Cl (90°) angles. It has been shown previously that this ~8979 eV feature can be assigned as a 1s —> 3d quadrupole transition.[16] At Cu K-edge energies (9000 eV) the X-ray photon wavelength (λ = 1.38 Å) is not large relative to the orbital of the electron and higher order terms in the transition moment multipole expansion become significant. The intensity of the *xy*-polarized 1s —> 3d feature does not go to zero at the minimum of the quadrupole variation ($\phi = 0°$). A close examination of the crystal structure of this system shows that there are two $CuCl_4^{2-}$ molecules per unit cell whose *z*-axes are equally displaced from the crystallographic *c*-axis and whose *xy* planes are rotated ~15° from one another. This non-alignment of the molecules accounts for ~22% of the residual intensity in the pre-edge feature. The experimental uncertainty in the crystal alignment (~5°) accounts for an additional ~10%, assuming the full 5° misalignment. The remaining intensity probably has its origin in vibronic coupling.[42] The *z*-polarized spectrum of D_{4h} $CuCl_4^{2-}$ in Figure 3.2b exhibits a weak pre-edge feature at ~8979 eV, the intensity of which is comparable to the minimum *xy*-polarized intensity at $\phi = 0°$. This feature has been observed by Kosugi and coworkers in a previous study of this complex.[43] The quadrupole transition will not contribute to pre-edge intensity in the *z*-polarized spectrum, so this weak feature must also originate from vibronic coupling. The most prominent feature in the *z*-polarized spectrum is a very intense feature at 8986.1 eV, which is absent in the *xy*-polarized spectrum. The intensity of the feature suggests that it is an allowed transition and is probably associated with the 1s —> 4p transition. As will be described later in this chapter, a previous Cu K-edge XAS study of copper(II) model complexes (including D_{4h} $CuCl_4^{2-}$) assigned this feature as a Cu 1s —> 4p transition with a simultaneous ligand-to-metal CT (LMCT) shakedown.[14,15] Based on results from *ab initio* calculations, Kosugi and coworkers also assigned this feature as a 1s —> 4p + LMCT shakedown transition.[43]

The polarized Cu K-edge study of D_{4h} $CuCl_4^{2-}$ shows that quadrupole intensity contributes to 1s —> 3d transition intensity at ~8979 eV. For other copper(II) systems the quadrupole contribution to the 1s —> 3d transition intensity will be similar to that in D_{4h} $CuCl_4^{2-}$, assuming that the magnitude of the $3d_{x2-y2}$ orbital character in the ground state wavefunction is similar. The quadrupole transition intensity is not isotropic; it will contribute in non-polarized and *xy*-polarized spectra.

3.3.1.2. Non-polarized Cu 1s —> 3d intensity. Non-polarized Cu K-edge X-ray absorption spectra for D_{4h} and D_{2d} $CuCl_4^{2-}$ and for Pc are shown in Figure 3.3. All have a feature at ~8979 eV, which can be assigned as the 1s —> 3d

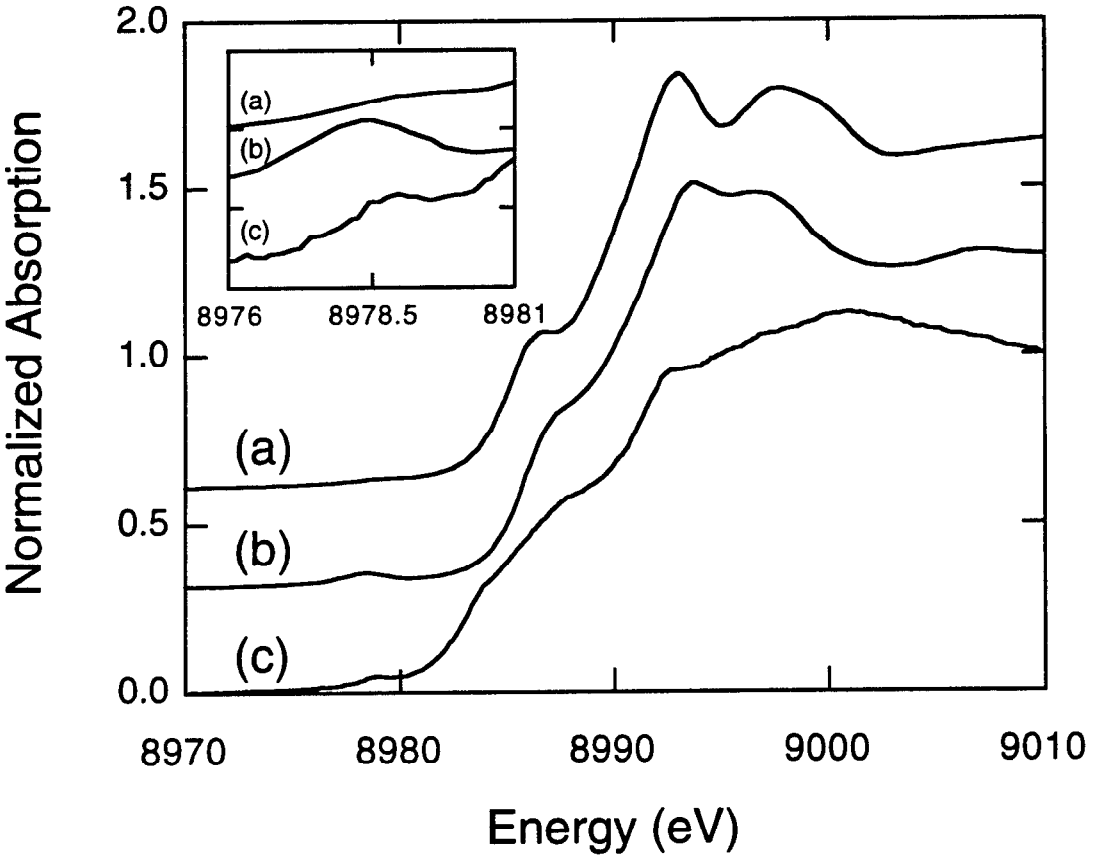

Figure 3.3. Non-polarized (isotropic) Cu K-edge spectra of (a) D_{4h} $CuCl_4^{2-}$, (b) D_{2d} $CuCl_4^{2-}$, and (c) plastocyanin . Inset shows pre-edge region intensities multiplied by a factor of five (5). The greater intensity in the 1s —> 3d transition at ~8987 eV in both D_{2d} $CuCl_4^{2-}$ and plastocyanin is due to 4p mixing into the ground state orbital, giving the feature electric dipole allowed intensity.

transition. The observed pre-edge intensity (Figure 3.3, inset) for the D_{2d} complex is about 3 times as intense as in the D_{4h} complex, while that of Pc is about 2 times as intense as in the D_{4h} complex. Xα calculations[13] indicate that the $3d_{x^2-y^2}$ component of the ground state is similar for D_{4h} and D_{2d} $CuCl_4^{2-}$, being 61% and 67% respectively. Thus, the quadrupole intensity in the D_{4h} spectrum can be taken as a baseline for the feature in the spectrum of the D_{2d} complex. Xα calculations on the blue copper site[4,5] indicate that the ground state is only 42% $3d_{x^2-y^2}$. Thus, it is expected that the contribution to the intensity from the quadrupole transition in Pc will be less than in the D_{4h} case. The source of the additional intensity in the D_{2d} complex and Pc must therefore be attributed to 4p mixing into the ground state.

3.3.1.3. Cu 1s —> 4p + LMCT shakedown transition intensity. The nature of the 4p mixing into the $3d_{x^2-y^2}$ ground state of D_{2d} $CuCl_4^{2-}$ has been investigated with single crystal polarized experiments. Figure 3.4 shows the *y*- and *z*-polarized spectra of D_{2d} $CuCl_4^{2-}$ (note that the *x*- and *y*-polarizations are equivalent in this system). The *y*-polarized spectrum exhibits no pre-edge feature, while the ~8979 eV pre-edge feature is present in the *z*-polarized spectrum. In the *y*-polarized orientation the half-occupied $3d_{x^2-y^2}$ orbital does not transform as d_{xy} in the coordinate frame of the incoming radiation so the quadrupole transition is not expected to be observed. There is also no *y*-polarized electric dipole intensity, ruling out $4p_{x,y}$ mixing into the ground state orbital. The *z*-polarized ~8979 eV feature must originate from $4p_z$ mixing into the ground state, as the quadrupole transition does not contribute to *z*-polarized spectra. Note that it is this $4p_z$ mixing which has been postulated to reduce the EPR parallel hyperfine splitting of this complex.

Additionally, in the *z*-polarized spectrum, there is a well-resolved feature on the rising edge at ~8987 eV. This is comparable to the ~8986 eV feature in the *z*-polarized spectrum of D_{4h} $CuCl_4^{2-}$ in Figure 3.2b. This transition is assigned as a Cu 1s —> 4p + ligand-to-metal CT (LMCT) shakedown transition made allowed by final state relaxation. A previous study of a series of copper(II) compounds found that this feature appears between 8986 and 8988 eV in all complexes studied.[14] In systems characterized by more covalent interactions with the ligands, the feature appears in the lower end of this energy range.[14] The process of excitation of a 1s core electron into the 4p orbital (an electric dipole allowed transition) creates a core hole, which results in an increased effective nuclear charge felt by the valence orbitals. This causes relaxation of the copper valence orbitals to deeper binding energies (Figure 3.5). The half-occupied $3d_{x^2-y^2}$ orbital relaxes to an energy below that of the ligand valence levels. As a result of this relaxation, a lower energy configuration is possible; an electron from the ligand valence is transferred to the copper and fills the $3d_{x^2-y^2}$ orbital. This excited configuration gives rise

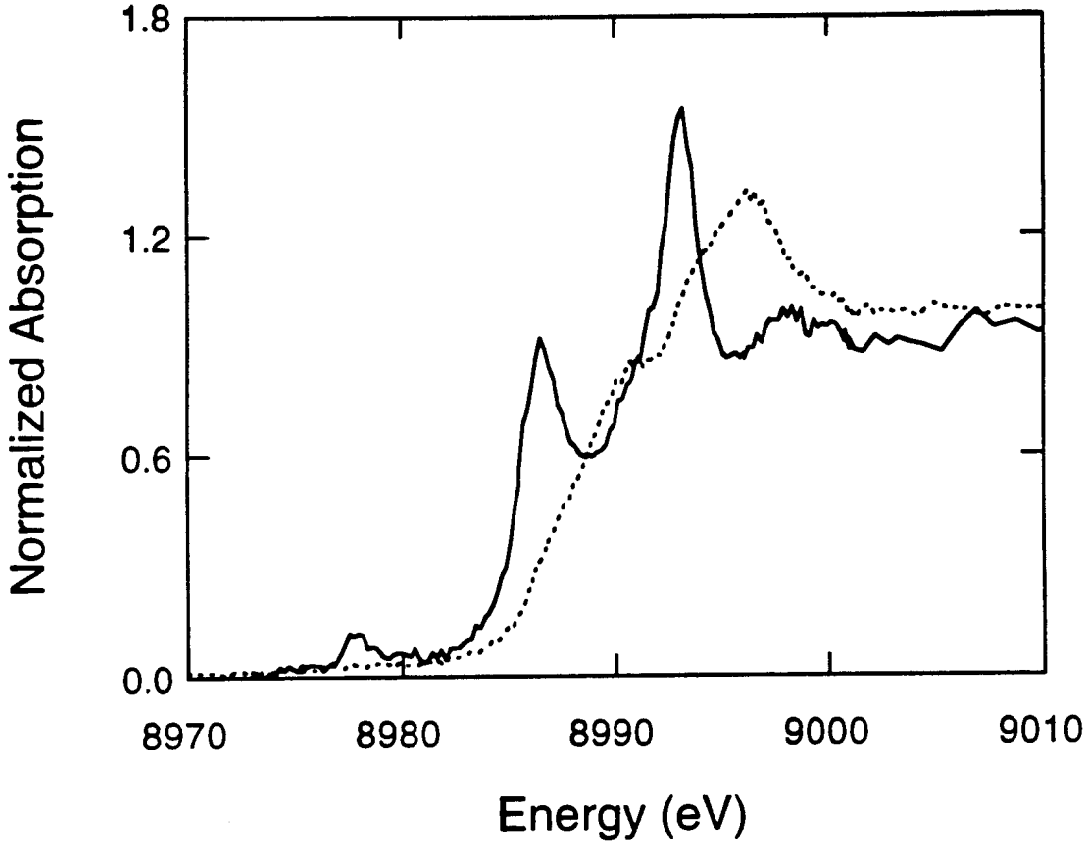

Figure 3.4. Polarized Cu K-edge spectra of D_{2d} $CuCl_4^{2-}$. *z*-polarized spectrum (——); *y*-polarized spectrum (-----). The feature in the *z*-polarized spectrum at ~8979 eV is assigned as the 1s —> 3d ($+4p_z$) transition. The feature in the *z*-polarized spectrum ~8987 eV is assigned as the 1s —> 4p + LMCT shakedown transition

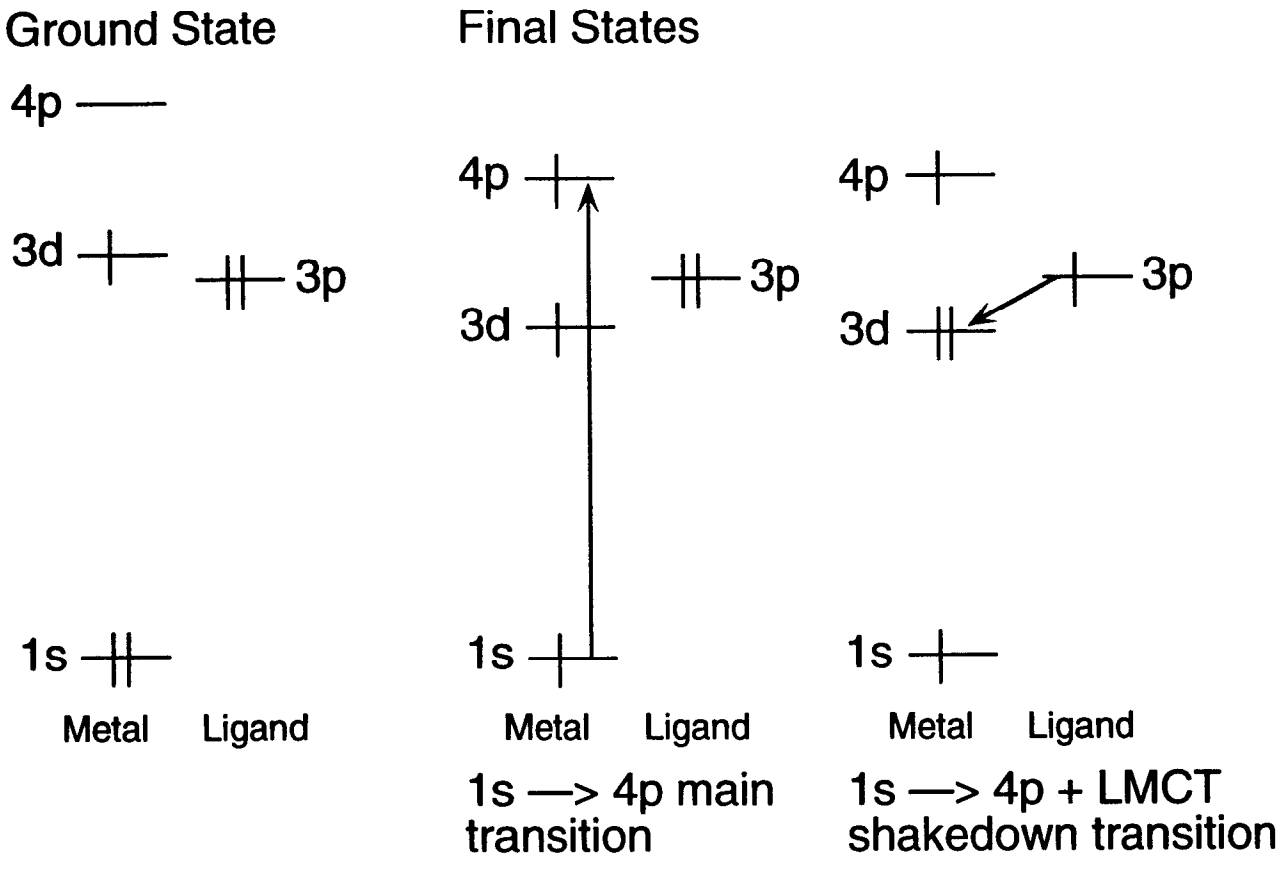

Figure 3.5. Schematic description of 1s —> 4p Cu K-edge transition and its associated shakedown transition. Left: ground state configuration. Center: excited 1s —> 4p final state with relaxation of valence levels due to the creation of a core hole. Right: excited final state associated with the 1s —> 4p + LMCT shakedown transition.

to a lower energy transition, observed as a feature on the rising edge. Covalency increases as the ligand ionization energy decreases; the ligand valence level comes closer in energy to the half-occupied Cu 3d orbital in the ground state. As the energy of the ligand 3p level increases, the stabilization of the 3d orbital upon core ionization relative to the ligand 3p orbital becomes greater. Thus, one would expect the energy of the shakedown transition to decrease as the covalency increases, which is the experimentally observed result.[14] Further, a shakedown assignment is required in the interpretation of the Cu(II) 2p XPS spectrum,[13] and its extension to the 1s core absorption is reasonable and consistent with *ab initio* calculations.[43,44]

The observed shakedown is analogous to the satellites observed in PES spectra and can be treated in a similar manner.[13] This treatment enables us to quantify the intensity of the 1s —> 4p + LMCT shakedown feature as a percentage of the total 1s —> 4p transition intensity. Comparison of the shakedown intensity to that of the 1s —> 3d(+4p) transition (~8979 eV) then allows for quantitation of the amount of $4p_z$ mixing into the ground state 3d orbital. In the sudden approximation,[45-47] the creation of the core hole occurs rapidly, before the remaining electrons adjust to the new potential. The intensity, I_i, of a given transition, i, corresponding to either the main or shakedown final state can then be expressed as

$$I_i = \left|\langle \psi_i(\underline{c}) | \psi_R(\underline{c}) \rangle\right|^2$$

where $\underline{c}$ denotes a core hole, ψ_i denotes the relaxed final states (the main and the shakedown peaks) and ψ_R is the initial unrelaxed state with the core electron removed. This implies that only initial and final states with the same symmetry can contribute to shakedown intensity. Quantitation of this process and determination of the intensity ratio of the main peak to the shakedown peak can be obtained through the use of a Configuration Interaction type model. The ground state wavefunction ψ_g for the D_{2d} complex is obtained by diagonalizing the energy matrix

$$\begin{vmatrix} \langle \psi(3d^9)|H|\psi(3d^9)\rangle - E' & \langle \psi(3d^9)|H|\psi(3d^9\underline{L})\rangle \\ \langle \psi(3d^9)|H|\psi(3d^9\underline{L})\rangle & \langle \psi(3d^{10}\underline{L})|H|\psi(3d^{10}\underline{L})\rangle - E' \end{vmatrix} = 0$$

where $\psi(3d^9)$ and $\psi(3d^{10}\underline{L})$ represent the one hole metal state and the d^{10} metal/one hole ligand state, respectively. Diagonalization gives the eigenvector corresponding to the lowest energy state as equation 3.1,

$$\psi_g = \cos\theta\left|3d^{10}\right\rangle - \sin\theta\left|3d^9\underline{L}\right\rangle \tag{3.1}$$

with $\tan 2\theta = 2T/\Delta$, $T = \left\langle \psi\left(3d^9\right)\middle|H\middle|\psi\left(3d^{10}\underline{L}\right)\right\rangle$, and $\Delta = \left\langle \psi\left(3d^9\right)\middle|H\middle|\psi\left(3d^9\right)\right\rangle - \left\langle \psi\left(3d^{10}\underline{L}\right)\middle|H\middle|\psi\left(3d^{10}\underline{L}\right)\right\rangle$. T is the interaction matrix element between the configurations contributing to the ground state wavefunction and Δ is the energy difference between the two configurations, as shown in Figure 3.6a.

The 1s —> 4p transition and corresponding creation of the core hole produce two possible final states corresponding to a main (ψ_m) and a shake down (ψ_s) peak. The interaction matrix for the excited states is constructed in an analogous fashion as for the ground state, with the addition of a term (Q) to the diagonal energy of the $\underline{c}3d^9$ configuration to account for the increase in the effective nuclear charge felt by the $3d^9$ state (Figure 3.6b). The solutions for the excited states wavefunctions are given by equations 3.2a and b, where $\underline{c}$ indicates a Cu 1s core hole and $\tan 2\theta' = 2T/(\Delta - Q)$; $0 < \theta' < 90^\circ$.

$$\psi_m = \sin\theta'\left|\underline{c}3d^9\right\rangle - \cos\theta'\left|\underline{c}3d^{10}\underline{L}\right\rangle \tag{3.2a}$$

$$\psi_s = \cos\theta'\left|\underline{c}3d^9\right\rangle - \sin\theta'\left|\underline{c}3d^{10}\underline{L}\right\rangle \tag{3.2b}$$

The energy splitting, W, between the main and shakedown peaks is given by equation 3.3.

$$W = \left[(\Delta - Q)^2 + 4T^2\right]^{1/2} \tag{3.3}$$

The main to shakedown peak intensity ratio (I_m/I_s) is given by equation 3.4.

$$\frac{I_m}{I_s} = \left(\frac{\sin\theta'\cos\theta - \cos\theta'\sin\theta}{\cos\theta'\cos\theta + \sin\theta'\sin\theta}\right)^2 = \tan^2(\theta' - \theta) \tag{3.4}$$

Thus, the intensity ratio is determined by the change in the wavefunction, θ'-θ, upon the creation of a 1s core hole. PES satellite features have already provided an analysis of $CuCl_4^{2-}$ complexes for ionization of a 2p core electron.[13] The PES study found that $\Delta = 0.88$ eV, $T = 1.5$ eV, $Q = 8.9$ eV and $W = 8.20$ eV for the D_{2d} $CuCl_4^{2-}$ complex. Because Δ and T are ground state parameters, the values determined in the PES study can be used in the analysis of the XAS shakedown intensity in D_{2d} $CuCl_4^{2-}$. The value of Q for the 1s —> 4p promotion is not known. As a first approximation, the relaxation Q, is assumed to be the same for as the 2p ionization. Our analysis, then, takes the following approach: i) use ground state values for $CuCl_4^{2-}$ as determined by PES; ii) assume

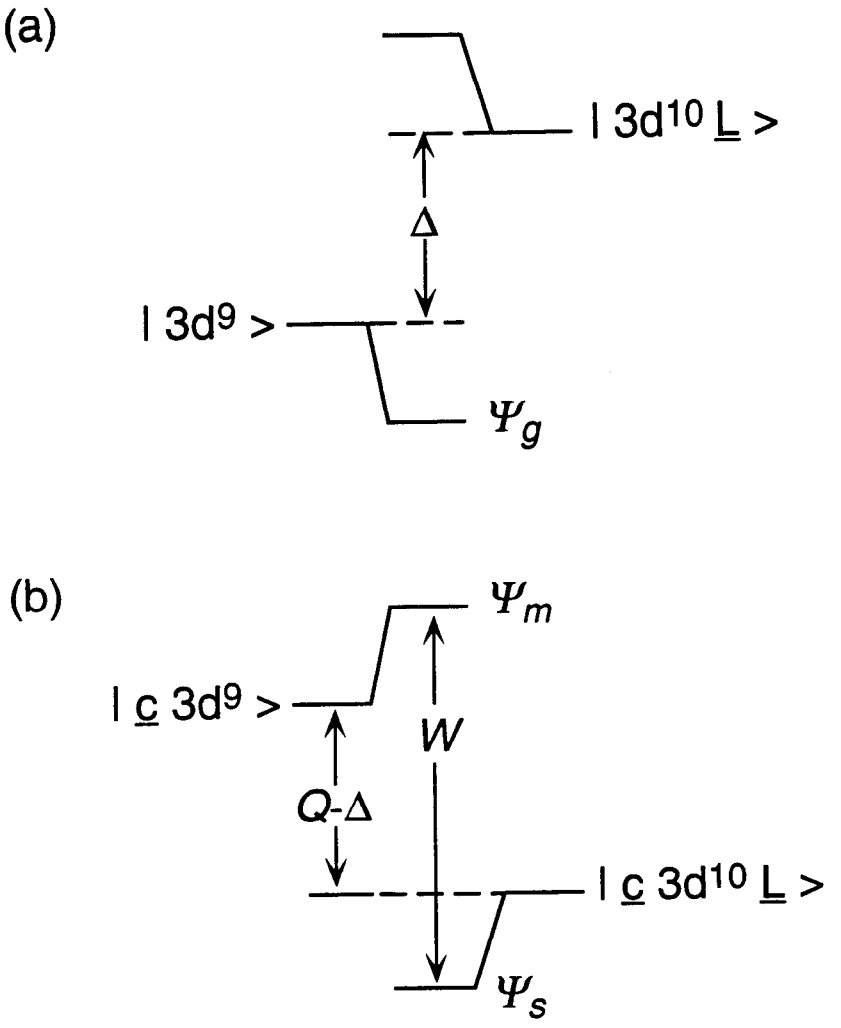

Figure 3.6. Configuration interaction formalism for analysis of the Cu K-edge near-edge structure. (a) Ground state wavefunctions are determined by the parameters T and Δ. (b) Final state wave functions. The lower-energy 1s —> 4p + LMCT shakedown final state (ψ_s) is separated in energy from the main 1s —> 4p transition (final state, ψ_m) by the splitting W.

W=8.20 eV as a first approximation for the energy splitting between the main and shakedown features; iii) fit the data to quantitate intensities and to obtain experimental energy splittings.

The fitting procedures showed that a feature could not reasonably be fit at 8.20 eV above the shakedown feature energy. However, the fit consistently required a feature 6.6 eV above the shakedown feature. The feature at 8993.1 eV in the *z*-polarized spectrum in Figure 3.4 is thus assigned as the 1s —> 4p main transition. The observed energy splitting relative to the shakedown peak (W = 6.6 eV) was used to calculate the relaxation in the system to find that Q = 6.8 eV. This relaxation is less than that of a 2p ionization because the promoted electron is in a bound valence state, reducing the effective nuclear charge felt by the valence orbitals.

Using this adjusted value of Q, the I_m/I_s intensity ratio is calculated to be 0.69. Thus the main transition contains 41% of the 1s —> 4p transition intensity and the shakedown transition contains 59%. The fitting procedure gave a I_m:I_s ratio of ~60:40. However, the fitted intensity of the main transition (I_m) is complicated by the rising edge background. This fit to both the data and to the second derivative of the data for the *z*-polarized D_{2d} XAS spectrum is shown in Figure 3.7. An examination of the resultant equivalently good fits (Table 3.2) shows that the ratios between features in the fitted spectrum is relatively constant, despite small changes in the absolute areas of the features. Further, the ratio between the areas of the ~8979 eV (1s —> 3d (+4p)) transition and the ~8987 eV shakedown feature is found to be

$$\frac{I(\sim 8979)}{I(\sim 8987)} = 0.0636 \pm 0.0005$$

The 4p mixing into the $3d_{x^2-y^2}$ ground state can now be determined because the intensity of the transition will be proportional to the amount of electric dipole transition character in that transition integral. Quadrupole contribution to the intensity of the ~8979 eV feature need not be considered because it is not allowed for the *z*-polarization. As calculated from the intensity ratio, I_m/I_s, the shakedown feature reflects 59% of the pure 1s —> 4p transition. The 1s —> 3d(+4p) transition must then reflect 3.8 ± 1.5% 4p character. Thus, there is ~4% $4p_z$ mixing into the ground state of D_{2d} $CuCl_4^{2-}$. This result is consistent with Xα calculations on this site.[13] As in the D_{4h} $CuCl_4^{2-}$ complex, vibronic coupling may contribute to the intensity of the ~8979 eV feature in this system. Thus, the 3.8% 4p mixing from the above analysis reflects an upper limit of the magnitude of direct 4p mixing in the half-occupied orbital of this complex.

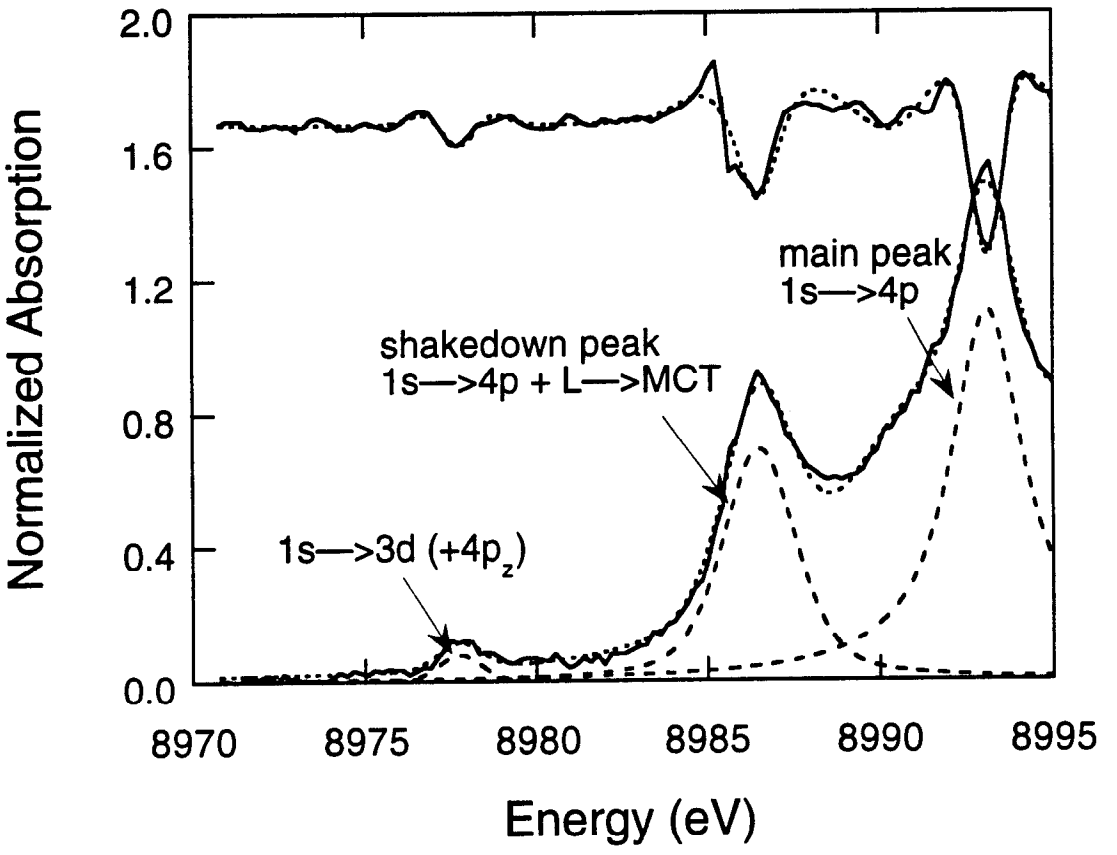

Figure 3.7. Representative fit to the data (bottom) and the second derivative (top) of z-polarized Cu K-edge spectra of D_{2d} $CuCl_4^{2-}$. Fit is represented by a dashed line. Shown in the fit to the data are the functions used to model the 1s —> 3d ($+4p_z$) transition at ~8979 eV, the 1s —> 4p + LMCT transition at ~8987 eV and the 1s —> 4p main transition at ~8993 eV. The intensity of the main transition is not well established due to the rising edge background.

Table 3.2. Non-linear Least Squares Fits of *z*-polarized Cu K-edge XAS Spectrum of D_{2d} $CuCl_4^{2-}$†§

		Peak 1[a] (Gaussian)	Peak 2[b] (Gaussian/Lorentzian)	Peak 3[c] (Lorentzian)	Peak 4[d] (Lorentzian)	Ratio: Peak 1/ Peak 2
FIT A	Ht	0.075642	0.39879/0.29177	0.49692	1.0991	
	FWHM	1.4768	2.454/2.6102	4.8	2.5763	0.0642
	Center	8977.8	8986.5	8990.5	8993.1	
FIT B	Ht	0.075936	0.39137/0.30306	0.49392	1.1042	
	FWHM	1.4796	2.4643/2.6306	4.7	2.5830	0.0639
	Center	8977.8	8986.5	8990.5	8993.1	
FIT C	Ht	0.076211	0.38398/0.31429	0.49086	1.1094	
	FWHM	1.4821	2.4751/2.63296	4.6	2.5899	0.0636
	Center	8977.8	8986.5	8990.5	8993.1	
FIT D	Ht	0.076464	0.37663/0.32540	0.48772	1.1145	
	FWHM	1.4845	2.487/2.6372	4.5	2.5971	0.0632
	Center	8977.8	8986.5	8990.5	8993.1	
FIT E	Ht	0.076692	0.36935/0.33636	0.48449	1.1195	
	FWHM	1.4866	2.5003/2.6433	4.4	2.6044	0.0629
	Center	8977.8	8986.5	8990.4	8993.1	
Average Peak Area		0.1129	1.7764		2.8734	0.0636
Standard Deviation		0.0009	0.0287		0.0333	0.000514

† Underlined values indicate that the parameter was fixed during this fit.

§ An additional Lorentzian function (not shown) was used to model the rising edge background

[a] Peak 1 models the 1s —> 3d transition at ~8979 eV.

[b] Peak 2 models the 1s —> 4p + LMCT shakedown transition at ~8987 eV.

[c] Peak 3 was required to reproduce the data and the second derivative of the data.

[d] Peak 4 models the 1s —> 4p main transition 6.6 eV above the shakedown transition.

The results of this shakedown analysis are inconsistent with the requirement that there be 12% $4p_z$ mixing in the ground state of D_{2d} $CuCl_4^{2-}$ to reproduce the observed small hyperfine splitting in the EPR spectra. An alternative explanation for the small EPR parallel hyperfine must therefore be considered.

3.3.1.4. Cu 1s —> 3d transition in plastocyanin: Cu 4p-mixing. Polarized single crystal XAS studies at the Cu K-edge of Pc provide a probe of Cu 4p mixing into the active site ground state. Figure 3.8 presents polarized X-ray absorption spectra of oriented Pc crystals, previously published in reference 17. A pre-edge feature at ~8979 eV, assigned as the 1s —> 3d(+4p) transition, is maximized in the *xy*-polarized spectrum and absent in the *z*-polarized spectrum. Because the orientation which gives rise to the spectrum in Figure 3.8b places the *x,y* plane perpendicular to the propagation of light, it exhibits no quadrupole intensity. The non-polarized Cu K-edge data (Figure 3.3c) show that the Pc 1s —> 3d transition has electric dipole intensity which is attributed to 4p mixing into the ground state wavefunction. The data in Figure 3.8 clearly show that the 1s —> 3d(+4p) electric dipole transition is *x,y* polarized; thus it must be $4p_{x,y}$ mixing which accounts for the observed intensity. The electric dipole intensity in this feature varies as $\cos^2\phi$ and is maximized ($\phi = 0^\circ$) when the polarization vector is coincident with the p-orbital which is allowed by group theory to mix with the $3d_{x^2-y^2}$ orbital.[48] The four molecules in the Pc unit cell are aligned such that the p orbitals responsible for electric dipole intensity are oriented in two sets at 90° to each other. Thus, in contrast to the previous interpretation of these data,[17] the electric dipole intensity is isotropic with respect to the *xy* plane of the Pc crystal system. (Data not shown). Note that both the effective C_{3v} symmetry determined by ligand field analysis and the Xα calculations predicted this $p_{x,y}$ mixing into the Pc ground state.

The absence of any 1s —> 3d pre-edge intensity in the *z*-polarized spectrum rules out the possibility of p_z mixing in the ground state wavefunction of the blue copper site. Thus, 12% $4p_z$ mixing into the Cu $3d_{x^2-y^2}$ ground state cannot be the explanation for the observed small hyperfine splitting in the EPR spectra of blue copper proteins.

3.3.2. Ligand K-edge Spectroscopy

3.3.2.1. Cl K-edge Spectroscopy. It is clear from the Cu K-edge studies that the origin of the small $A_{\|}$ splitting in the EPR spectra of D_{2d} $CuCl_4^{2-}$ and blue copper centers is not $4p_z$ mixing. The alternative explanation for the reduced hyperfine splitting, high covalency, has therefore been explored experimentally. An estimate of the covalency of a metal-ligand bond can be obtained from ligand K-edge studies. A previous study by

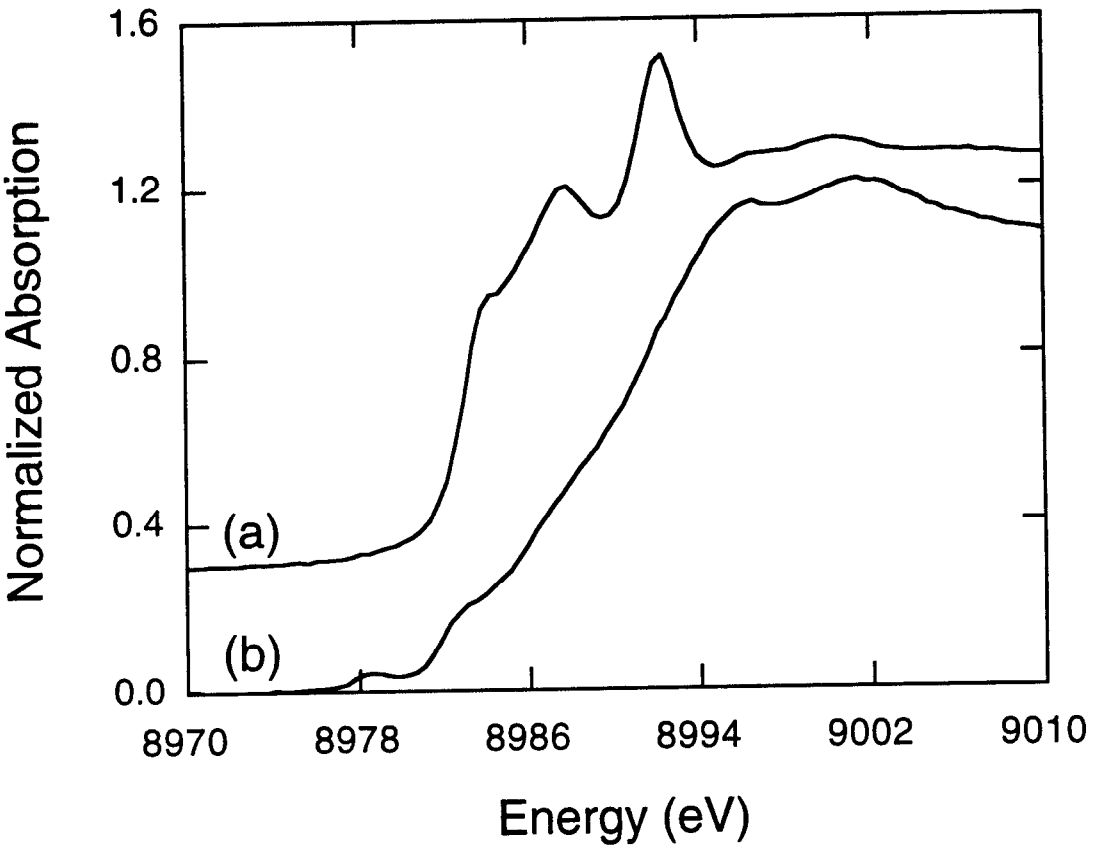

Figure 3.8. Polarized Cu K-edge spectra of poplar plastocyanin. (a) *z*-polarized spectrum and (b) *xy*-polarized spectrum. The feature at ~8979 eV in the *xy*-polarized spectrum indicates that the plastocyanin ground state is characterized by $p_{x,y}$ mixing. The absence of pre-edge intensity in the *z*-polarized spectrum reveals there is no p_z mixing. (Data are taken from reference 17).

Hedman and coworkers showed that the Cl K-edge spectra of D_{4h} and D_{2d} $CuCl_4^{2-}$ exhibit a well-resolved, intense pre-edge feature at ~2820 eV.[26] As discussed in Chapter 1 (equation 1.3c), the intensity of the transition is proportional to the covalent mixing of the Cu $3d_{x^2-y^2}$ with the four chloride ligands due to bonding.

Figure 3.9, which presents higher resolution data than reference 26, shows that the pre-edge feature in D_{2d} $CuCl_4^{2-}$ is less intense than in D_{4h} symmetry and that the feature in the D_{2d} spectrum lies at 0.4 eV lower energy. Analysis of EPR superhyperfine splitting in D_{4h} $CuCl_4^{2-}$ has established that its ground state orbital is best described as 61% Cu $3d_{x^2-y^2}$ and 39% Cl 3p.[49] If $\alpha'^2 = 0.39$ for D_{4h}, one can compare the experimental pre-edge intensities to determine that $\alpha'^2 = 0.29$ for D_{2d} $CuCl_4^{2-}$. Thus, the ground state orbital in D_{2d} $CuCl_4^{2-}$ is ~71% Cu $3d_{x^2-y^2}$ and ~29% Cl 3p,[50] in good agreement with Xα calculations which predict 67% $3d_{x^2-y^2}$ in the ground state.[13] Thus, the Cl K-edge data show that the small EPR $A_{\|}$ hyperfine in the D_{2d} site also cannot be explained by a high degree of $3d_{x^2-y^2}$ covalency for the site. The origin of this splitting is addressed in the Discussion section of this chapter.

3.3.2.2. S K-edge Spectroscopy. Sulfur K-edge data of the thiolate model complex, Cu-tet *b*, and Pc are shown in Figure 3.10. Both spectra have an intense, well-resolved pre-edge feature ~2470 eV assigned as a S(thiolate) 1s —> ψ^* transition, where ψ^* is the molecular orbital containing Cu $3d_{x^2-y^2}$ and S(thiolate) 3p orbital character. In both spectra the data are normalized to an edge jump of one sulfur. Pc has a total of three sulfur atoms, but only the cysteine sulfur ligand has overlap with the Cu $3d_{x^2-y^2}$ orbital and contributes to pre-edge intensity. (One of the sulfur residues is not ligated to the copper. From single crystal EPR it is known that the methionine sulfur ligand bond is perpendicular to the half-occupied orbital and has no net overlap with this orbital.[12] Xα calculations[4] have further verified that there is no S(Met) character in the half-occupied orbital. Note that the S(Met) does undergo a bonding interaction with the fully-occupied d_{z^2} orbital.). To compare pre-edge intensities the Pc spectrum must thus be re-normalized by a factor of three (3) (Figure 3.10, inset). The pre-edge intensity of Pc is much greater than that of Cu-tet *b*. Both the Cu-tet *b* and Pc re-normalized pre-edge regions were fit as described in the experimental section; the Cu-tet *b* pre-edge intensity (approximated by the height x FWHM) is 0.38, while the Pc intensity is 0.97. Because the pre-edge intensity is a direct probe of the covalency of the Cu-S bond, these data clearly show that, relative to the Cu-tet *b* complex, Pc has a highly covalent Cu-S(Cys) bond.

In order to interpret the covalency reflected in the S K-edge pre-edge intensities in a more quantitative fashion, it is important to have an understanding of the electronic structure of the Cu-tet *b* model complex and its relation to the electronic structure of Pc.

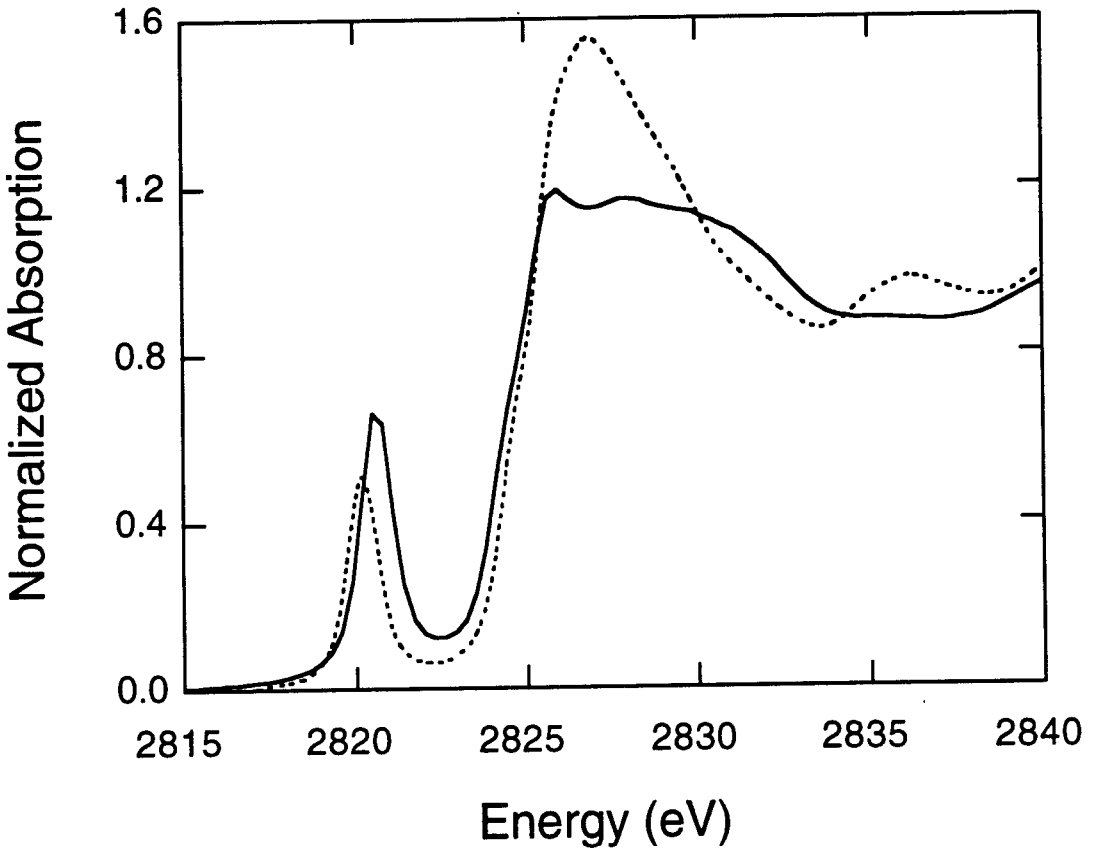

Figure 3.9. Cl K-edge spectra of D_{4h} $CuCl_4^{2-}$ (—) and D_{2d} $CuCl_4^{2-}$ (----). The pre-edge feature at ~2820 eV is assigned as a Cl 1s —> ψ^* transition, where ψ^* is an antibonding molecular orbital with both Cl 3p character and Cu $3d_{x2-y2}$ character. The intensity reflects the magnitude of the electric dipole allowed component of the transition (Cl 3p) and therefore reflects the covalent contribution of the ligand to ψ^*.

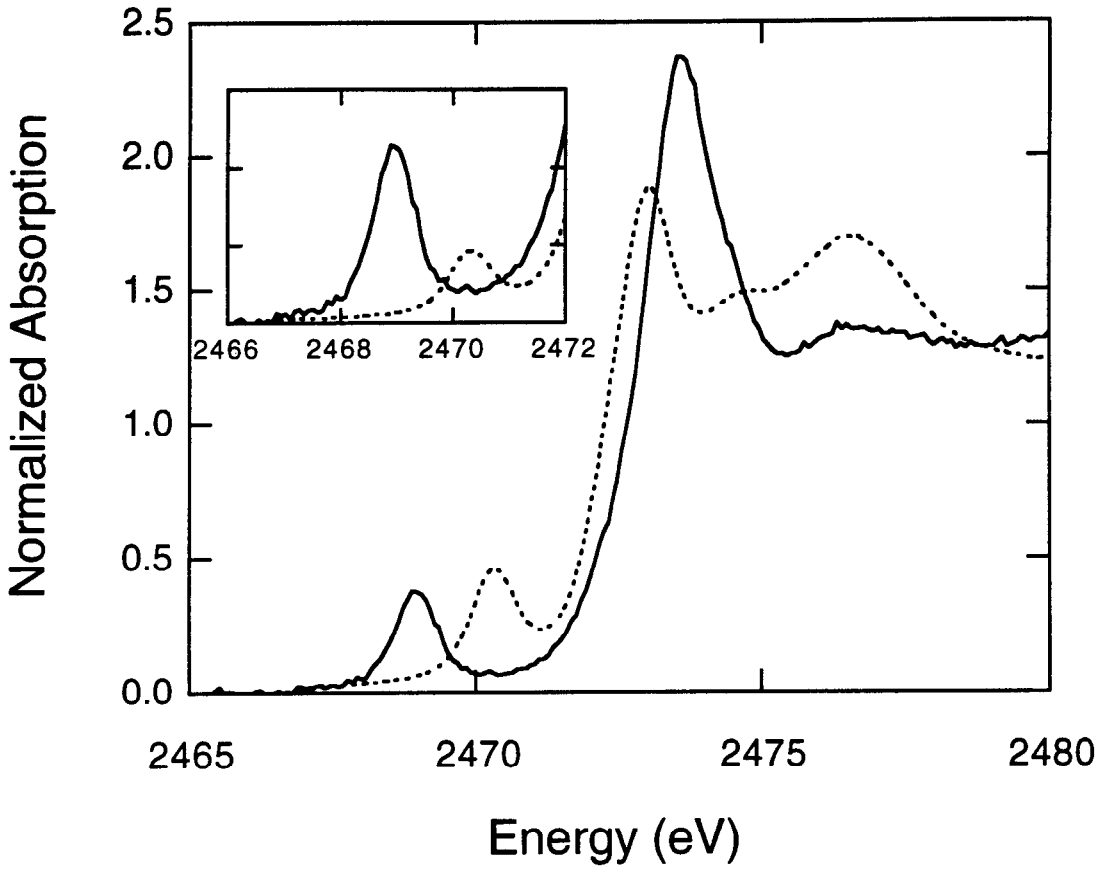

Figure 3.10. S K-edge spectra of the blue copper model, Cu-tet *b* (---) and spinach plastocyanin (—). The inset shows the pre-edge regions of the spectra only, with the plastocyanin data rescaled by a factor of three (see text). The intensity of the pre-edge feature reflects the covalent contribution of the thiolate ligand to the ground state molecular orbital.

To this end, Xα calculations on Cu-tet *b* have been performed, the parameters for which are given in Table 3.1. The highest occupied valence molecular orbitals for the Cu-tet *b* molecule are given in Table 3.3. The metal contribution to the ground state wavefunction (state 18a') is 0.88 $d_{x^2-y^2}$ and 0.11 d_{z^2}. These contributions help to picture the effective symmetry of this site. 5-coordinate sites can be described as structural distortions along a C_s distortion pathway between the two high symmetry limits of square pyramidal and trigonal bipyramidal, where the square pyramidal has a $d_{x^2-y^2}$ ground state and the trigonal bipyramidal has a d_{z^2} ground state. In the tetragonal coordinate system the trigonal bipyramidal ground state is written as 75% $d_{x^2-y^2}$ and 25% d_{z^2}.[51] Therefore, the 11% d_{z^2} component of the ground state in Cu-tet *b* indicates a structure half-way between the two high symmetry limits (Figure 3.11).

The Xα calculation provides important insight into the character of the half-occupied molecular orbital. In contrast to the bonding scheme in Pc in which the highest occupied molecular orbital (HOMO) contains a strong Cu $3d_{x^2-y^2}$ - Spπ antibonding interaction, the half-occupied orbital in Cu-tet *b* is rotated by 45° with respect to the Cu-S(thiolate) bond and is characterized by a σ-antibonding interaction (Figure 3.12). It is much less covalent than Pc, consisting of 66% Cu $3d_{x^2-y^2}/d_{z^2}$ and 15% Spσ, while the wavefunction in Pc is 42% Cu $3d_{x^2-y^2}$ and 36% Spπ.[4,5] This difference in bonding is attributed to the increased Cu-S bond length of Cu-tet *b* (2.36 Å) relative to Pc (2.13 Å), which reduces the π-interaction. The Cu-thiolate bonding in the Cu-tet *b* model complex is now understood and the results of the calculation can be used to give a quantitative description of the S K-edge data. Thus, the pre-edge intensity of the S K-edge spectrum reflects a ~15% Sp contribution to the half-occupied ground state orbital ($\alpha'^2 = 0.15$ for Cu-tet *b*). Using the protocol outlined in Chapter 1 and reference 26 and the quantitative intensities derived from the fits to the data, the Pc pre-edge intensity reflects 38% Sp character in the ground state orbital. This is in quantitative agreement with the Xα calculation on Pc which gives the Sp contribution to the ground state wavefunction to be 36%.[4,5] It is thus experimentally confirmed that the ground state of Pc is highly covalent, containing ~38% ± 3% Sp character. Further, this analysis provides a quantitative description of sulfur pre-edge intensities with respect to covalency.

Having achieved a good description of the bonding in Cu-tet *b*, it is useful to relate this calculation to previously published spectral data.[27] Slater transition state calculations were performed on selected states for comparison to the experimental absorption spectrum. The experimental charge transfer (CT) bands appear[27] at ~23,500 cm^{-1} and 27,800 cm^{-1} for the Sπ and Sσ to Cu CT transitions, respectively. The calculated transition energy for the Sσ CT transition (from state 15a') is 26,762 cm^{-1}, in good agreement with experiment.

Table 3.3. Results of SCF-Xα-SW Calculation for the Highest Occupied Valence Levels of Cu-tet *b*: Ground State Orbital Energies and Charge Distribution

Level	Energy (eV)	Character†
18a'	-2.467	66% Cu [0.88 d_{x2-y2} + 0.11 d_{z2}] (ab) 15% Sp_σ + ~20% N
10a"	-3.169	35% Cu [0.88 d_{xz}] (ab) 51% Sp_π + ~12% N
17a'	-3.806	68% Cu [d_{z2}] (ab) 21% Sp_σ + ~12% N
9a"	-4.205	53% Cu [d_{xz}] (b) 32% Sp_π + ~18% N
16a'	-4.431	94% Cu [d_{xy}] (nb) 3% Sp
8a"	-4.459	98% Cu [d_{yz}]
15a'	-5.074	55% Cu [0.47 d_{x2-y2} + 0.41 d_{z2} + 0.11 d_{xy}] (b) 37% Sp_σ

† (ab) denotes antibonding interaction; (b) denotes bonding interaction; (nb) denotes a non-bonding state

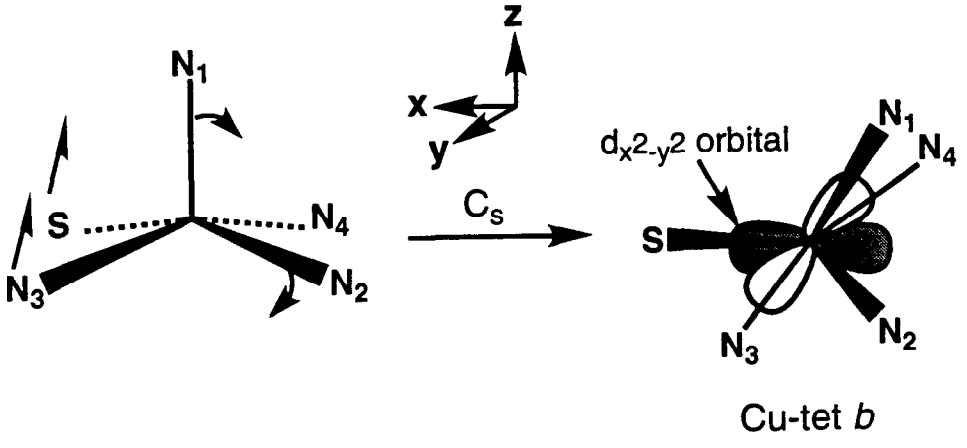

Figure 3.11. Schematic representation of the C_S structural distortion from the 5-coordinate square pyramidal limit to the Cu-tet *b* molecular structure.

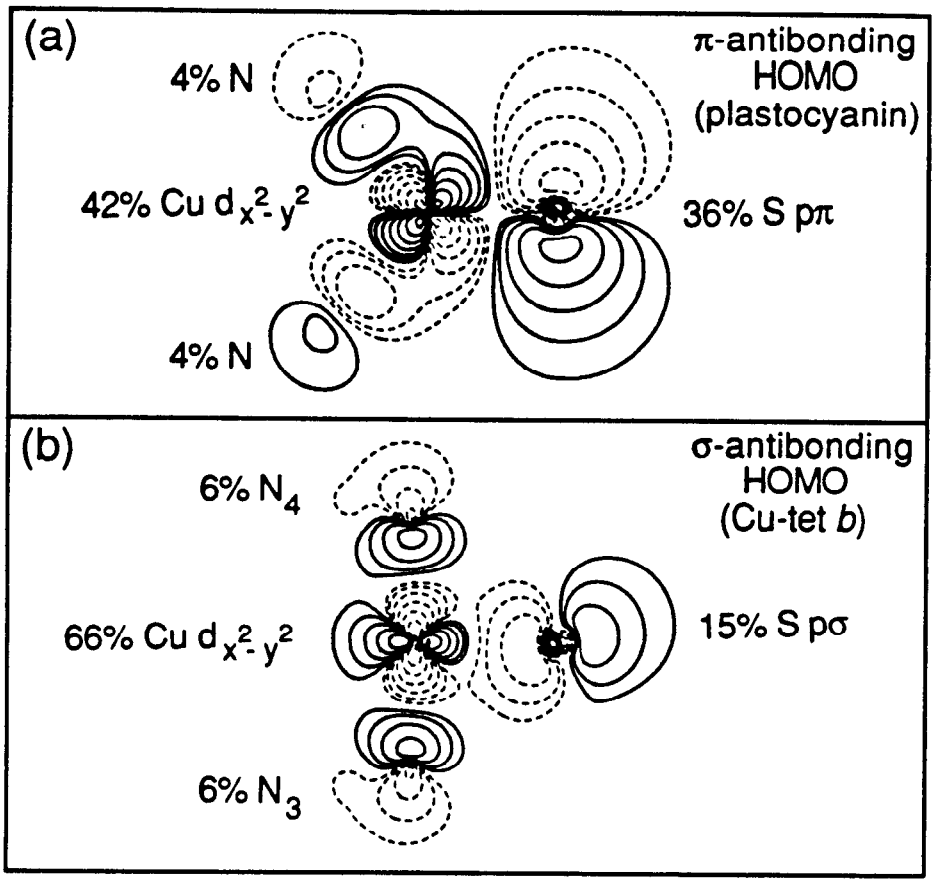

Figure 3.12. (a) Xα calculation contour plot of the highest occupied molecular orbital (HOMO) of plastocyanin showing the strong Cu-S(thiolate) π-interaction (taken from references 4-5). (b) Xα calculation contour plot of the HOMO of Cu-tet *b* (state 18a') showing the Cu-S(thiolate) σ-interaction. The N_3 and N_4 labels refer to the atom numbering shown in Figure 3.11. Note that, as described in Table 3.3, the 66% Cu d-orbital character of this orbital is comprised of 88% d_{x2-y2} and 11% d_{z2}.

The calculated transition energy for the Sπ CT transition (from state 9a") is 15,365 cm^{-1}. This calculation gives an anomolously low result because states 8a" and 9a" come close in energy, resulting in a great deal of mixing of the two states and change in character of the wavefunctions upon ionization within the transition state. However, the calculations do predict the proper ordering of the Sσ and Sπ CT transitions. The experimental ligand field transitions[27] appear at 10,900 cm^{-1}, 13,700 cm^{-1}, and 17,000 cm^{-1}, with the 13,700 cm^{-1} feature having an unusually high ε value for a d —> d transition. The ligand field transition energies from states 17a', 16a', and 8a" are calculated to be 11,130 cm^{-1} (d_{z2}), 17,446 cm^{-1} (d_{xy}), and 18,389 cm^{-1} (d_{yz}), respectively. Of the three ligand field transitions, only the 17a' state (d_{z2}) contains significant Sp ligand character due to configurational interaction with the 15a' Spσ level. Thus, the most intense ligand field band at 13,700 cm^{-1} is reasonably correlated with this transition.

The S K-edge data in Figure 3.10 also show that the pre-edge feature of Cu-tet *b* is higher in energy than in Pc. The pre-edge feature in the Cu-tet *b* spectrum appears at 2470.3 eV, while that for Pc is at 2469.0 eV. A comparison of the S K-edge pre-edge energies to the energies of the CT bands in the optical spectra (Sπ CT in Pc[4,5] and Sσ CT in Cu-tet *b*[27]) show that there is a shift in the CT band to higher energy (relative to Pc) in the Cu-tet *b* by 1.40 eV. Both the CT band and the S pre-edge feature reflect transitions to the $3d_{x2-y2}$ orbital. Clearly the distorted 5-coordinate geometry of Cu-tet *b* results in increased repulsion of the $3d_{x2-y2}$ orbital relative to that in Pc, causing both the CT transition and the S K-edge pre-edge transition to occur at higher energy in the Cu-tet *b* spectrum. This is in agreement with Xα calculations which indicate the HOMO orbital is higher in energy in Cu-tet *b* than in Pc by 0.7 eV.[4,5]

3.4. Discussion

From single crystal polarized Cu K-edge XAS studies, it has been demonstrated that the origin of the small hyperfine splitting in blue copper centers is not 12% $4p_z$ mixing in the ground state. Further, the S K-edge data, in combination with Xα calculations on the Cu-tet *b* model complex, show experimentally that the unpaired electron density at the blue copper site is highly delocalized and the site is characterized by an unusually covalent Cu-S(Cys) bond. These results are in quantitative agreement with the Xα calculation on the Pc site which indicate that the thiolate contribution to the ground state wavefunction is ~38%.[4,5] These experimental results indicate that delocalization of electron density onto the thiolate cysteine ligand is the origin of the small parallel hyperfine splitting in the EPR spectra of blue copper centers.

Xα calculations on the Cu-tet *b* molecule have provided insight into Cu-S(thiolate) bonding in this complex. The electronic structure of Cu-tet *b* is consistent with a geometry about halfway between the square pyramidal and trigonal bipyramidal limits. The dominant bonding interaction in Cu-tet *b* is a Cu-S σ-interaction (in contrast to the π-interaction in blue copper), which is probably due to the increased bond length relative to that in the blue copper centers.

The origin of the small $A_{||}$ hyperfine splitting in D_{2d} $CuCl_4^{2-}$ can now be addressed. The Cu K-edge studies and shakedown transition analysis of D_{2d} $CuCl_4^{2-}$ show that the magnitude of $4p_z$ mixing into the ground state is ~4%. Thus, as in blue copper, 12% $4p_z$ mixing can be ruled out as the origin of the small hyperfine splitting. In contrast to blue copper, Cl K-edges show that the complex is not unusually covalent. Therefore, the origin of the small hyperfine must be attributed to a large orbital dipolar contribution for which the sign is opposite that of the spin dipolar term associated with the half-occupied $3d_{x^2-y^2}$ orbital. This is consistent with our earlier studies of this complex.[13]

The contributions to the 1s —> 3d transition intensity in the Cu K-edge at ~8979 eV are now well understood. Because higher order terms in the multipole expansion cannot be neglected at Cu K-edge energies, there is a contribution to the transition intensity from a 1s —> 3d quadrupole-allowed transition. Additionally, in appropriate site symmetries, 4p mixing into the $3d_{x^2-y^2}$ orbital gives electric dipole allowed character to the transition. Polarized single crystal experiments are a useful probe into the nature and relative magnitude of this 4p mixing in a metal center. The transition in the Cu K-edge spectrum of Cu(II) complexes at ~8987 eV has been assigned as a 1s —> 4p +LMCT shakedown transition. We have presented the first quantitative analysis of the intensity of this feature in Cu K-edge spectra and have assigned the 1s —> 4p main transition in the *z*-polarized Cu K-edge spectrum of D_{2d} $CuCl_4^{2-}$ at 6.6 eV higher energy. From this analysis, the energy and intensity of the shakedown pre-edge feature are related to the degree of relaxation which occurs upon promotion of the 1s electron to a valence orbital. We have observed experimentally that this relaxation is somewhat less than that for complete 2p ionization.

Ligand K-edge data have been shown to be a powerful tool in the study of the electronic structures of metal-ligand interactions in open shell metal ions. Ligand pre-edge intensity is a direct probe of the covalency of a metal-ligand bond. In this chapter, we have quantified the sulfur pre-edge intensity in terms of the covalency of the Cu-S bond using Xα calculations and have thus presented the first use of ligand edges to quantitatively probe covalency in a metalloprotein.

3.5. Acknowledgments

This work was supported by grants from NSF (CHE91-21576, K.O.H), (CHE89-19687, E.I.S) and NIH (RR01209, K.O.H). SSRL operations are funded by the Department of Energy, Office of Basic Energy Sciences. The Biotechnology Program is supported by the NIH, Biomedical Research Technology Program, National Center for Research Resources. Further support is provided by the Department of Energy, Office of Health and Environmental Research. We also wish to thank Professor Hans Freeman of the University of Sydney who provided the poplar Pc crystals and participated in the single crystal experiments for which the data was previously published in reference 17. We also thank Drs. Robert A. Scott and Teresa A. Smith who contributed to some of the early phases of this work. Finally, acknowledgment goes to Dr. Mike Lowery and Mr. Lou LaCroix who waded through buckets of spinach glop to aid in the isolation of spinach plastocyanin, as well as to all members of the Solomon lab who pitched in to devein many boxes of fresh spinach.

3.6. References and Notes

(1) Solomon, E. I.; Penfield, K. W.; Wilcox, D. E. *Structure and Bonding* **1983**, *53*, 1-57.

(2) Gray, H. B.; Solomon, E. I. In *Copper Proteins*; Spiro, T. G., Ed.; Wiley: New York, 1980; pp 1-39.

(3) Adman, E. T. In *Advances in Protein Chemistry, Metalloproteins: Structural Aspects*; Anfinsen, C. B.; Edsall, J. T.; Richards, F. M.; Eisenberg, D. S., Ed.; Academic Press, Inc.: New York, 1991; Vol. 42; pp 145-192.

(4) Penfield, K. W.; Gewirth, A. A.; Solomon, E. I. *J. Am. Chem. Soc.* **1985**, *107*, 4519-4529.

(5) Gewirth, A. A.; Solomon, E. I. *J. Am. Chem. Soc.* **1988**, *110*, 3811-3819.

(6) Bates, C. A.; Moore, W. S.; Standley, K. J.; Stevens, K. W. H. *Proc. Phys. Soc.* **1962**, *79*, 73-93.

(7) Sharnoff, M. *J. Chem. Phys.* **1965**, *42*, 3383-3395.

(8) Solomon, E. I.; Hare, J. W.; Dooley, D. M.; Dawson, J. H.; Stephens, P. J.; Gray, H. B. *J. Am. Chem. Soc.* **1980**, *102*, 168-178.

(9) Guss, J. M.; Freeman, H. C. *J. Mol. Biol.* **1983**, *169*, 521-563.

(10) Adman, E. T.; Jensen, L. H. *Isr. J. Chem.* **1981**, *21*, 8-12.

(11) Roberts, J. E.; Brown, T. G.; Hoffman, B. M.; Peisach, J. *J. Am. Chem. Soc.* **1980**, *102*, 825-829.

(12) Penfield, K. W.; Gay, R. R.; Himmelwright, R. S.; Eickman, N. C.; Norris, V. A.; Freeman, H. C.; Solomon, E. I. *J. Am. Chem. Soc.* **1981**, *103*, 4382-4388.

(13) Gewirth, A. A.; Cohen, S. L.; Schugar, H. J.; Solomon, E. I. *Inorg. Chem.* **1987**, *26*, 1133-1146.

(14) Kau, L. S.; Spira-Solomon, D. J.; Penner-Hahn, J. E.; Hodgson, K. O.; Solomon, E. I. *J. Am. Chem. Soc.* **1987**, *109*, 6433-6442.

(15) Smith, T. A.; Penner-Hahn, J. E.; Berding, M. A.; Doniach, S.; Hodgson, K. O. *J. Am. Chem. Soc.* **1985**, *107*, 5945-5955.

(16) Hahn, J. E.; Scott, R. A.; Hodgson, K. O.; Doniach, S.; Desjardins, S. R.; Solomon, E. I. *Chem. Phys. Lett.* **1982**, *88*, 595-598.

(17) Scott, R. A.; Hahn, J. E.; Doniach, S.; Freeman, H. C.; Hodgson, K. O. *J. Am. Chem. Soc.* **1982**, *104*, 5364-5369.

(18) Hahn, J. E.; Hodgson, K. O. *ACS Symp. Ser.* **1983**, *211*, 431-444.

(19) Templeton, D. H.; Templeton, L. K. *Acta Crystallogr., Sect. A* **1980**, *36*, 237-241.

(20) Templeton, D. H.; Templeton, L. K. *Acta Crystallogr., Sect. A* **1982**, *38*, 62-67.

(21) Heald, S. M.; Stern, E. A. *Phys. Rev. B* **1978**, *17*, 4069-4081.

(22) Stern, E. A.; Sayers, D. E.; Lytle, F. W. *Phys. Rev. Lett.* **1976**, *37*, 298-301.

(23) Stern, E. A.; Sayers, D. E.; Dash, J. G.; Shechter, H.; Bunker, B. *Phys. Rev. Lett.* **1977**, *38*, 767-770.

(24) Cox, A. D.; Beaumont, J. H. *Philos. Mag. B* **1980**, *42*, 115-126.

(25) Kutzler, F. W.; Scott, R. A.; Berg, J. M.; Hodgson, K. O.; Doniach, S.; Cramer, S. P.; Chang, C. H. *J. Am. Chem. Soc.* **1981**, *103*, 6083-6088.

(26) Hedman, B.; Hodgson, K. O.; Solomon, E. I. *J. Am. Chem. Soc.* **1990**, *112*, 1643-1645.

(27) Hughey, J. L., IV; Fawcett, T. G.; Rudich, S. M.; Lalancette, R. A.; Potenza, J. A.; Schugar, H. J. *J. Am. Chem. Soc.* **1979**, *101*, 2616-2623.

(28) Schugar, H. J. unpublished results.

(29) Udupa, M. R.; Krebs, B. *Inorg. Chim. Acta* **1979**, *33*, 241-244.

(30) McGinnety, J. A. *J. Am. Chem. Soc.* **1972**, *94*, 8406-8413.

(31) Penner-Hahn, J. E. **1984**, Ph. D. Thesis, Stanford University.

(32) Smith, T. A. **1985**, Ph. D. Thesis, Stanford University.

(33) Note that the orientations shown in Figure 1 of reference 17 are those of crystal 2.

(34) Ellefson, W. L.; Ulrich, E. A.; Krogmann, D. W. In *Methods in Enzymology*; San Pietro, A., Ed.; McGraw-Hill: New York, 1980; Vol. 69; pp 223-228.

(35) Hedman, B.; Frank, P.; Gheller, S. F.; Roe, A. L.; Newton, W. E.; Hodgson, K. O. *J. Am. Chem. Soc.* **1988**, *110*, 3798-3804.

(36) In this molecule the $3d_{xy}$ ground state is equivalent to the $3d_{x2-y2}$ ground state of D_{4h} $CuCl_4^{2-}$ as a result of a 45° rotation of the *xy* molecular coordinate system and will be referred to herein as a $3d_{x2-y2}$ ground state.

(37) Agarwal, B. K. *X-ray Spectroscopy*; Springer-Verlag: Berlin, 1979, pp 276ff.

(38) Tyson, T. A.; Roe, A. L.; Frank, P.; Hodgson, K. O.; Hedman, B. *Phys. Rev. B* **1989**, *39A*, 6305-6315.

(39) Lytle, F. W. In *Applications of Synchrotron Radiation*; Winick, H.; Xian, D.; Ye, M. H.; Huang, T., Ed.; Gordon and Breach: New York, 1989; pp 135.

(40) Lytle, F. W.; Greegor, R. B.; Sandstrom, D. R.; Marques, E. C.; Wong, J.; Spiro, C. L.; Huffman, G. P.; Huggins, F. E. *Nucl. Instr. Meth.* **1984**, *226*, 542-548.

(41) Schwarz, K. *Phys. Rev. B* **1972**, *5*, 2466-2468.

(42) The effect of incomplete polarization of the beam cannot be quantitated for this data as it was not measured at the time of the experiment.

(43) Kosugi, N.; Yokoyama, T.; Asakura, K.; Kuroda, H. *Chem. Phys.* **1984**, *91*, 249-256.

(44) Bair, R. A.; Goddard III, W. A. *Phys. Rev. B* **1980**, *22*, 2767-2776.

(45) Manne, R.; Åberg, T. *Chem. Phys. Lett.* **1970**, *7*, 282-284.

(46) Larsson, S. *Phys. Scr.* **1977**, *16*, 378-380.

(47) van der Laan, G.; Westra, C.; Haas, C.; Sawatzky, G. *Phys. Rev. B: Condens. Matter* **1981**, *23*, 4369-4380.

(48) If the coordinate system of the plastocyanin molecule is rotated about *z* by 45° to define axes *x'* and *y'* (for the purpose of analysis), the ground-state orbital is $d_{x'y'}$ and the Cu-S(Cys) bond is along the *x'* axis. In C_s symmetry it is found[4-5] that only the $p_{y'}$ orbital mixes with the ground-state orbital. In the orientation which gives rise to Figure 3.8b, each $p_{y'}$ orbital is oriented 45° from **E**.

(49) Solomon, E. I. *Comments Inorg. Chem.* **1984**, *3*, 297-299.

(50) Note that the value derived here for covalency of the HOMO orbital corresponds to the total chloride contribution. This is in contrast to values in Chapter 2 which are given as covalent contributions per chloride.

(51) Wilcox, D. E.; Porras, A. G.; Hwang, Y. T.; Lerch, K.; Winkler, M. E.; Solomon, E. I. *J. Am. Chem. Soc.* **1985**, *107*, 4015-4027.